An adaptive optics system for astronomical image sharpening

Doel, A.P.

An Adaptive Optics System For Astronomical Image Sharpening

by
A.P. Doel, B.Sc.

A Thesis
Submitted to the University of Durham
for the Degree of
Doctor of Philosophy.

29 September 1990

Abstract

Images of stars in the focal plane of large astronomical telescopes are many times larger than the images expected from diffraction theory. Much of this blurring of the image is due to variations in the optical properties of the atmosphere above the observatory which for small aperture telescopes causes motion of the image, and for large aperture telescopes causes the image to break up into a number of smaller sub-images. This thesis describes a prototype adaptive system which is designed to sharpen astronomical images in real-time. The sharpening is achieved by removing the atmospherically induced motions of the image with servo-looped plane mirrors driven by piezo-electric actuators. The results of real-time sharpening obtained with the adaptive system at the William Herschel Telescope (WHT) are presented along with the results of an investigation into the characteristics of the atmospheric limitations at the La Palma observatory site.

[Telescopes] cannot be so formed as to take away that confusion of Rays which arises from the Tremors of the Atmosphere.

–Isaac Newton, *Opticks* (1704)

Note on Units

Unless otherwise stated, all quanities used in equations are given in S.I. units.

The value of the coherence parameter r_o given, unless the wavelength is specified, corresponds to a wavelength of 500 nm

Contents

Chapter 1

Introduction

The achievable resolution of a large ground based astronomical telescope is not governed by the diffraction limit of its aperture, but by the effects of atmospheric turbulence. For example, a 4 m telescope that has a theoretical diffraction limit of 25 milliarcseconds at visible wavelengths is, due to atmospheric limitations, only able to produce images of typically 1 arcsecond in size. This degradation of image quality, termed 'seeing', is due to the turbulent mixing in the atmosphere of regions of differing temperature which cause local refractive index variations; these in turn cause phase and amplitude distortions across the wavefront from an astronomical object at the aperture plane of a telescope. The main effect of these distortions for a small aperture telescope is to cause motion of the image; but for large apertures the image will break up into a number of smaller sub-images, called 'speckles'. These speckles are in continual motion giving rise to the characteristic 'boiling' appearance of stellar images when they are observed at high magnification.

The importance attached to eliminating these atmospheric effects can be seen in the search for observatory sites where good seeing conditions prevail. Although the Hubble Space Telescope should be able to achieve diffraction limited images unaffected by the atmospheric turbulence, its limited availability and the expense of operation provide a good incentive to develop cheap, ground based methods of high resolution imaging. Work in this field has been given further impetus with the planned construction of optically linked large telescope arrays such as the European Southern Observatory's Very Large Telescope Array, and the Columbus project, since these systems can only fulfil their true potential if atmospheric effects

are removed.

The astronomical applications of high resolution imaging are wide ranging. Such techniques have already been applied successfully to determining the radii and structure of nearby giant stars; to resolving close binary systems, and to the investigation of small scale features of the Sun such as magnetic fields and solar granulation cells. High resolution imaging would also benefit the study of the populations, distribution and properties of stars in nearby galaxies, and in the cores of globular clusters. There are also applications in the studies of galactic evolution where high resolution will enable more detailed investigation of the morphology of distant galaxies.

One of the high resolution imaging techniques in which there has been considerable progress in recent years is that of adaptive optics, where the seeing induced phase variations across a telescope aperture are removed in real-time by the action of rapidly guided plane or deformable mirrors. This method of image sharpening has an advantage over the many other proposed techniques in that no post-exposure processing is required and the corrected light output can be imaged directly onto an instrument of the observers choice, such as a Charged Coupled Device (CCD) camera or the slit of a spectrograph.

The MARTINI project (Multible Aperture Real Time Image Normalisation Instrument), developed at Durham University, is a prototype adaptive optics system designed to operate on the GHRIL (Ground Based High Resolution Imaging Laboratory) platform at the Nasmyth focus of the William Herschel Telescope (WHT). The system uses piezo-electrically driven plane mirror elements to remove the atmospherically induced tilt of a wavefront across an aperture. Atmospheric seeing theory predicts that with this technique, an optimum telescope aperture size exists at which the improvement in image resolution that can be achieved is maximised. The size of the optimum aperture is determined by the particular atmospheric conditions prevalent at the time of an observation, but typically it is between 40–80 cm. Therefore to enable the full light collecting abilities of a large telescope to be utilised, the full aperture must be divided into a number of sub-apertures. In MARTINI there are six such sub-apertures, the size of which can be altered to match the seeing conditions; each sub-aperture having its own

wavefront tilt correction system.

Construction of the MARTINI system began in October 1986, funded by a grant from the Science And Engineering Research Council (SERC), and the first tests with the instrument at the WHT were carried out in September 1988 and June 1989.

A project as large as MARTINI is clearly the work of a team of people. My particular involvement has been in following areas.

Imaging Photon Detector (IPD): in the determination of the operating characteristics of the IPD such as electronic dead-time, resolution, efficiency and uniformity of photocathode response.

Software: in developing control and display software for the IPD and the CCD camera, which is the present read-out system for the real-time corrected output of the MARTINI device. This software allows instant analysis of the images recorded by these systems, enabling parameters such as the images' full width half maxima to be quickly determined. I have also written the software to control the artificial star system and to enable it to simulate real star motion.

Piezo-actuators: in measuring the hysteresis of the actuators, and in developing algorithms that reduce the effect of this property on the positioning of the tip-tilt mirrors.

Data analysis: in the post-exposure processing of time-tagged photon event data recorded with the IPD during the observing runs. This has involved writing the analysis software to determine such parameters as the degree of post-exposure image sharpening that can be obtained, the size of the outer scale of turbulence, and the power spectrum of image motion.

Observing runs: I have been present at all the observations with the MARTINI system at the WHT, where I have been responsible for the setting up of the IPD and CCD systems and for their control during run-time.

The structure of the thesis is as follows. Chapter two gives a general introduction to the theory of atmospheric turbulence and the effect it has on astronomical imaging. Parameters relevant to image sharpening are described, such as the coherence parameter, the isoplanatic patch size, the outer scale of turbulence and the power spectrum of image motion. Chapter three gives a brief review of the various techniques of high resolution imaging with a more complete description of

the method of adaptive optics image sharpening. A summary is given of adaptive optics projects which have been implemented or are under development, along with a brief description of the device and their preliminary results. Chapter four is a description of the MARTINI image sharpening system. The optical and mechanical design is described along with its control system. In chapter five the results are presented of the September 1988, June 1989, and February 1990 observing runs with MARTINI at the WHT. The results of the real-time image sharpening with the MARTINI system are shown, along with those of the post-exposure analysis of time-tagged photon data. Chapter six reviews the planned improvements of the present system and discusses the longer term objectives for high resolution imaging development at Durham.

Chapter 2

Seeing Theory

2.1 Atmospheric Structure Function

In atmospheric flows large scale turbulent motions, almost inevitably produced by the processes that input the energy into the flow, give rise to turbulent motions on shorter scales, which themselves give rise to yet shorter scale turbulence. This 'breakup' process continues until scales are reached below which, due to the loss of energy by viscous dissipation, turbulent motion can not be sustained. Atmospheric turbulence can, therefore, be characterised by two scale lengths; one an upper scale L_0, termed the outer scale of turbulence, associated with the flow energy input processes; the other a lower scale l_0, termed the inner scale of turbulence, imposed by viscous dissipation effects (these scales are often referred to by their corresponding wave vectors which are given as $k_m = 2\pi/l_o$ and $K_o = 2\pi/L_0$). The sizes of the inner scale and outer scales vary with atmospheric height, but the average size of the inner scale is a few millimetres whilst atmosphere studies such as that of COULMAN [1] have shown that mean value of the outer scale of turbulence is typically less than 10 metres in size (see figure 2.1).

KOLMOGOROV [2] has shown from dimensional considerations that, within the inertial subrange $K_o < k < k_m$, the power spectrum of atmospheric velocity fluctuations in turbulence is given by the expression

$$P(\mathbf{k}) \propto k^{-\frac{11}{3}}. \tag{2.1}$$

where k is the modulus of the wave vector $\mathbf{k}$. The behaviour of the power spectrum of velocity fluctuations outside the inertial subrange range is less well established

but it is thought that at wavevectors beyond k_m there is an approximately exponential fall-off of power whilst below K_o the spectrum is assumed to become constant. The behaviour of the power spectrum over the whole range of wavevectors is often then modeled as

$$P(\mathbf{k}) \propto \frac{1}{(\frac{1}{L_o^2} + k^2)^{\frac{11}{6}}} \exp(-k/l_o). \tag{2.2}$$

and a plot of this spectrum is shown in figure 2.2.

Assuming, however, that the outer and inner scales of turbulence can be ignored and that the power spectrum of velocity fluctuations is described by equation 2.1 at all wave vectors (an assumption which can be crude as will be discussed later), it can be shown that the mean square difference of flow velocity between two points in space, $\mathbf{r}_1$ and $\mathbf{r}_2$, is proportional to the two-thirds power of the distance between the points. This allows the velocity structure function $D_V(\boldsymbol{\rho})$ to be written as

$$D_V(\boldsymbol{\rho}) = \langle |\mathbf{v_1} - \mathbf{v_2}|^2 \rangle = C_V^2 \rho^{\frac{2}{3}}, \tag{2.3}$$

where $\boldsymbol{\rho} = \mathbf{r}_1 - \mathbf{r}_2$ and C_V^2 is a constant of proportionality known as the velocity structure constant.

However, velocity fluctuations alone do not effect optical propagation, but temperature fluctuations will cause an effect and these can be linked to the turbulence by considering temperature as a 'conserved passive additive' (i.e. an additive which does not effect the dynamics of the turbulence or disappear by chemical reaction). TARTARSKI [4] and others (OBUKHOV [5], YAGLOM [6]) have shown that by considering temperature in such a way, the differences of temperature between two points in space follow the Kolmogorov power spectrum and therefore the structure function of temperature fluctuations $D_T(\boldsymbol{\rho})$ is given by

$$D_T(\boldsymbol{\rho}) = \langle |T_1 - T_2|^2 \rangle = C_T^2 \rho^{\frac{2}{3}}, \tag{2.4}$$

where C_T is the temperature structure constant.

Refractive index fluctuations depend linearly on temperature fluctuations, so the refractive index structure function $D_N(\boldsymbol{\rho})$ can be written as

$$D_N(\boldsymbol{\rho}) = \langle |n_1 - n_2|^2 \rangle = C_N^2 \rho^{\frac{2}{3}}, \tag{2.5}$$

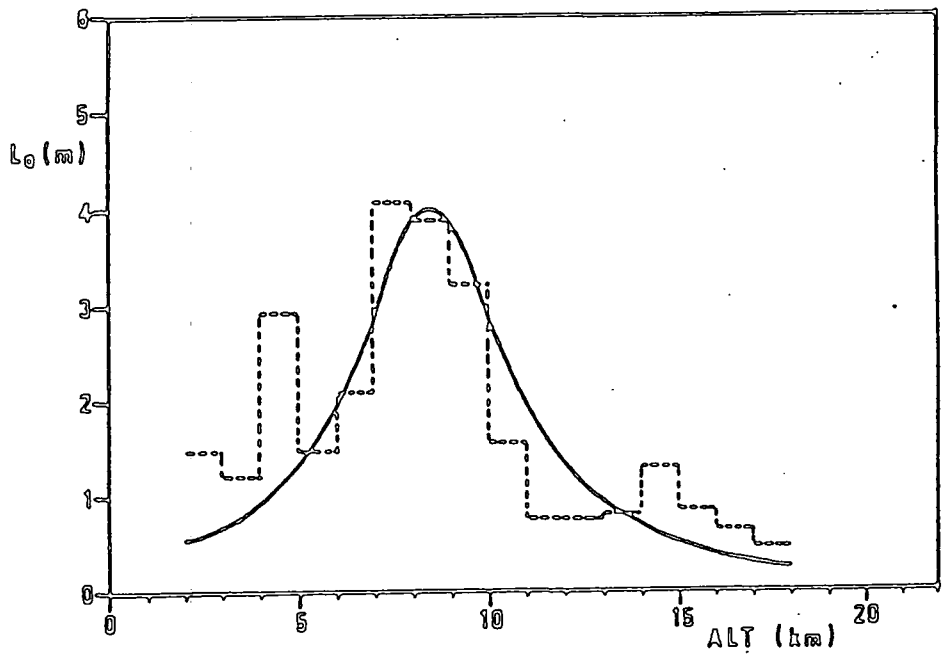

Figure 2.1: Size of the outer scale of turbulence as a function of altitude (from Coulman et al. [1]).

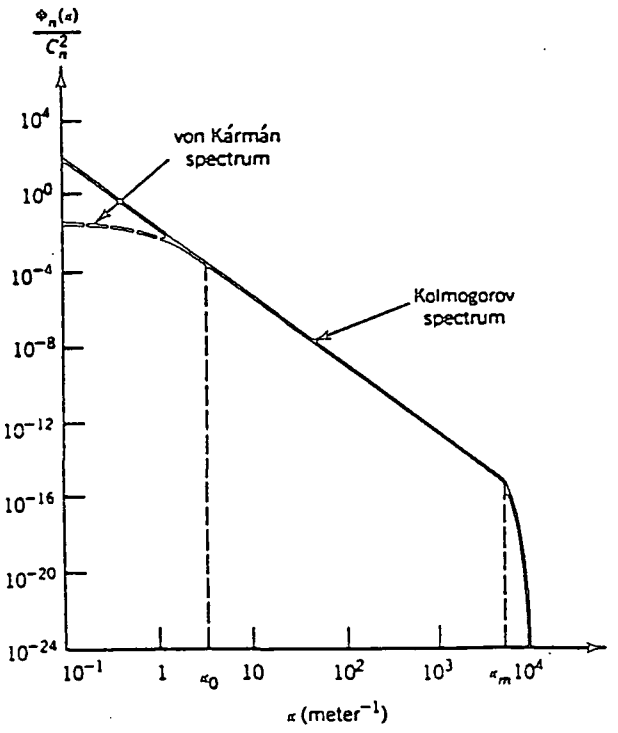

Figure 2.2: Power spectrum of refractive index fluctuations (from Goodman [3]).

with C_N, the refractive index structure constant, being related to the temperature structure constant by

$$C_N = 80 \times 10^{-6} C_T \frac{P}{T^2}, \tag{2.6}$$

where P is the air pressure expressed in millibar and T the air temperature in degrees Kelvin. Under normal conditions of temperature and pressure C_N is approximately $10^{-6} C_T$.

Various investigations have been made to determine the distribution of C_N^2, and hence the turbulence distribution through the atmosphere. It has been found that below 4 km the value of C_N^2 is greatly affected by considerations of the local geography. However, above 4 km the variation with height of the average value of C_N^2 seems to be independent of the location at which the measurements are made. Figure 2.3 shows a typical profile of the C_N^2 distribution with height as measured by BARLETTI ET AL. [7]. The values plotted are averages of C_N^2 distribution profiles determined on a number of different days and at different locations. The value of C_N^2 can be seen, at first, to fall quite sharply with increasing altitude reaching a minimum of about $10^{-17}\,\mathrm{m}^{-\frac{2}{3}}$ at 6 km, then increasing to a secondary maximum at about 10km before continuing to decrease at higher altitudes. Also shown in the figure is the semi-empirical model of C_N^2 distribution as derived by HUFNAGEL [8], where the value of the refractive index constant at height h is given by

$$C_N^2(h) = \mathrm{A}\left[2.2 \times 10^{-26} h^{10} \exp\left(\frac{-h}{1000.0}\right)\left(\frac{V}{V_m}\right)^2 + 10^{-16} \exp\left(-\frac{h}{1500}\right)\right] \tag{2.7}$$

where A is an arbitrary scaling constant and V/V_m is the ratio of the upper atmospheric wind speed to a mean upper atmospheric wind speed.

Though the averaged C_N^2 distribution can be expected to follow that shown in figure 2.3, the distribution of C_N^2 as measured on one particular night is not a smooth distribution, but it is found that the turbulence seems to occur in thin layers of thicknesses of between 100–200 m, where the C_N^2 value is a factor of 10 or so above its background level (see figure 2.4).

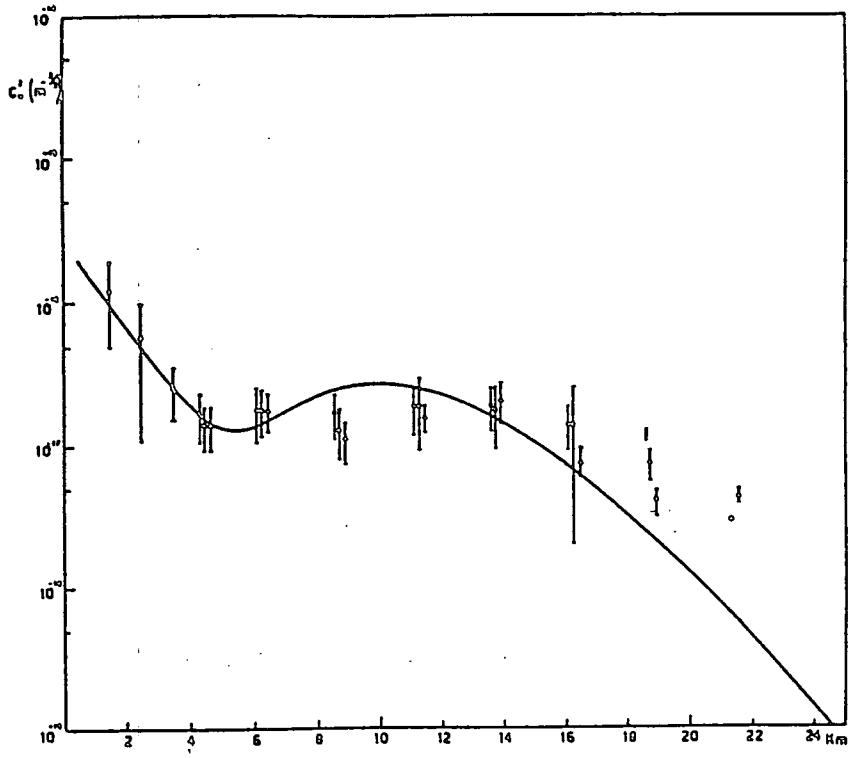

Figure 2.3: Average distribution of the refractive index structure constant with height (from Barletti et al.[7]). Also shown (solid line) is the semi-empirical model of refractive index structure constant variation as derived by Hufnagel [8].

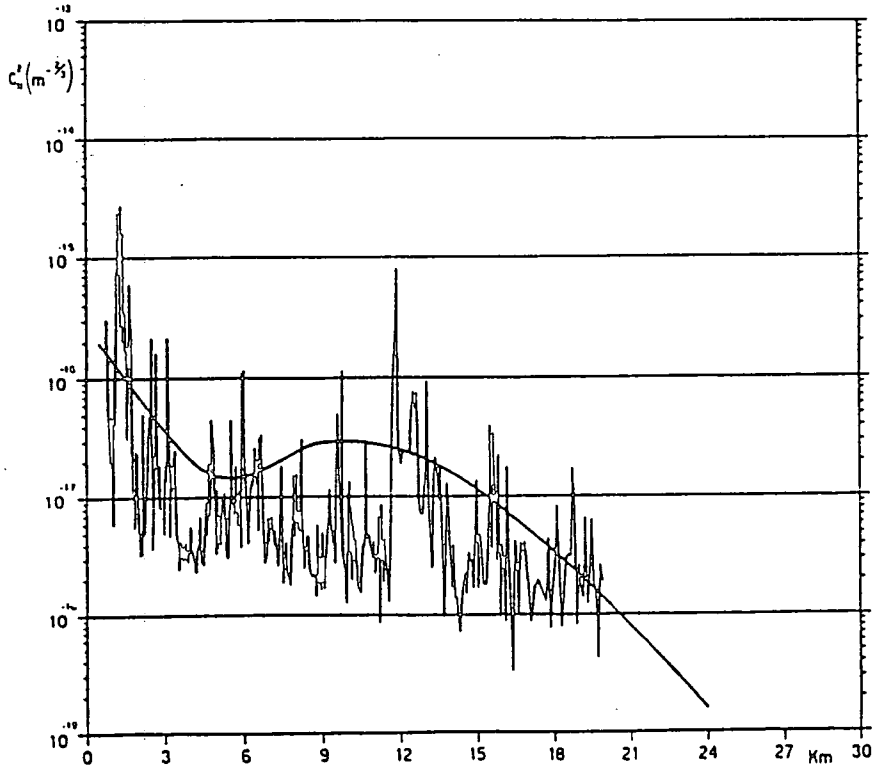

Figure 2.4: Typical distribution of the refractive index structure constant as measured on a single night (from Barletti et al. [7]).

2.2 Atmospheric Transfer Function

The effect of turbulence induced refractive index variations on a plane wave passing through the atmosphere is to introduce changes of phase and amplitude along the wavefront. If such a perturbed wave is incident on a telescope aperture, the aperture function, $f(\mathrm{r})$, can be written as

$$f(\mathrm{r}) = f_o(\mathrm{r}) \exp\left[i\Phi(\mathrm{r}) + L(\mathrm{r})\right], \tag{2.8}$$

where $f_o(\mathrm{r})$ is the aperture function for an unperturbed plane wave, and $\Phi(\mathrm{r})$, $L(\mathrm{r})$ are functions describing, respectively, the phase and log-amplitude variations of the wave due to turbulence. The log-amplitude term is usually regarded as being small compared to the phase term and thus it may be ignored. This is the so called 'Near field approximation' and the results of computer simulations and stellar scintillation studies (see RODDIER [9], RODDIER AND RODDIER [10]), all seem to suggest that in the case of astronomical observations such an assumption is justified.

The optical transfer function $\mathrm{OTF}(\boldsymbol{\rho})$ of the overall atmosphere and telescope system can now be found from the convolution of the aperture function,

$$\mathrm{OTF}(\boldsymbol{\rho}) = f(\mathrm{r}) \odot f(\mathrm{r} - \lambda\boldsymbol{\rho}), \tag{2.9}$$

which can be rewritten, neglecting the log-amplitude term of the aperture function, as

$$\mathrm{OTF}(\boldsymbol{\rho}) = \int_{-\infty}^{\infty} f_o(\mathrm{r}) f_o(\mathrm{r} - \lambda\boldsymbol{\rho}) \exp\left[i\Phi(\mathrm{r}) - i\Phi(\mathrm{r} - \lambda\boldsymbol{\rho})\right] \mathrm{dr}. \tag{2.10}$$

It is to be noted that for a point source such as a star this optical transfer function is equivalent to the modulation transfer function $\mathrm{MTF}(\boldsymbol{\rho})$.

2.2.1 Long Exposure Transfer Function

If the average OTF over a sufficiently long period of time is considered, the exponential part of equation 2.10 can be represented as an ensemble average. Thus equation 2.10 can be rewritten as

$$\mathrm{OTF}(\boldsymbol{\rho}) = \int_{-\infty}^{\infty} f_o(\mathrm{r}) f_o(\mathrm{r} - \lambda\boldsymbol{\rho}) \left\langle \exp\left[i\delta\Phi\right] \right\rangle \mathrm{dr}, \tag{2.11}$$

where $\delta\Phi$ is the difference between phase variations at $\mathbf{r}$ and $\mathbf{r} - \lambda\boldsymbol{\rho}$, and $\langle \ldots \rangle$ denotes an ensemble average. Assuming both $\Phi(\mathbf{r})$ and $\Phi(\mathbf{r} - \lambda\boldsymbol{\rho})$ have gaussian distributions, then the distribution of $\delta\Phi$ is also described by a gaussian and in such a case it can be shown that

$$\langle \exp[i\delta\Phi] \rangle = \exp\left[-\frac{1}{2}\left\langle \delta\Phi^2 \right\rangle\right],$$

and

$$\left\langle \delta\Phi^2 \right\rangle = \left\langle [\Phi(\mathbf{r}) - \Phi(\mathbf{r} - \lambda\boldsymbol{\rho})]^2 \right\rangle = D_\Phi(\boldsymbol{\rho}),$$

where $D_\Phi(\boldsymbol{\rho})$ is the structure function of phase variations. The optical transfer function can now be written as

$$\mathrm{OTF}(\boldsymbol{\rho}) = \int_{-\infty}^{\infty} f_o(\mathbf{r}) f_o(\mathbf{r} - \lambda\boldsymbol{\rho}) \exp[-\frac{1}{2} D_\Phi(\boldsymbol{\rho})] d\mathbf{r}. \tag{2.12}$$

The first part of this equation is simply the optical transfer function of the telescope for an incident unperturbed plane wave, whilst the exponential part depends solely on the properties of the atmosphere and is termed the long exposure atmospheric transfer function, $\mathrm{OTF}_{\mathrm{LE}}(\boldsymbol{\rho})$. Thus

$$\mathrm{OTF}_{\mathrm{LE}}(\boldsymbol{\rho}) = \exp[-\frac{1}{2} D_\Phi(\boldsymbol{\rho})]. \tag{2.13}$$

In the case of an infinite plane wave source such as a star, observed at a zenith angle of θ, the phase structure function has been shown by FRIED [11] to be related to the refractive index structure constant by the following expression

$$D_\Phi(\boldsymbol{\rho}) = 2.91 \left(\frac{\lambda}{2\pi}\right)^2 (\lambda\rho)^{\frac{5}{3}} \sec\theta \int_0^H C_N^2(h) dh, \tag{2.14}$$

where h is height in the atmosphere and H is the total height over which the atmosphere is chosen to extend. It is convenient now to use the coherence diameter r_o, first introduced by FRIED [12]. This is defined as

$$r_o = \left[0.423 \left(\frac{\lambda}{2\pi}\right)^2 \sec\theta \int_0^H C_N^2(h) dh\right]^{-\frac{3}{5}}, \tag{2.15}$$

From equations 2.14 and 2.15, the long exposure atmospheric transfer function can be written as

$$\mathrm{OTF}_{\mathrm{LE}}(\boldsymbol{\rho}) = \exp\left[-3.44 \left(\frac{\lambda\rho}{r_o}\right)^{\frac{5}{3}}\right]. \tag{2.16}$$

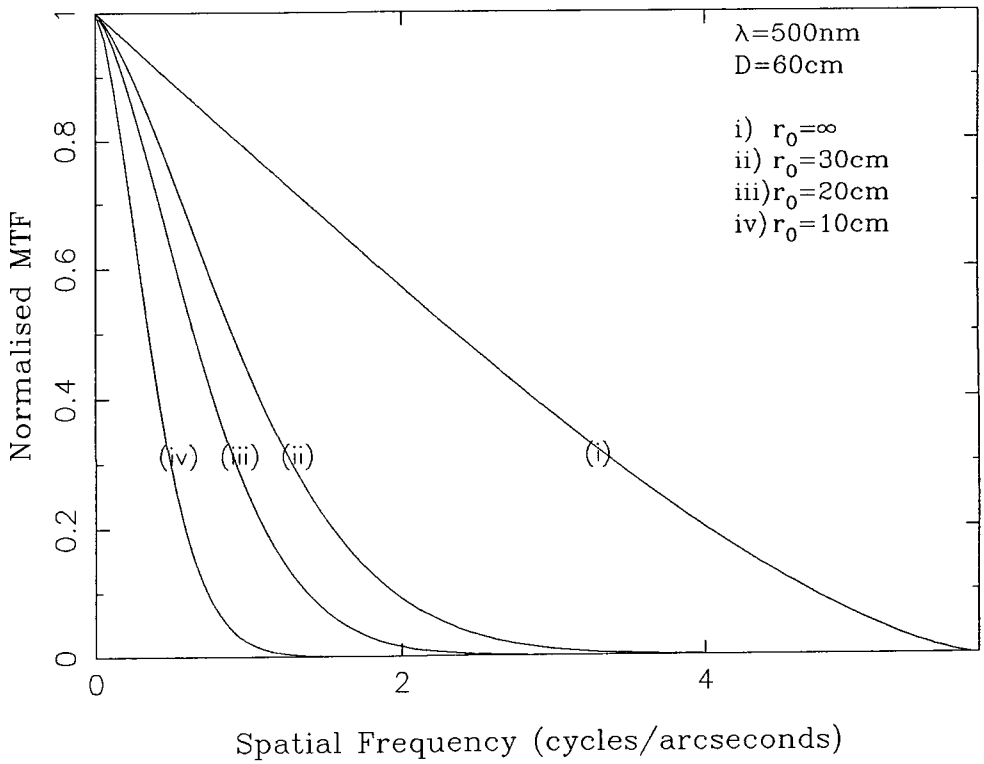

Figure 2.5: Long exposure optical transfer functions for combined atmosphere and telescope system.

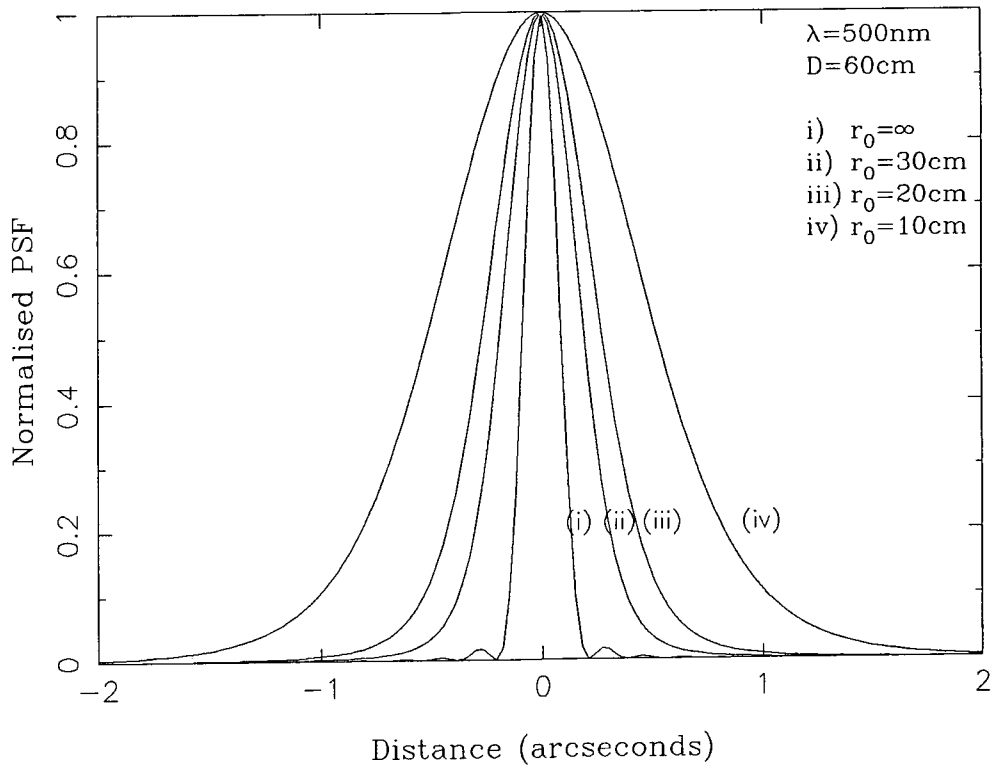

Figure 2.6: Long exposure point spread functions for combined atmosphere and telescope system.

Using this result the overall OTF of a telescope and atmosphere system can be calculated. The associated point spread function PSF(r) can be obtained by a Hankel Transformation of the optical transfer function,

$$\mathrm{PSF(r)} = 2\pi \int_0^\infty \mathrm{OTF}(\rho)\mathrm{J_o}(2\pi\rho r)d\rho, \tag{2.17}$$

where $\mathrm{J_o}(x)$ is the zero order Bessel function. Figures 2.5 and 2.6 show the theoretically predicted long exposure OTFs and PSFs of a telescope 0.6 m in diameter, for several values of coherence parameter r_o. It can be seen that effect of atmospheric turbulence is to reduce considerably the amount of information available especially at high spatial frequencies.

The actual atmospheric transfer function has been investigated experimentally by several groups using a variety of different techniques. KING [13] measured the photographic image profiles of stars and compared them to the theoretically predicted profiles. Others (BROWN AND SCADDEN [14]) have used interferometric methods to measure the atmospheric OTF directly. The results of these investigations seem to confirm that equation 2.16 provides a good fit to the experimental data.

2.2.2 Short Exposure Transfer Function

If instead of a long exposure, a short time duration exposure of a star is considered (i. e. a few milliseconds) then the effect is to 'freeze' the seeing motion of the star image. If a whole sequence of these short exposure images are then recentered and superimposed, an image can be constructed where the random tilt component of the wavefront distortion across the telescope aperture has been effectively removed.

The optical transfer function for such a short exposure image has been derived by FRIED [15]. Fried, however, makes a distinction between the short exposure atmospheric OTF obtained when the seeing is termed 'near' and that which is obtained when the seeing is termed 'far'. Near seeing is defined as when the size of the telescope aperture being used for the observations is very much greater than the quantity $(L\lambda)^{\frac{1}{2}}$, where L is the length of the propagation path through the turbulent medium. Far seeing conditions are defined as when the telescope diameter D is very much smaller than $(L\lambda)^{\frac{1}{2}}$. Fried the gives the short exposure

atmospheric transfer function $\mathrm{OTF_{SEN}}$ and $\mathrm{OTF_{SEF}}$ for such near and far seeing conditions as

$$\mathrm{OTF_{SEN}}(\rho) = \exp\left[-3.44\left(\frac{\lambda\rho}{r_o}\right)^{\frac{5}{3}}\left(1-\left(\frac{\lambda\rho}{D}\right)^{\frac{1}{3}}\right)\right], \tag{2.18}$$

and

$$\mathrm{OTF_{SEF}}(\rho) = \exp\left[-3.44\left(\frac{\lambda\rho}{r_o}\right)^{\frac{5}{3}}\left(1-\frac{1}{2}\left(\frac{\lambda\rho}{D}\right)^{\frac{1}{3}}\right)\right], \tag{2.19}$$

where D is the diameter of the telescope aperture.

In fact for most astronomical observations the seeing can be regarded as near, since it has been shown from experimental determinations of the distribution of the refractive index structure constant C_N^2, that the greatest contribution to seeing is made by thin layers at a heights of less than 15 km. The term $(L\lambda)^{\frac{1}{2}}$ can therefore be expected to be small compared to the aperture diameter of a reasonably large telescope.

Figures 2.7 and 2.8 show the OTFs and PSFs determined for short exposure (near seeing) imaging for a telescope-atmosphere system. Compared to the OTFs obtained for long exposures images, more high spatial frequency information is retained and thus the short exposure images formed will be correspondingly sharper.

2.3 Resolution

In seeing theory it is usual to define resolution in accordance with the Strehl criterion, where the resolution R is given as the sum over all frequencies of the optical transfer function. Thus

$$R = \int_0^\infty \mathrm{OTF}(\rho)d\rho. \tag{2.20}$$

Using equations 2.16, 2.18 and 2.20, the theoretical resolution of a telescope and atmosphere system, for both long and short exposure cases, can now be determined for any particular values of telescope aperture D and coherence parameter r_o. In particular it can be shown that if the telescope has an aperture D very much greater than r_o, the resolution for both long and short exposures approaches an asymptotic limit, R_∞, given by the expression

$$R_\infty = \frac{1}{4}\pi\left(\frac{r_o}{\lambda}\right)^2. \tag{2.21}$$

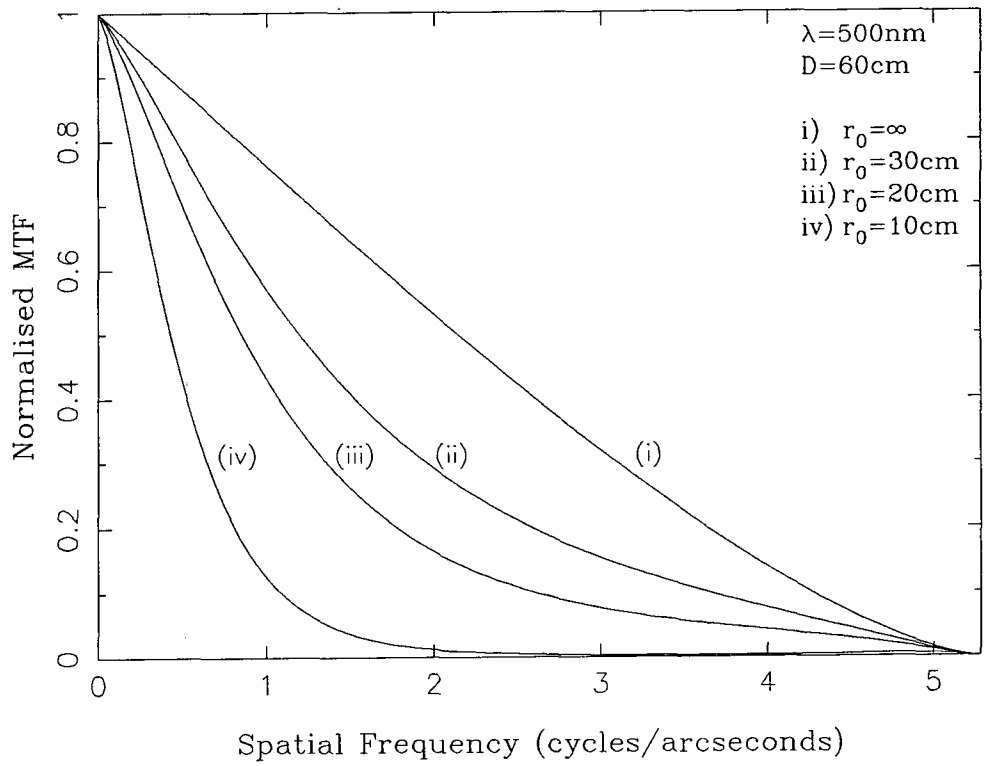

Figure 2.7: Short exposure optical transfer functions for combined atmosphere and telescope system.

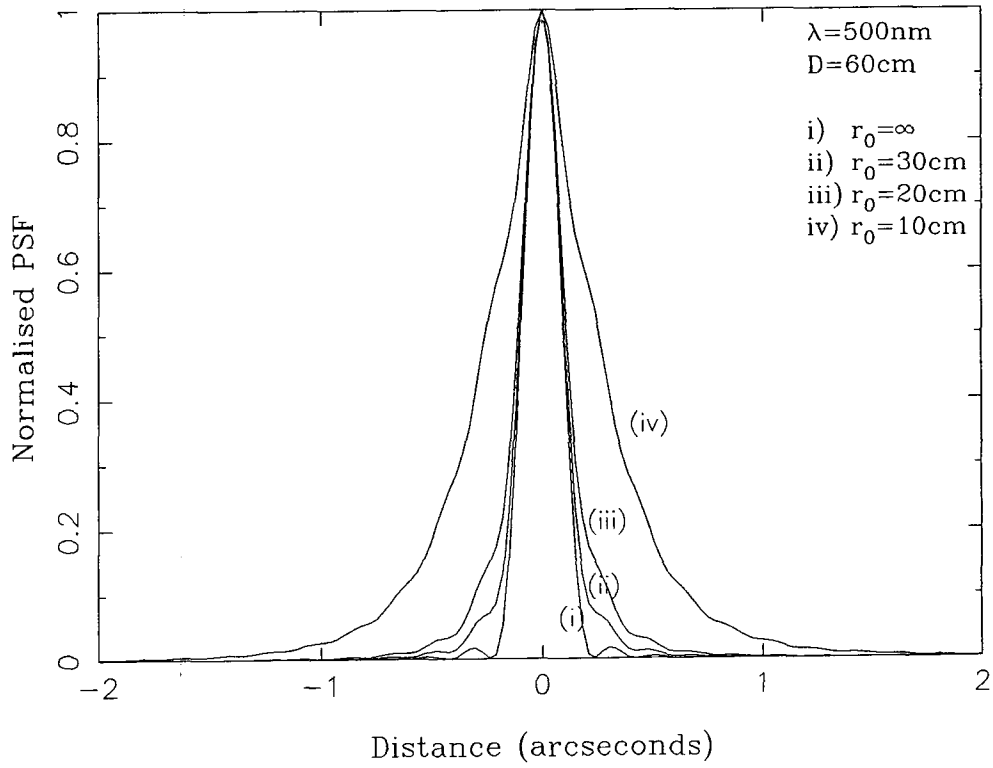

Figure 2.8: Short exposure point spread functions for combined atmosphere and telescope system.

It is convenient, therefore, to use a normalised resolution R/R_∞, and figure 2.9 shows such a normalised resolution as a function of D/r_o, for long and short exposures. Also shown in the figure is the theoretical resolution achievable if the telescope were diffraction limited. It can be seen from these figures that with long exposures the resolution follows the diffraction limited curve at low values of D/r_o, but at higher values the curve turns off and approaches the asymptotic limit. In the short exposure case, the resolution again follows the diffraction limited curve at low D/r_o values, but instead of just gradually turning off from this curve, the resolution is seen to peak at a D/r_o value of approximately 3.8 before declining again and approaching the asymptotic limit. At this point of short exposure maximum resolution, the factor of improvement that is gained over R_∞ is 3.5.

To relate the resolution to the image size, RODDIER [9] defines a quantity called the 'blurring spread angle' ω as the diameter of a disk, with uniform illumination equal to the central intensity of the image considered, and with the same total intensity as the image. This can be related to the resolution by

$$\omega = \left(\frac{4}{\pi R}\right)^{\frac{1}{2}}. \tag{2.22}$$

A plot of ω against D/r_o for both long and short exposures is shown in figure 2.10. A minimum in the short exposure spread angle is reached at $D/r_o = 3.8$ and the improvement over the spread angle as $D/r_o \to \infty$ is about a factor of 2.0.

However, use of blurring angle as an indication of image sharpness is slightly misleading in that it is related to the integral of the OTF over all frequencies and therefore loses information on the detailed structure of the image. An alternative and perhaps more useful measure of the image size is the full width half maximum (FWHM) value as determined from the Hankel Transform of the optical transfer function. Figures 2.11 and 2.12 show the FWHM of long and short exposure images as a function of telescope diameter, for r_o values of 10 cm and 20 cm. A minimum in FWHM is again reached in the short exposure curve at about $D/r_o \approx 3.8$, with an improvement over the FWHM as $D/r_o \to \infty$ of about a factor of 3.

Another measure of image sharpness which is often quoted is the Strehl Ratio SR, which is defined as the ratio of the central intensity of the image to that of the central intensity of the diffraction limited image. This ratio can be expressed in terms of the atmospheric and diffraction limited OTFs of the image; for example

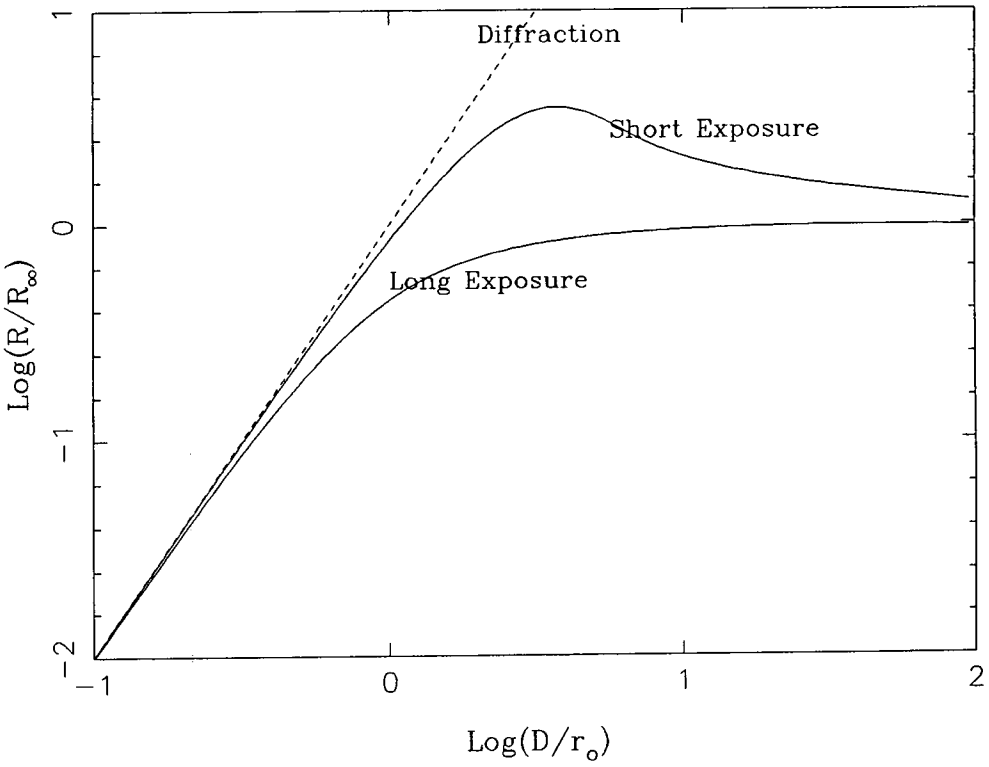

Figure 2.9: Normalised resolution versus aperture diameter for long and short exposure images.

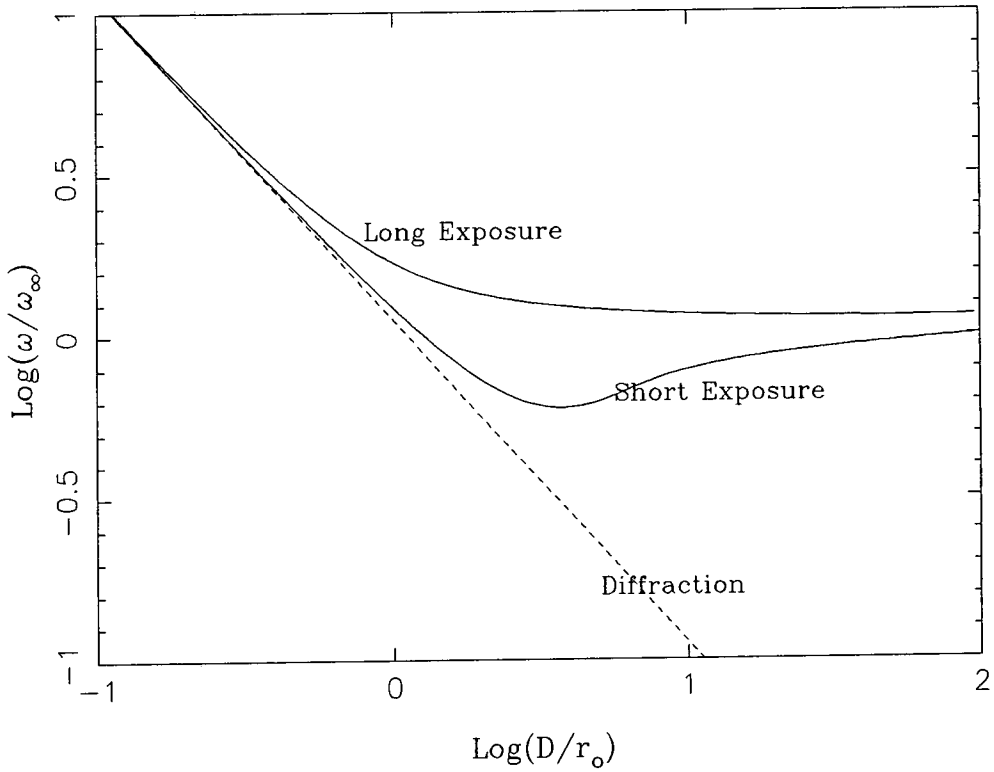

Figure 2.10: Normalised spread angle versus aperture diameter for long and short exposure images.

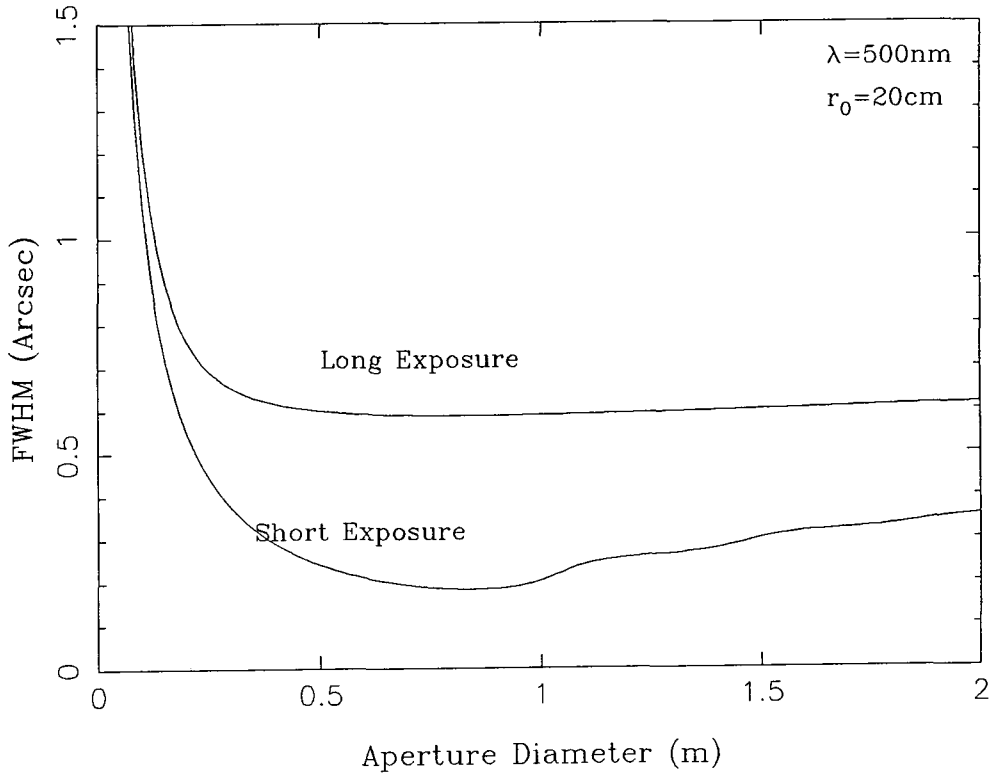

Figure 2.11: Full width half maxima for long and short exposure images with a coherence parameter value of 0.20 m.

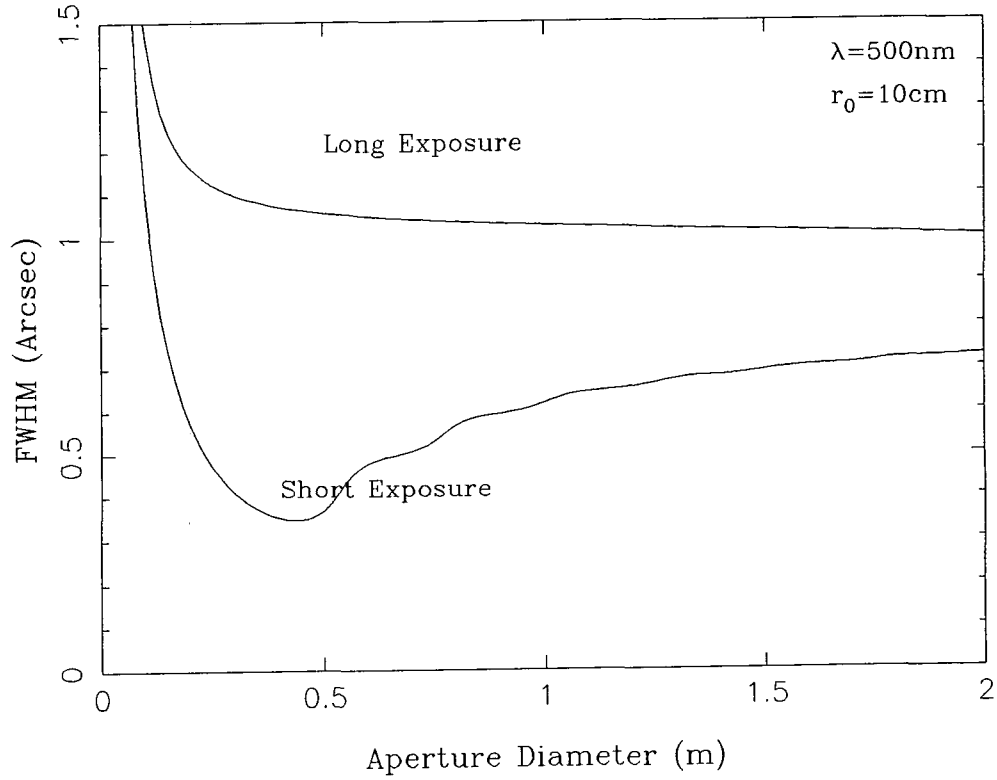

Figure 2.12: Full width half maxima for long and short exposure images with a coherence parameter value of 0.10 m.

the Strehl ratio for the long exposure image $S.R_{LE}$ is given as

$$SR_{LE} = \frac{\int_0^\infty OTF_{diff}(\rho)OTF_{LE}(\rho)d\rho}{\int_0^\infty OTF_{diff}(\rho)d\rho}, \tag{2.23}$$

and similarly the short exposure Strehl ratio $S.R_{se}$ is given as

$$SR_{SEN} = \frac{\int_0^\infty OTF_{diff}(\rho)OTF_{SEN}(\rho)d\rho}{\int_0^\infty OTF_{diff}(\rho)d\rho}. \tag{2.24}$$

In the case where the aperture is chosen to match the seeing condition such that the gain in resolution of short over long exposures is maximised (i. e. $D/r_o \simeq 4$), $S.R_{le}$ and $S.R_{se}$ are found to be to be 0.07 and 0.27 respectively.

2.4 Lucky Exposures

Both the previous sections on long and short exposures deal with the time averaged OTFs and PSFs that can be obtained. However, moments of seeing can arise where the corrugation of the wavefront is instantaneously almost negligible and the short exposure image obtained is effectively the diffraction limit of the aperture. If a final image is constructed which only includes such moments of seeing, an improvement in image quality closer to the diffraction limit can be attained. The probability of such 'lucky' exposures has been calculated by FRIED [16] as

$$\text{Prob} \approx 5.6 \exp\left[-0.1557\left(\frac{D}{r_o}\right)^2\right], \tag{2.25}$$

where Fried's definition of a lucky exposure is when the root mean squared distortion of a wavefront across the telescope aperture is less than one radian squared.

Table 2.1 shows the probabilities of obtaining a lucky exposure for a variety of D/r_o ratios. As can be seen the chances of getting a lucky exposure decreases rapidly with increasing value of the D/r_o ratio. This is to be expected since a large aperture effectively samples many different seeing cells and the probability that they combine to produce no significant distortion across a wavefront is small.

$\frac{D}{r_o}$	Probability
2	0.986 ± 0.006
3	0.765 ± 0.005
4	0.334 ± 0.014
5	$(9.38 \pm 0.033) \times 10^{-2}$
6	$(1.915 \pm 0.084) \times 10^{-2}$
7	$(2.87 \pm 0.57) \times 10^{-3}$
10	$(1.07 \pm 0.48) \times 10^{-6}$
15	$(3.40 \pm 0.59) \times 10^{-15}$

Table 2.1: Probability of lucky exposures for a variety of D/r_o ratios.

2.5 Outer Scale of Turbulence

In all the above calculations it has been assumed that the outer scale of turbulence is very much greater, and the inner scale of turbulence is very much smaller, than the aperture size of the telescope. In the case of the inner turbulence scale this assumption would seem reasonable since most estimates of l_o give a size of a few millimetres. However, atmospheric studies such as those described in §2.1 have shown that the outer scale of turbulence is typically only a few metres in size, and so the assumption made that $L_o \gg D$ is incorrect. In such a case, where the size of L_o should be taken into account, the power spectrum of the refractive index fluctuations may be more correctly given as

$$P_N(\mathbb{k}) = \frac{0.033 C_N^2 L_o{}^{\frac{11}{3}}}{(1 + k^2 L_o^2)^{\frac{11}{6}}}. \tag{2.26}$$

VALLEY [17] has shown that with such a power spectrum the structure function of the atmospheric refractive index variations is given by

$$D_\phi(\rho) = 3.69\left(\frac{r_o}{L_o}\right)^{-\frac{5}{3}}\left[1 - 0.994397\left(\frac{\rho}{L_o}\right)^{\frac{5}{6}} \mathrm{K}_{\frac{5}{6}}(\rho/L_o)\right], \tag{2.27}$$

where $\mathrm{K}_{\frac{5}{6}}(x)$ is the modified Bessel function. If this structure function is substituted into equation 2.13 of §2.2.1, the long exposure atmospheric optical transfer

function and hence the point spread function can be calculated for any particular value of L_o. Figures 2.13 and 2.14 show the FWHM of the long exposure image, as determined from the theoretical PSFs, plotted as a function of aperture size for several different outer scale of turbulence values. As can be seen the effect of a finite outer scale of turbulence is to reduce the expected FWHM of the long exposure image, and the size of this effect can be significant even at relatively large values of L_o. The effect of a finite outer scale of turbulence on the expected short exposure image has also been investigated by Valley, and he has shown that it can be assumed negligible unless the size of L_o is smaller than the aperture used for the observations.

Figure 2.15 shows a plot of the long exposure FWHM value obtained versus coherence parameter size for a 60 cm aperture, and for various values of L_o. The FWHM of the long exposure image can also be related to the standard deviation of image motion σ_m for a particular combination of r_o and L_o, the expected standard deviation being found using

$$\sigma_m^2 = 8\pi^3 \left(\frac{\lambda}{2\pi}\right)^2 r_o^{-\frac{5}{3}} \int_0^\infty \left[\frac{2\mathrm{J_o}(\pi D k)}{\pi D k}\right] \frac{L_o^{\frac{11}{3}}}{(1+k^2L_o^2)^{\frac{11}{6}}} k^2 dk. \qquad (2.28)$$

Figure 2.16 shows a plot of the long exposure FWHM against the standard deviation of image motion for L_o values of infinity, 100m, 10m, and 1m.

2.6 Coherence Parameter r_o

The value of the coherence parameter r_o provides a good measure of the seeing conditions since it is directly related to the height distribution of C_N^2 and hence to the turbulence. The physical significance of the coherence parameter can be understood in that it represents the diameter of a circular aperture over which the mean squared phase variation is approximately one radian squared. The value of r_o can also be thought of as the size of an aperture diameter at which the effects of seeing begin to dominate over those of diffraction.

The value of the coherence parameter can be determined using a variety of techniques. Assuming that the outer scale of turbulence L_o is very much greater than the size of aperture used for the observations, r_o can be estimated from the

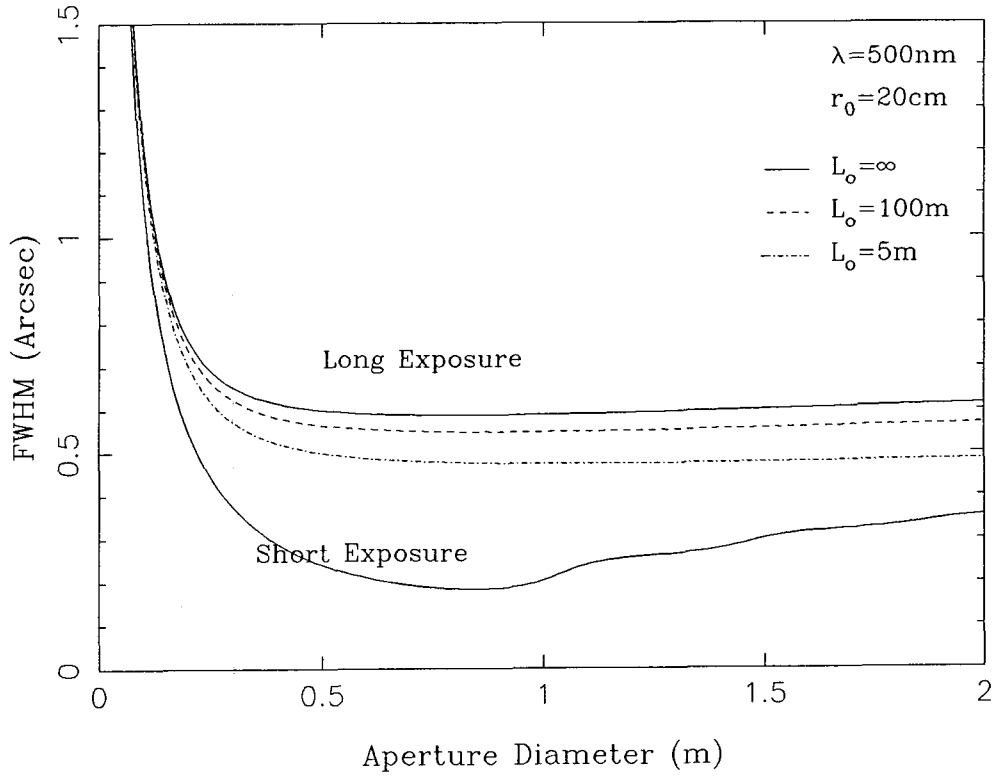

Figure 2.13: Full width half maxima of long and short exposures versus aperture diameter with an r_o of 0.2 m and for outer scale of turbulence of infinity, 100 m, and 5 m.

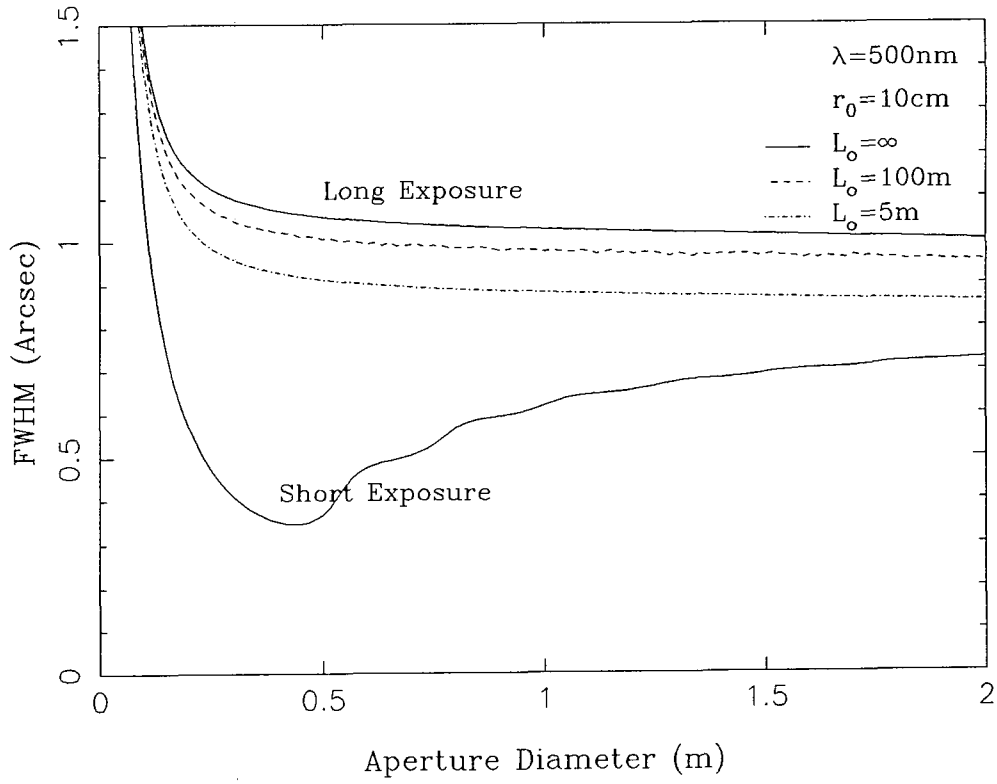

Figure 2.14: Full width half maxima of long and short exposures versus aperture diameter with an r_o of 0.1 m and for outer scale of turbulence of infinity, 100 m, and 5 m.

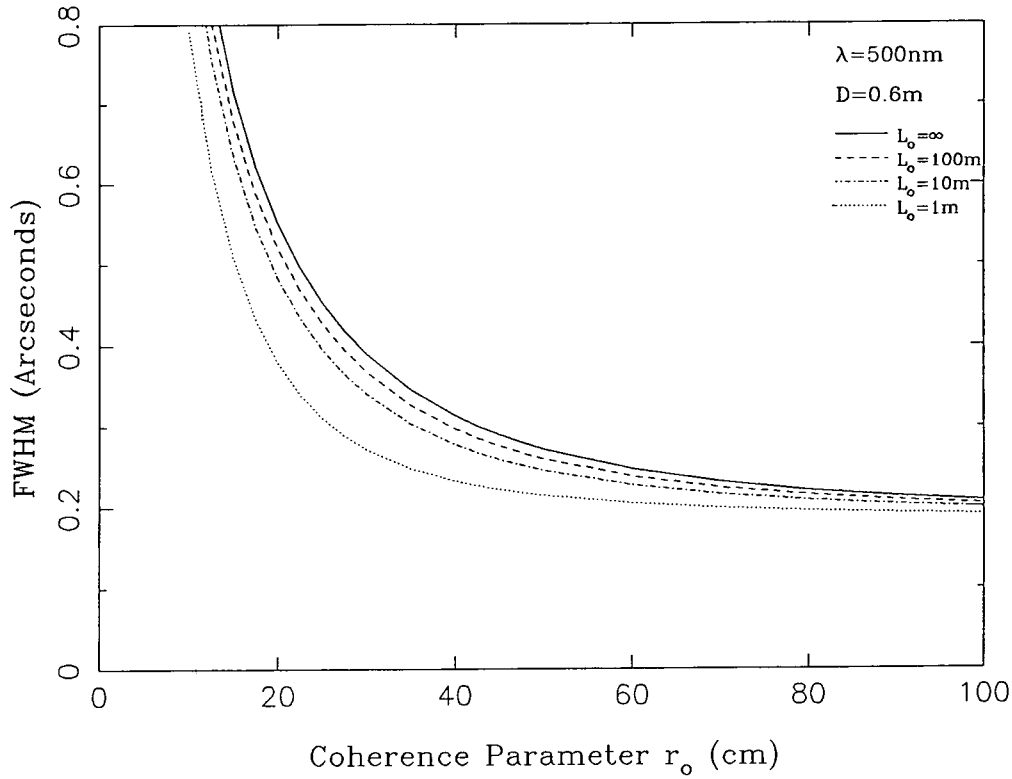

Figure 2.15: Full width half maxima of the long exposure image as a function of the coherence parameter, for outer scales of turbulence of infinity, 100 m, 10 m, and 1 m.

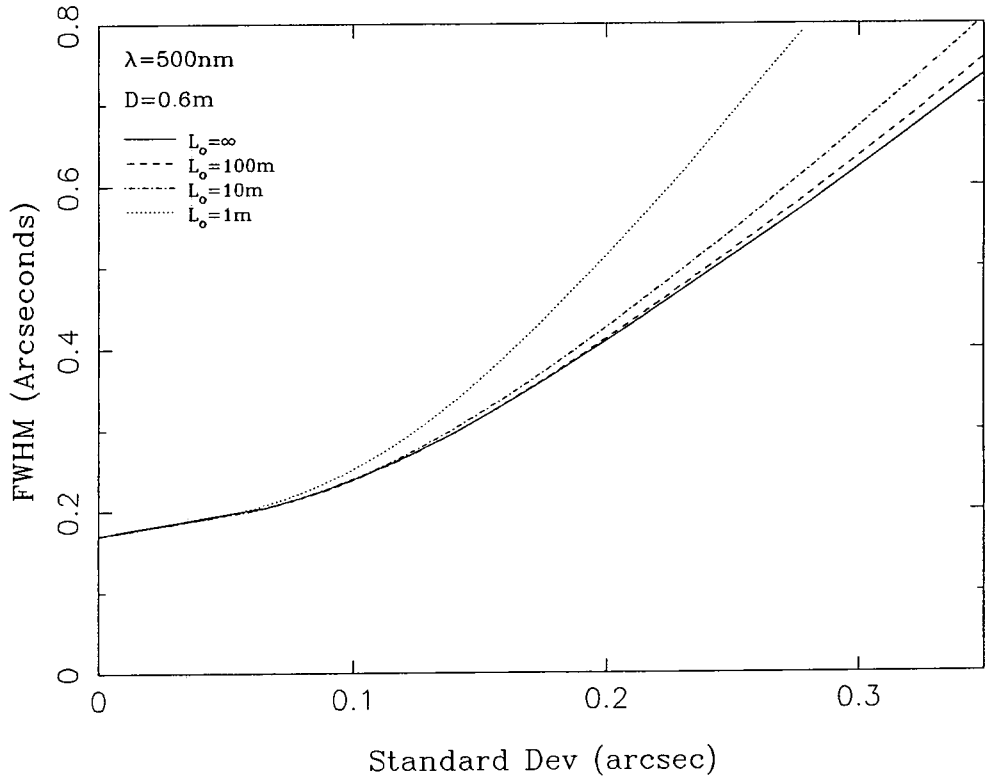

Figure 2.16: Full width half maxima of long exposure images versus the standard deviation of image motion for outer scales of turbulence of infinity, 100 m, 10 m, and 1 m.

long exposure FWHM of an image measured in arcseconds, using the relation

$$r_o \approx 2.0 \times 10^6 \frac{\lambda}{\mathrm{FWHM}}. \tag{2.29}$$

Again assuming that $L_o \gg D$, the r_o value can also be determined from the variance of the image centroid motion σ_m^2 where

$$\sigma_m^2 \simeq 0.36 \lambda^2 D^{-\frac{1}{3}} r_o^{-\frac{5}{3}}. \tag{2.30}$$

However, in the real case of astronomical observations the FWHM and mean squared centroid motion of the image will be affected by non atmospheric effects such as telescope shake and tracking errors, and by the finite size of the outer scale of turbulence. A better estimate of r_o is therefore obtained by considering the relative centroid motions of a star imaged though two separate apertures, since any common motion due to the telescope will be removed. If these apertures are separated by a distance α, the variance of the images' relative longitudinal motion σ_{lon}^2 is given by

$$\sigma_{lon}^2 = 2\left(\frac{\lambda}{r_o}\right)^{\frac{5}{3}} \left[0.179\left(\frac{\lambda}{D}\right)^{\frac{1}{3}} - 0.097\left(\frac{\lambda}{\alpha}\right)^{\frac{1}{3}}\right], \tag{2.31}$$

and that of their relative transverse motion σ_{lat}^2 by

$$\sigma_{lat}^2 = 2\left(\frac{\lambda}{r_o}\right)^{\frac{5}{3}} \left[0.179\left(\frac{\lambda}{D}\right)^{\frac{1}{3}} - 0.145\left(\frac{\lambda}{\alpha}\right)^{\frac{1}{3}}\right]. \tag{2.32}$$

A device which uses this technique to monitor seeing conditions is in regular use at the European Southern Observatory site at La Silla in Chile (see SARAZIN AND RODDIER [18]). The results from this instrument and from other studies utilising alternative techniques for determining r_o (MCINNES AND WALKER [19], MCINNES [20], and DUNLOP ET AL [21]) have shown that the value of r_o at a site of good astronomical seeing is typically 10 cm (~ 1 arcsecond seeing). However, periods with seeing conditions significantly better than this, with an $r_o > 15$ cm, would appear to occur quite regularly.

2.7 Isoplanatism

This is the term used in seeing theory to describe the degree of similarity between the seeing induced distortions of wavefronts coming from different sky directions.

The angular extent of sky over which these distortions can be assumed to be approximately the same is called the 'isoplanatic patch'. The size of this patch is of particular importance to high resolution imaging techniques that use a bright reference star to sense the atmospheric distortions. This is because the larger the isoplanatic patch size the further the reference star can be from the object of interest and thus the percentage of sky over which these techniques can be applied is increased.

If a simple model of seeing is assumed, where all the turbulence contributing to the wavefront distortions occurs at a height h above the observer, and wavefronts from two astronomical objects separated by an angle θ are compared in the aperture plane of a telescope (see figure 2.17), then FRIED [22] gives the size of the isoplanatic patch Ω to be

$$\Omega = 0.62\frac{r_o}{h}. \tag{2.33}$$

Using this definition the maximum allowable root mean squared optical path difference between the points on the two wavefronts at the aperture plane is $\frac{\lambda}{2\pi}$. Assuming a more realistic atmospheric turbulence model, where the turbulence is assumed to be distributed over a range of heights, the above equation becomes

$$\Omega = 0.62\frac{r_o}{\overline{h}} \tag{2.34}$$

where $\overline{h}$ is an average turbulent layer height defined by Fried as

$$\overline{h} = \left[\frac{\int_0^\infty h^{\frac{5}{3}} C_N^2(h)dh}{\int_0^\infty C_N^2(h)dh}\right]^{\frac{3}{5}}. \tag{2.35}$$

In order to calculate the expected size of the isoplanatic patch and average seeing height a distribution of the $C_N^2(h)$ value based on that of Hufnagel's 1978 model (see equation 2.7 of §2.1) was used. In the calculations the observer was assumed to be situated at an altitude of 2400 m (the height of the La Palma observatory) and table 2.2 shows the results obtained for the various $C_N^2(h)$ distributions as defined by the value of the upper atmosphere wind speed ratio parameter V/V_m used in the Hufnagel model. The values given in the table, however, are slightly misleading in that the true distribution of C_N^2 on a particular night does not follow the averaged distribution, as represented in the Hufnagel model, but instead tends to occur in layers at a variety of heights. Calculations with a more realistic C_N^2 distribution show that a larger isoplanatic patch is expected.

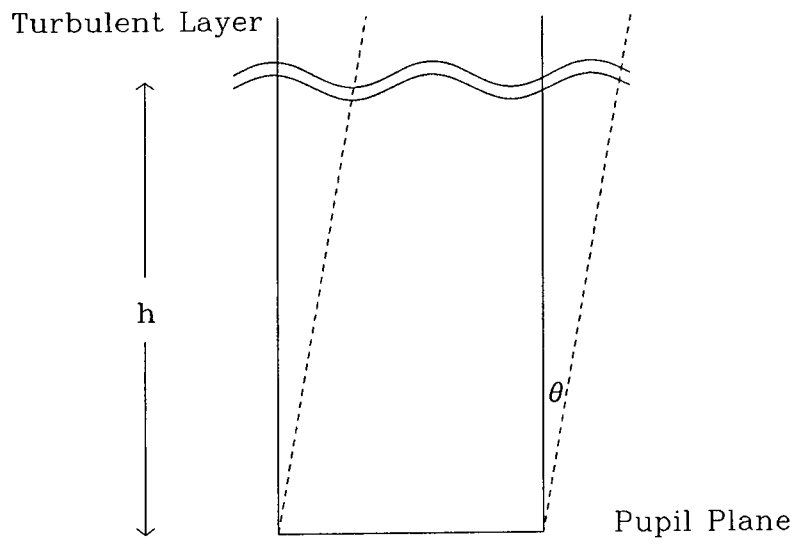

Figure 2.17: Configuration in which seeing is due to a single layer of turbulence and where the wavefront distortions are compared at the pupil plane of the telescope.

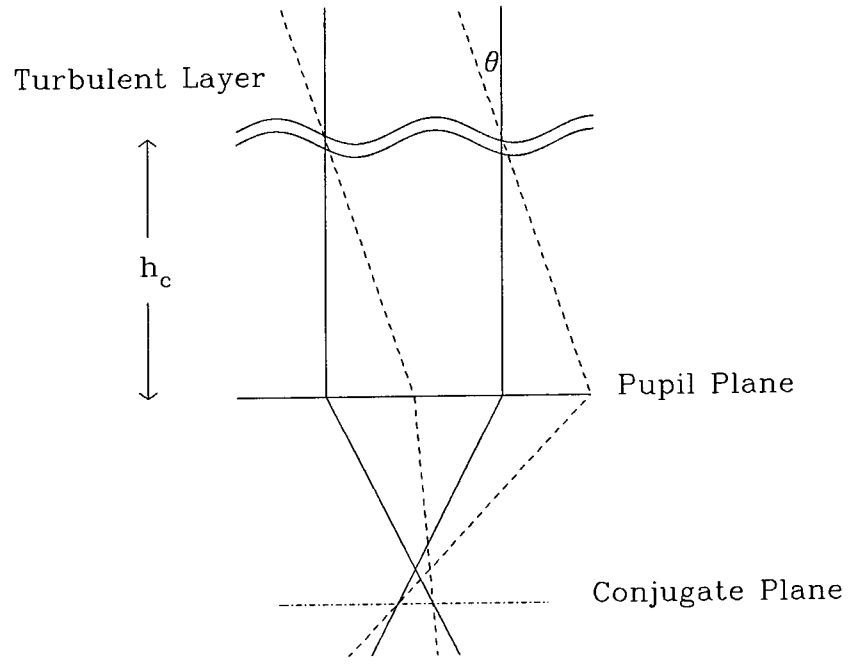

Figure 2.18: Configuration in which seeing is due to a single layer of turbulence and where the wavefront distortions are compared at a plane conjugate to a height in the atmosphere of h_c.

Wind Speed Ratio $\frac{V}{V_m}$	Average Seeing Height (km)	Isoplanatic Patch Size (arcsec)
0.00	1.9	6.73
0.25	3.4	3.76
0.50	5.4	2.37
0.75	6.7	1.91
1.00	7.4	1.72

Table 2.2: Average seeing height and isoplanatic patch size calculated using Hufnagel's model for the C_N^2 distribution and an r_o value of 0.10 m.

The above definitions of isoplanatic patch size apply for wavefronts compared at the aperture plane of the telescope. If instead, the wavefront distortions are considered in a sub-aperture positioned downstream of the telescope focus at a point conjugate to a height h_c in the atmosphere (see fig 2.18), the equations given above must be modified. Assuming again a simple model of atmospheric turbulence, where all the turbulence occurs at a height h, the isoplanatic patch size is given analogous to equation 2.33 as

$$\Omega = \frac{0.62 r_o}{|h - h_c|}. \tag{2.36}$$

In particular it can be seen that if the turbulent layer is at h_c the isoplanatic patch is infinitely large, or rather will only be limited by the telescope's field of view. This case is particularly relevant to adaptive optics as the position of the plane of wavefront correction can be arranged to minimise the average height term and thus increase the isoplanatic patch size. With a single layer model of atmospheric turbulence distribution, equation 2.36 can be used to calculate the isoplanatic patch size for any particular combination of h_c and turbulent layer height and figure 2.19 shows the variation of isoplanatic patch size with height of the turbulent layer, for a variety of different h_c values. The advantage in having the correction plane at a conjugate focus position instead of at the aperture plane

can be clearly seen in that the range is increased of the heights at which the turbulent layer can be situated and the isoplanatic patch remain large. This can be extended to a more realistic model of turbulence distribution in a similar way as before, but with the average seeing height now being given (see appendix A) as

$$\overline{h} = \left[\frac{\int_0^{h_c} |h - h_c|^{\frac{5}{3}} C_N^2(h) dh}{\int_0^{\infty} C_N^2 dh} \right]^{\frac{3}{5}}. \tag{2.37}$$

If a continuous distribution of the refractive index constant is assumed based on that of the model given by Hufnagel and this is applied to the La Palma observatory site; equation 2.37 can be used to determine the position of the conjugate height at which the average turbulent layer height is minimised. Table 2.3 shows the optimum height above the observer the image correction plane must be conjugate to in order to minimise $\overline{h}$, for various distributions of $C_N^2(h)$. The table also shows the theoretical isoplanatic patch size that would be obtained; calculated using equation 2.36 and assuming an r_0 of 0.10 m.

Wind Speed Ratio $\frac{V}{V_m}$	Optimum Conjugate Height (km)	Average Turbulent Layer Height (km)	Size Of Isoplanatic Patch (arcsec)
0.00	1.3	1.3	9.47
0.25	2.1	2.7	4.74
0.50	3.9	3.9	3.28
0.75	5.6	4.1	3.12
1.00	6.6	4.0	3.20

Table 2.3: Optimum position of conjugate height and isoplanatic patch size for various $C_N^2(h)$ distributions.

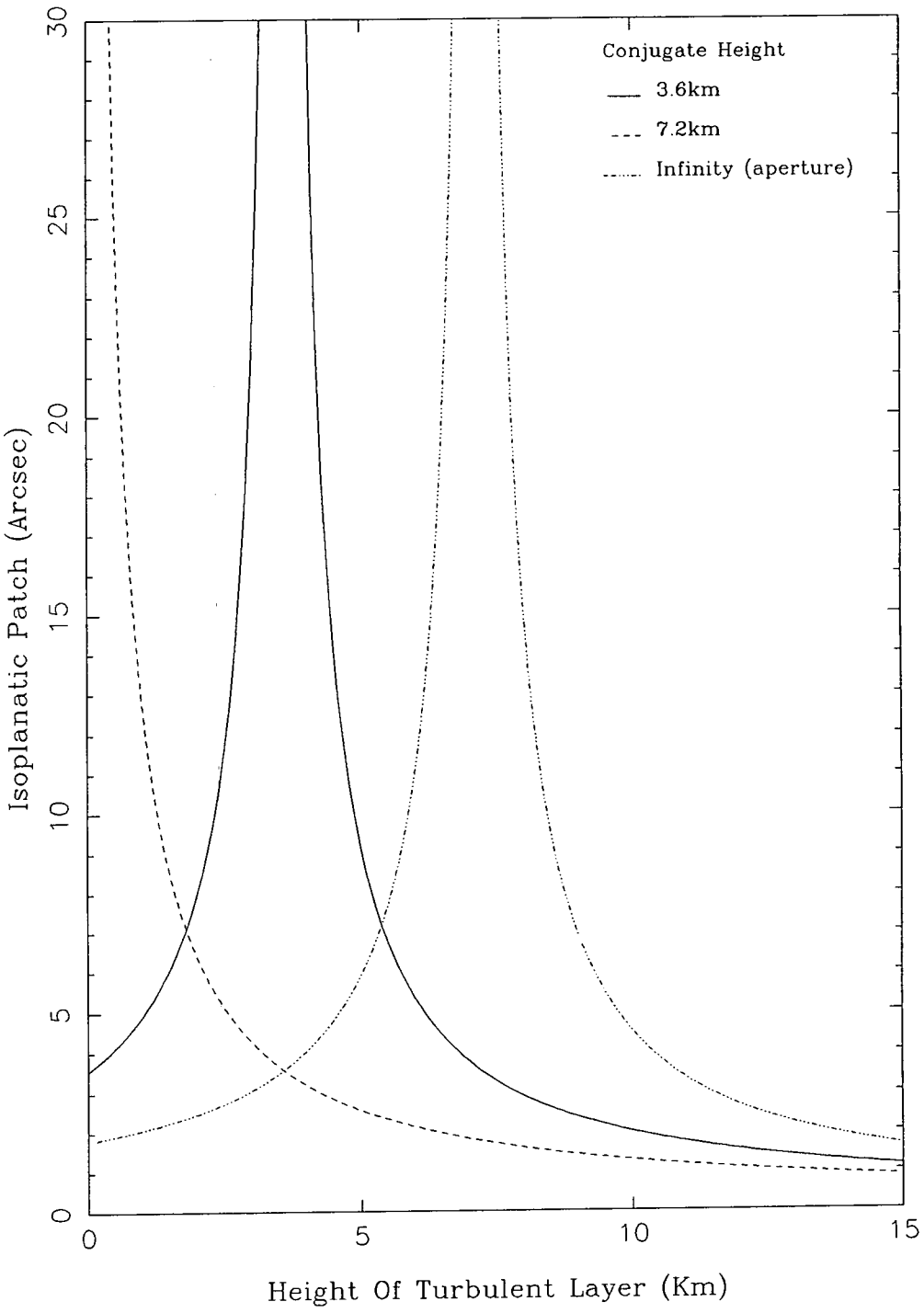

Figure 2.19: Size of isoplanatic patch as a function of turbulent layer height for several different conjugate focus positions of the wavefront correction plane and an r_o value of 0.10 m.

2.8 Power Spectra Of Image Motion

The Power Spectrum Density (PSD) per unit area $\mathrm{P_a(k)}$ as measured through a circular aperture of diameter D has been shown by MARTIN [23] to be related to the power spectrum of atmospheric refractive index variations $\mathrm{P}_\phi(\mathbf{k})$ by

$$\mathrm{P_a(k)} = \left(\frac{\lambda}{2\pi}\right)^2 [2\pi(k_x \cos\theta + k_y \sin\theta)]^2 \left[\frac{2\mathrm{J}_1(\pi Dk)}{\pi Dk}\right]^2 \mathrm{P}_\phi(\mathbf{k}), \tag{2.38}$$

where θ is the angle between the cross wind direction and the axis chosen along which the standard deviation of image motion is measured, and $\mathrm{J}_1(x)$ is the first order Bessel function.

To calculate the power spectrum density per unit time of image motion $\mathrm{P_t}(f)$, where f is the frequency in Hertz, the 'Taylor hypothesis' is adopted which assumes that the refractive index variations in the atmosphere can be regarded as 'frozen' and that the motion of a star image is caused by these variations being blown across the telescope aperture at the mean wind velocity of the turbulent layers. If the image motion is measured with a finite exposure time τ the PSD per unit time is given by Martin as

$$\mathrm{P_t}(f) = \frac{2}{V_{cw}} \left[\frac{\sin f\tau}{f\tau}\right]^2 \int_{-\infty}^{\infty} \mathrm{P_a}(q)\, dq, \tag{2.39}$$

where V_{cw} is the cross wind velocity, and $q = \left(k_x^2 + \left(\frac{2\pi f}{V_{cw}}\right)^2\right)^{\frac{1}{2}}$.

Figure 2.21 shows the one-sided PSDs obtained for a variety of different cross wind conditions, the measurement of the PSD is assumed parallel to the wind direction. It can be seen that all the curves behave as $f^{-\frac{2}{3}}$ at low frequencies, whilst at high frequencies the curves switch to a $f^{-\frac{8}{3}}$ behaviour, the change over occurring at a frequency of $f \simeq 0.2\frac{V_{cw}}{D}$.

Martin has also investigated the effect of the length of the exposure time used for the observations on the image motion recorded. He has shown that the ratio of the measured variance of image motion to the actual variance is given by

$$\begin{aligned}\frac{\sigma^2_{meas}(\frac{V_{cw}\tau}{D}, \theta)}{\sigma^2_{abs}} &= \frac{1}{2.361} \int_0^{\infty} q^{-\frac{2}{3}} \left[\frac{2\mathrm{J}_1(\pi q)}{\pi q}\right] dq \\ &\times \frac{1}{\pi} \int_0^{2\pi} \cos(\phi - \theta)\, \mathrm{sinc}^2\left(q \cos\phi \left(\frac{V_{cw}\tau}{D}\right)\right) d\phi. \end{aligned} \tag{2.40}$$

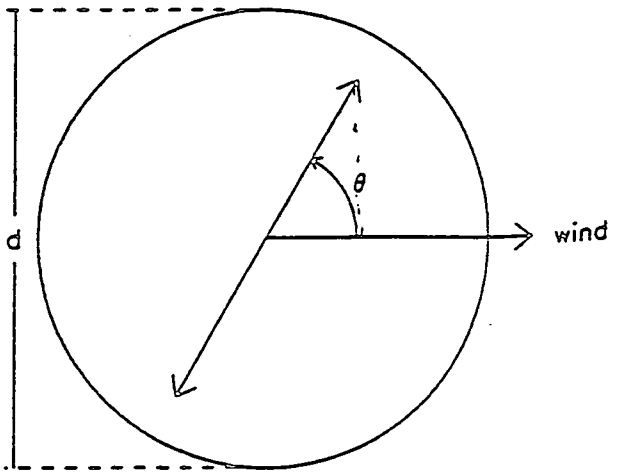

Figure 2.20: Definition of variables for the measurement of absolute image motion. The x-axis is defined to be parallel to the wind direction. Image centroids are measured along the axis represented by the two headed arrow (from Martin [23]).

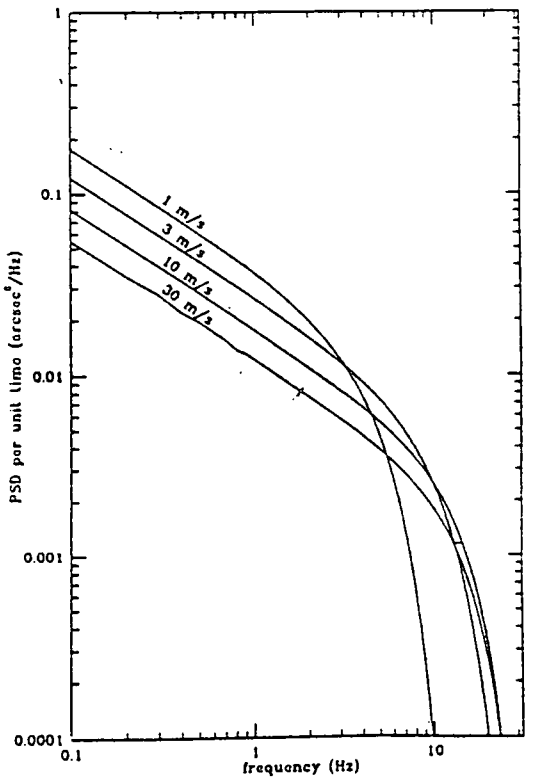

Figure 2.21: Power spectral density per unit time of image motion for several crosswind velocities, measured along an axis parallel to the wind direction (from Martin [23]).

The value of this ratio only depends on the quantity $\frac{V_{cw}\tau}{D}$ and on the angle the wind direction is to axis along which motion is measured. A plot of this ratio against $\frac{V_{cw}\tau}{D}$ for several different values of θ is shown in figure 2.22. It can be seen that to keep the estimation of $\frac{\sigma^2_{meas}}{\sigma^2_{abs}}$ greater than 0.95, the value of $\frac{V_{cw}\tau}{D}$ must be less than one, leading to a maximum exposure time of

$$\tau \simeq \frac{D}{V_{cw}}. \tag{2.41}$$

To calculate this exposure time the cross wind velocity of the turbulent layer must be known. Martin gives that cross wind velocities are typically between 10–40 ms^{-1} at a height of 12 km and a few metres a second at ground level. Therefore depending on where the turbulent layer is situated, the maximum allowable exposure time for a typical seeing matched aperture of 60 cm aperture, is a few tens to several hundred milliseconds in length.

All the above calculations assume that the seeing motion is produced by a single turbulent layer. If a more realistic model of atmospheric turbulence is considered, however, with the seeing being due to a distribution of turbulent layers, each with an associated cross wind velocity, equation 2.39 should then be more properly be written as

$$P_t(f) = \frac{2\int_0^\infty C_N^2(h){V_{cw}}^{-1}(h)\left[\left[\frac{\sin f\tau}{f\tau}\right]^2 \int_{-\infty}^{\infty} P_a(q)du\right]dh}{\int_0^\infty C_N^2(h)dh}. \tag{2.42}$$

The effect of this multilayer structure on the observed power spectrum is to remove the sharp change over in behaviour and to replace it with a more extended region of change over between the two extremes of behaviour where the power spectrum shows an approximately $f^{-\frac{5}{3}}$ dependency. Such behaviour has been observed by CHRISTIAN AND RACINE [24] (see figure 2.23), who measured the power spectra of star motion using a star trail technique.

2.9 Conclusions for Adaptive Image Sharpening

It can be seen from this chapter that there is considerable more spatial frequency information available than can be obtained from simple long exposure images of astronomical objects. The section on short exposure imaging shows that substantial

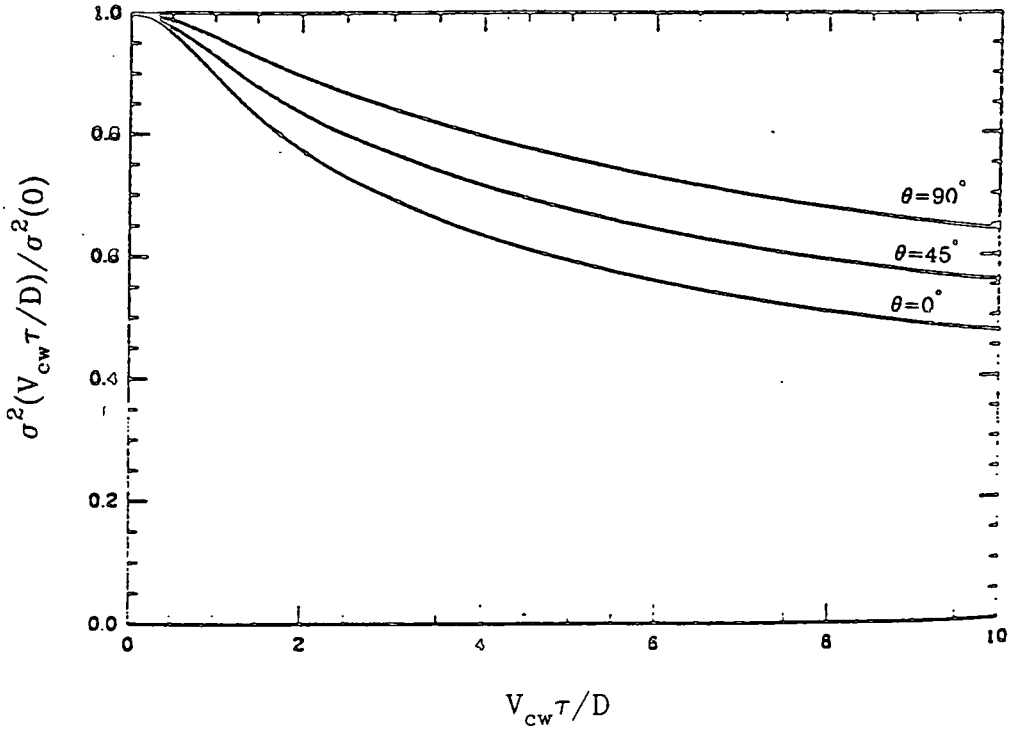

Figure 2.22: Ratio of the measured variance of the image motion to the actual variance (from Martin [23]).

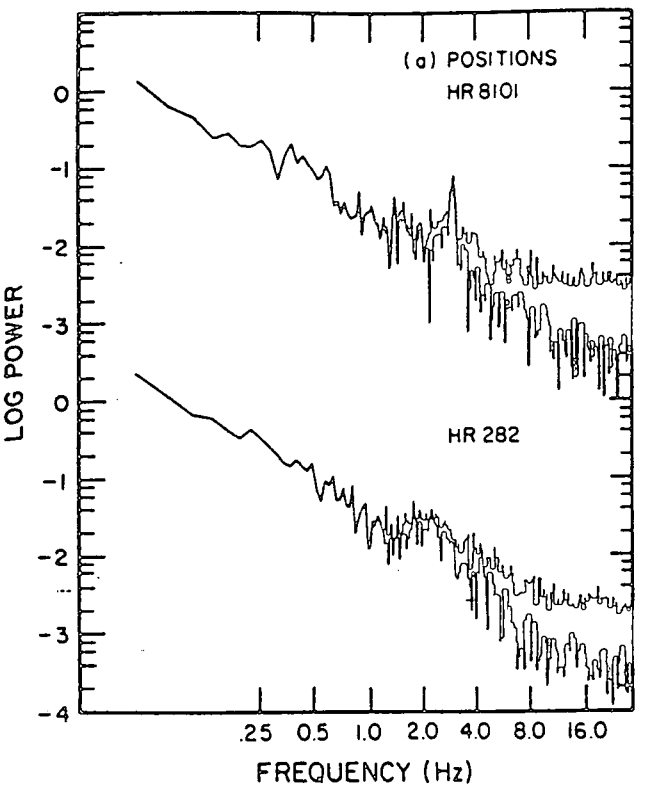

Figure 2.23: Power spectral density per unit time of image motion (from Christian and Racine [24]).

improvements in the image quality can be achieved by just removing the overall phase (tilt) of a wavefront across an aperture. Using this technique, if the aperture chosen is matched to the seeing conditions ($D/r_o = 4$), a possible maximum threefold improvement in the FWHM of an image can be obtained. A further improvement of the image towards the diffraction limit of the aperture used could be achieved by making use of the occurrence of lucky exposures and only including these moments of seeing in the final image.

If the wavefront tilt is removed by the technique of adaptive optics, the times scales at which the corrections need to be applied to effectively remove the tilt induced image motion, can be seen from equation 2.41 of §2.8 to be governed by the cross wind velocities of the turbulent layers and the aperture size used for the observations. Assuming a value for the cross wind velocity of between 10–30 ms^{-1} and a seeing matched aperture size of 60 cm, the required frequency of tilt removal is of the order of 10–50 Hz.

It should be noted, however, that the factor of three improvement in image FWHM hoped to be gained by the application of wavefront tilt correction is really an upper limit to that which can be achieved. If the outer scale of turbulence is of the order of a few metres in size, as experimental determinations would seem to suggest, then the effects of the atmosphere on the image quality might well be overestimated and the gains that can result from wavefront tilt removal may not be as large as predicted. It should also be mentioned that the theories of atmospheric seeing take no account of such effects as 'dome' and 'mirror' seeing, or effects due to inaccuracies in mirror figuring and optical alignment of the telescope.

The results of §2.7 would seem to suggest that the size of the isoplanatic patch (a few arcseconds) imposes severe limitations on adaptive optics sharpening. However, the definitions of the isoplanatic patch given only really apply if full wavefront correction is attempted. In adaptive techniques where just the overall tilt of a wavefront is removed, the size of the sky area around a guide star over which significant improvements are gained, is expected to be tens of arcseconds. This is discussed more fully in the next chapter.

Chapter 3

Image Sharpening

3.1 Techniques of High Resolution Imaging

It can be seen from the preceeding chapter that for a telescope aperture greater than about ten centimetres the effects of atmospheric turbulence become the dominating factor in determining the obtainable resolution of astronomical images. If these atmospheric effects could be removed a great improvement in image quality would be attained. Over the last twenty years the theory of atmospheric turbulence has become more thoroughly understood. This understanding coupled with the progress in modern photon counting detectors and computing technology, has led to the development of a variety of techniques that seek to retrieve the information lost due to the atmospheric deterioration of astronomical images.

3.1.1 Classical Interferometry

Interferometric methods were first applied to achieve high resolution at optical wavelengths by MICHELSON AND PEASE [25], who measured the visibility of the fringes produced between the images of an object formed by two separate apertures, as a function of the aperture separation. The visibility V of the fringes being given by

$$V = \frac{I_{max} - I_{min}}{I_{max} + I_{min}}, \tag{3.1}$$

where I_{max} is the peak, and I_{min} the minimum fringe intensity. Using the variation in visibility versus aperture separation, Michelson and Pease were able to obtain

measurements of the angular diameters of nearby giant stars.

To minimise the effects of atmospherically induced phase variations across an aperture, the size of the apertures used in this technique are of the order of the coherence parameter r_o. There will, however, still be a random tilt of the wavefront, causing the fringes formed to be in constant motion. To avoid this problem more modern developments of this technique (see SHAO ET AL [26]) use fast wavecompensation systems, similar to those discussed later, to remove these aperture tilts.

In the classical Michelson technique the fourier space occupied by the object is sampled one point at a time and only in one direction, thus the reconstruction of non-symmetrical objects is impossible. In the technique of 'Multiple Aperture Synthesis', as suggested by ROGSTAD [27], and RHODES AND GOODMAN [28], a system of N apertures allows N(N-1)/2 baselines to be measured simultaneously and the fourier space of the object can then be reconstructed. The apertures used can either be an array of sub-apertures on a larger telescope or a system where several separate telescopes are optically linked, such as that planned for the European Southern Observatory's Very Large Telescope array (VLT). Partial fourier phase information may be recovered by the application of 'Phase Closure', the feasibility of which has been shown experimentally by BALDWIN ET AL [29]. Using this technique high resolution images of several astronomical objects have been reconstructed (HANIF ET AL [30]).

3.1.2 Shear Interferometry

This is an alternative method of sampling the fourier space where the pupil plane image of a wavefront from an object is divided by a beamsplitter into two equal amplitude parts, which are then recombined in such a way as to produce interference fringes. The visibility of the fringes can then be measured and used to reconstruct the fourier transform of the object. One such instrument designed to utilise this technique is the reversing or folding interferometer as used by DAINTY AND SCADDEN [31], where one of the wavefront images is folded back on itself before being recombined with the other unaltered image. This device has some disadvantages; firstly in that the size of the shear is fixed and thus cannot be

matched to the seeing conditions and so fringes are formed in just the central portion of the final image; secondly that for any one particular measurement the given shear is only in one direction so that reconstruction of two dimensional objects requires exposures to be taken with different orientations of the instrument. A device which avoids these problems is the rotational shear interferometer as suggested by BRECKINRIDGE 32], where the two beamsplit wavefront images are rotated through an angle with respect to each other and then recombined so as to produce fringes. The degree of rotation can be adjusted to match the seeing conditions so that the fringes are formed right across the final image. Since shears in all directions are present in this final image the two-dimensional spatial intensity distribution of an observed object can be reconstructed from the fringe visibility variation. RODDIER AND RODDIER [33] have successfully used such a rotating shear interferometer to investigate the structure of several nearby giant stars.

3.1.3 Speckle Interferometry

The technique of 'Speckle Interferometry', first introduced by LABEYRIE [34], takes advantage of the fact that the mean squared fourier transform $\langle|\mathrm{I}(f)|^2\rangle$ of a series of short exposure images of an object, is given by

$$\langle|\mathrm{I}(f)|^2\rangle = \langle|\mathrm{O}(f)|^2\rangle\langle|\mathrm{S}(f)|^2\rangle, \tag{3.2}$$

where $\mathrm{O}(f)$ and $\mathrm{S}(f)$ are, respectively, the fourier transforms of the object intensity distribution and that of the atmosphere. Since $\mathrm{I}(f)$ can be experimentally measured, and $\mathrm{S}(f)$ can be determined from either a model fit or from an simultaneous observation of a nearby point source, the squared modulus of object's intensity distribution can be determined. This technique has been widely used, particularly in measuring the angular diameters of nearby stars (e. g. GEZARI ET AL. [35]), and in determining the separations of close binaries.

Knowledge of the phase of an object is, however, lost using the above method and modifications to the technique have been proposed in order to retrieve this information. 'Speckle Holography,' suggested by BATES ET AL [36], uses a nearby reference star to reconstruct the structure of the object, whilst KNOX AND THOMPSON [37] suggested using the statistical autocorrelation of the image transform ('Speckle Imaging'). More recently WEIGELT [38] has put forward the technique

of 'Speckle Masking', which involves computing the triple correlations of the short exposure images to obtain the phase information. A good review of the various techniques of speckle interferometry is given by AITKEN [39].

3.1.4 Post-exposure Centroid Superposition

High resolution images can also be obtained by the post-exposure software centroid superposition of short exposure images. The maximum theoretical improvement of the image obtained, occurs if the aperture used for the short exposure observations is matched to the seeing conditions (i.e. $D/r_o = 4$). This technique has been successfully used by a number of groups to sharpen images of extended astronomical objects (HECQUET AND COUPINOT [40], FUENSALIDA ET AL. [41], REDFERN [42]). A further sharpening of the images can be attained if 'lucky exposures' are taken advantage of and frame selection used to only include moments of good seeing in the final image (see LELIÈVRE ET AL. [43]).

The drawback to this post-exposure method of image sharpening is the vast amount of data that must be stored in order to later reconstruct images and the poor quantum efficiency and non-uniformity of the detectors at present used to record the short exposure images.

3.2 Adaptive Optics Image Sharpening

The term 'adaptive optics' is applied to describe any image sharpening technique that tries to remove part or all of the atmospherically induced phase variations of a wavefront across an aperture by means of a rapidly guided wavefront distortion compensating system. In adaptive optics the wavefront corrections are capable of being applied at high frequencies ($> 10\,\mathrm{Hz}$) and this is what distinguishes it from the term 'active optics' which is now taken to mean optical systems where corrections are applied only at low frequencies (a few Hz).

There are basically two approaches to adaptive optics image sharpening which are currently in the process of being implemented on large telescopes. In one approach the instrument is designed to remove the general phase (tilt) of a wavefront

across an aperture, whilst the other main approach is to correct all the phase variations across a wavefront and not just the general tilt. In both methods a bright reference ('guide') star is required close to the astronomical object being observed, this guide star being used to sense the wavefront distortions.

3.2.1 Wavefront Tilt Correction

It has been calculated by FRIED [12] that the mean square wavefront error Δ given in radians for an atmospherically distorted wavefront across a circular aperture of diameter D is

$$\Delta = 1.030\left(\frac{D}{r_o}\right)^{\frac{5}{3}}. \tag{3.3}$$

If the tilt component of the wavefront distortion across the aperture is removed, the residual wavefront error $\Delta_{T.C}$ reduces to

$$\Delta_{T.C} = 0.134\left(\frac{D}{r_o}\right)^{\frac{5}{3}}. \tag{3.4}$$

So it can be seen that wavefront tilt contributes significantly to the overall wavefront distortion and the correction of this term alone can provide a large improvement in the final image quality. This removal of wavefront tilt is analogous to the superimposition of short exposure images for which the expected improvement in the corrected full width half maximum over that of unguided long exposures is shown in figures 2.11 and 2.12 of chapter 2. A decrease in the size of the FWHM by a maximum factor of three can be seen to be achievable if the size of the aperture is chosen to be optimal at a diameter of approximately four times the coherence parameter r_o.

The tilt of the distorted wavefront is usually determined by the real-time sensing of the centroid position of an image of a bright guide star. The detected wavefront tilt is then removed by applying an opposite tilt to an actively controlled plane mirror. Since the optimum aperture for typical seeing conditions ($r_o \approx$ 10–20cm) is only between 40–80 centimetres in diameter, to utilise the full aperture of a large telescope a mask of a number of sub-apertures must be used, each with its own tilt correction system; the stabilised output from each aperture being recombined to form the final image.

The position of the guide star image centroid has to be determined in a short enough time interval in order that the seeing motion of the star is effectively 'frozen', such that the centroid position gives the instantaneous overall tilt of the wavefront across the telescope aperture. Due to the need that sufficient photons arrive within this time interval to determine the image centroid accurately, limitations are imposed on the magnitude of the guide star. With the efficiency of detectors currently available, the limit on the faintest star that can be used as the reference object for this image sharpening technique is approximately 13^{th} magnitude (see appendix C).

3.2.2 Full Wavefront Correction

This technique attempts to remove the smaller scale wavefront phase distortions across an aperture as well as the overall tilt; the distortions generally being removed by the action of a single flexible mirror or a large number of small tip-tilt mirrors. This approach means that the full aperture of a telescope can be utilised and should, neglecting seeing induced amplitude variations in the wavefront, enable full diffraction limited images to be obtained. The scales on which the wavefront needs to be corrected to achieve such diffraction limit images has been investigated by HUDGINS [44] who has shown that the residual mean square wavefront error after correction, for a system that has effectively n correction elements across the mirror, is given by

$$\Delta_R = K\left(\frac{D}{nr_o}\right)^{\frac{5}{3}}, \tag{3.5}$$

where K is a constant which depends on the response function of the individual corrector elements (for a continuous flexible mirror $K \sim 0.2$). The Strehl ratio of the corrected image central intensity to that of the diffraction limit can then be determined using the relation

$$S.R. \simeq \exp(-\Delta), \tag{3.6}$$

Thus if the aim is to achieve at visible wavelengths a Strehl ratio after correction of 80%, and assuming a typical r_o value of 0.10 cm; for a 4 m telescope this would require that n would have to be approximately 40 (i.e. element size $\sim r_o$), thus requiring ~ 1600 correction elements for the whole mirror. Such a system would

be complicated and expensive to build so most of the devices which attempt full wavefront correction are designed to work at infra-red wavelengths where the value of r_o is greater and thus fewer correction elements are required.

The method that is used to sense the wavefront distortions across the aperture is generally based on a Hartmann-Shack detector arrangement, which divides the aperture into a number of separate sections using an array of small lenslets. The diameter of each section is matched to the size of the wavefront correction elements. The images formed by each separate lens are then sensed with a suitable detector and their positions used to establish the tilt of each segment of the wavefront. These individual tilts can then be used to determine the overall shape of the distorted wavefront and this distortion is then corrected by the wavefront compensation system. The main disadvantage of this technique is that because the seeing distortions are sensed on scales of approximately r_o instead of $4r_o$, a three magnitudes brighter guide star is required than for aperture tilt correction.

3.2.3 Sky Coverage

The limits imposed by the guide star magnitudes mean that at optical wavelengths and under typical seeing conditions the percentage area of sky with a suitable star within the isoplanatic patch as given by equation 2.33 of chapter 2 is only about 3%. However, this definition of isoplanatic patch size is really only applicable if near total correction of the distorted wavefront is required and in fact a significant improvement in the image quality can be made over a larger sky angle if less stringent criteria are applied. For example, if just the wavefront tilt across an aperture is being removed the sky angle over which image improvement extends is expected to be much higher. The reason for this is that the lower spatial frequency wavefront distortions such as tilt have a greater coherence length than the higher frequency distortions responsible for small scale wavefront corrugation.

The expected size of the isoplanatic patch for tilt correction has been investigated by VALLEY [45,46]. Valley derived an expression for the modulation transfer function $\mathrm{MTF}_{\mathrm{iso}}(\rho, \theta)$ due to tilt decorrelation at an offset angle θ from the guide star, and used this to define a quantity called the isoplanatic relative intensity

$I_{rel}(\theta)$ given as

$$I_{rel}(\theta) = \frac{\int_0^1 MTF_{ap}(\rho)\, MTF_{atm}(\rho)\, MTF_{iso}(\rho,\theta)\, d\rho}{\int_0^1 MTF_{ap}(\rho)\, MTF_{atm}(\rho)\, d\rho}. \tag{3.7}$$

A plot of the isoplanatic relative intensity versus offset angle for various seeing conditions is shown in figure 3.1. The value of the isoplanatic relative intensity rapidly decreases at angles away from $\theta = 0$, but it can be seen that wavefront tilt removal produces an improvement in image quality over that of the uncorrected long exposure image for isoplanatic angles as great as several tens of arcseconds. These results agree well with the those given by COWIE AND SONGALIA [47] who have calculated that the limitation on the size of the isoplanatic patch over which tilt correction is expected to provide an image improvement is

$$\Omega_{t.c} < \frac{4r_o}{\overline{h}}, \tag{3.8}$$

where $\overline{h}$ is the average turbulent layer height as defined by equation 2.35 of chapter 2.

An interesting fact that emerges from these calculations of isoplanatism is that the degree of the wavefront tilt correlation decreases more rapidly in the radial direction from the centre of a chosen field than in the transverse direction. This leads to an effect, noticed by some observers, that the tilt corrected images of field stars away from the guide star appear radially distorted.

The limited area of sky that can be observed at optical wavelengths, even if just tilt correction is being attempted, is still a major drawback to adaptive optics image sharpening. To overcome this problem it has been suggested by FOY AND LABEYRIE [48] that instead of using a real star, the reference object could be an artificial star created by stimulating the sodium ions in the upper atmosphere with a high power tunable frequency laser. Experiments into the feasibility of creating such a system have been successfully conducted by THOMPSON ET AL. [49] and by FOY [50]; though the implementation of a full image correction system incorporating such a technique still requires extensive research and development.

An alternative method that has been proposed to increase the sky coverage is to position the plane of wavefront correction at the conjugate focus of the atmospheric

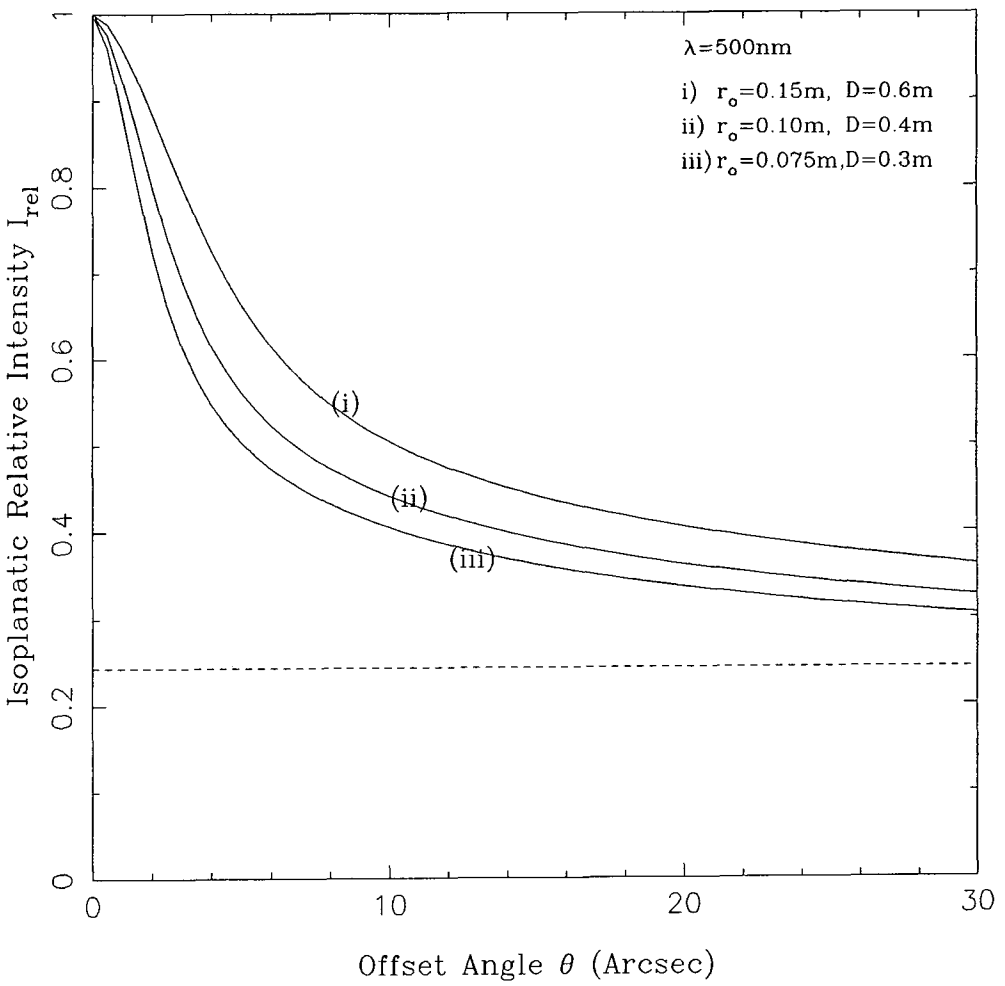

Figure 3.1: Isoplanatic relative intensity as a function of offset angle θ for various values of r_o with Fried matched apertures (after Valley [46]). The model used in the calculations for the distribution of the refractive index structure constant is that of Hufnagel [8], with a V/V_m ratio of 1.0. Also shown (dotted line) is the Strehl ratio of the short exposure tilt corrected image to the uncorrected long exposure image at $\theta = 0$.

turbulence. As shown in § 2.7 of chapter 2, if the seeing is dominated by a single layer of turbulence, then correct positioning of the correction plane would produce an infinitely large isoplanatic patch. In practice, however, this is not achievable since seeing is generally due to turbulent layers at a variety of heights. Nevertheless the optimum positioning of the correction plane so as to minimise the average turbulent layer height $\overline{h}$, can produce an increase in the size of the isoplanatic patch. A development of this idea that has been suggested by BECKERS [51], is that wavefront correction could be applied at multiple conjugate positions each corresponding to a layer of major turbulence.

3.2.4 Adaptive Optics In the Infra-red

Interest has arisen in applying adaptive optics at near infra-red wavelengths and the reason for this is that there are considerable advantages to be gained at working at these wavelengths. It can be seen from the preceding chapter (equation 2.15) that the size of the coherence parameter r_o is proportional to $\lambda^{\frac{6}{5}}$, thus r_o is larger at longer wavelengths and the size of the isoplanatic patch, which is proportional to r_o, is also correspondingly bigger. The optimum size of aperture for tilt correction ($D \approx 4r_o$) is also increased, thus enabling fewer sub-apertures to be used in covering the full aperture of a large telescope. For example, in typical seeing conditions ($r_o =$ 10 cm) a 4 m telescope such as the WHT would require approximately 170 sub-apertures at a wavelength of 0.5 μm, whilst at 5 μm this reduces to only about 7. At infra-red wavelengths the correlation time of wavefront distortion is increased and this coupled with the fact that the number of photons available increases approximately with $\lambda^{\frac{17}{5}}$ (due to the increase in optimum aperture size and decrease in individual photon energy), enables a less bright star to be used as the reference object. RODDIER AND RODDIER [10] have also shown that the deterioration in image quality due to wavefront amplitude fluctuations becomes less of an effect with increasing wavelength. All these advantages have to be weighed against the disadvantage of the increase in the diffraction limited image size at longer wavelengths; the full width half maximum of the image increasing in proportion to the wavelength. Table 3.1 summarises the change in value of the basic parameters of seeing as the wavelength is increased.

Wavelength (microns)	r_o (cm)	Isoplanatic patch (arcsec)	Correlation Time (millisec)	Diffraction Limit 4m Aperture (arcsec)
0.5	10	6	10	0.031
2.2	60	36	60	0.136
5.0	160	70	160	0.309
10.0	360	150	350	0.618

Table 3.1: Change of Seeing Parameters With Wavelength

The major drawback to adaptive optics image correction in the infra-red is the current lack of suitable photon counting detectors at these wavelengths, though progress in this field has greatly advanced in recent years. To overcome this problem, various groups have adopted an approach where wavefront distortions are sensed at optical wavelengths, whilst the final stabilised image is recorded in the infra-red. This is termed the 'polychromatic approach' and though chromatic errors are introduced due to the difference between the sensing and recording wavelengths, the expected deterioration in the final corrected image due to these errors can be shown to be small. If it is assumed that total phase correction has taken place the OTF of the atmosphere is given by the contributions due to amplitude effects alone and RODDIER AND RODDIER [10] give such an atmospheric optical transfer function for a two wavelength correction system as

$$\mathrm{OTF}(\rho) = \exp(-0.14 r_o^{-\frac{5}{3}} (\cos\theta)^{-\frac{11}{6}} \lambda_2^{\frac{5}{6}} \overline{h}_p^{\frac{5}{6}} I_2(|\rho|\sqrt{\cos\theta/\lambda\overline{h}}, q), \qquad (3.9)$$

with,

$$I_2(\alpha, q) = \int_0^\infty \xi^{-\frac{8}{3}} q^2 [1 - \mathrm{J_o}(2\pi\alpha\xi)][\cos(\pi q \xi^2) - \cos(\pi\xi^2]^2 [\sin(\pi\xi^2)]^2 d\xi, \qquad (3.10)$$

where q is the ratio of the wavelength λ_1 at which the wavefront distortions are sensed to the wavelength λ_2 at which the final corrected images are recorded, and $\overline{h}_p$ is an average height given by

$$\overline{h}_p = \left[\frac{\int_0^\infty h^{\frac{5}{6}} C_N^2(h) \mathrm{d}h}{\int_0^\infty C_N^2(h) \mathrm{d}h} \right]^{\frac{6}{5}}, \qquad (3.11)$$

Figures 3.2 and 3.3 show the atmospheric optical transfer function expected after

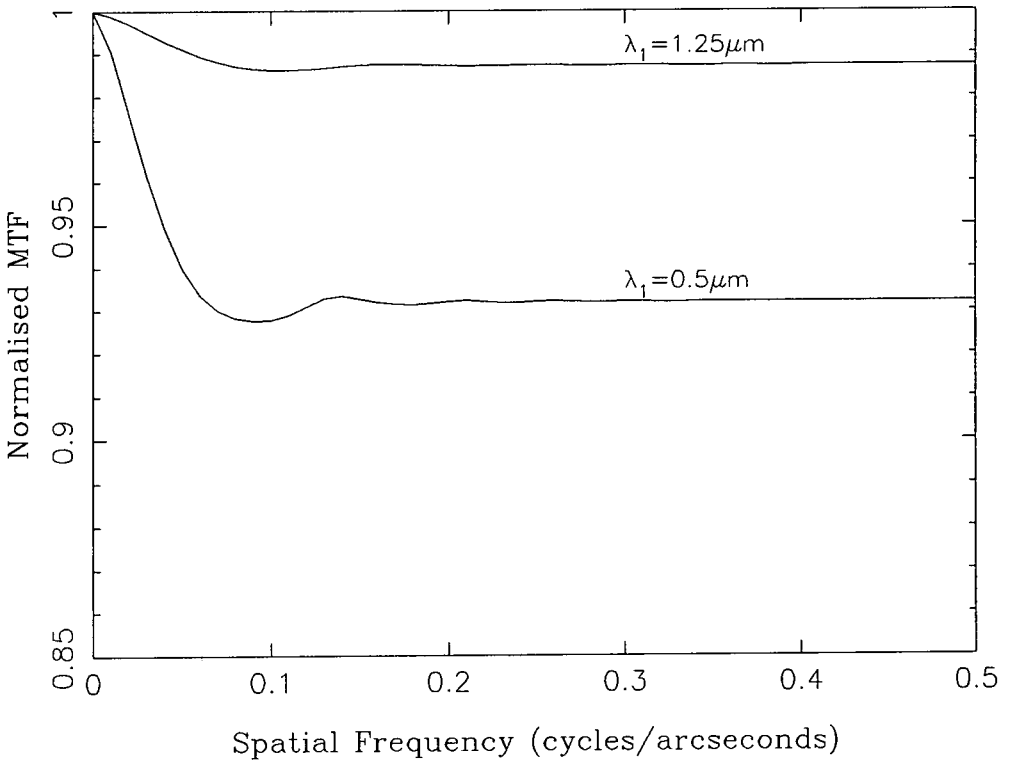

Figure 3.2: Atmospheric optical transfer functions after phase correction for a λ_2 of 2.2 μm and λ_1 values of 2.2 μm and 0.5 μm (after Roddier and Roddier [10]).

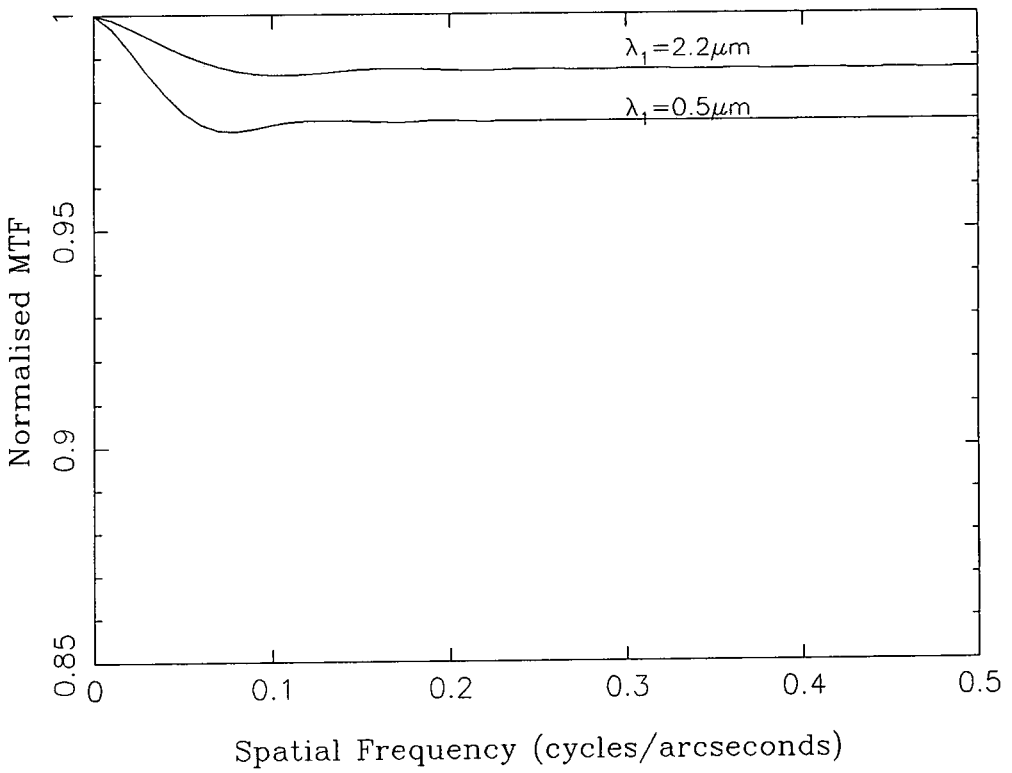

Figure 3.3: Atmospheric optical transfer functions after phase correction for a λ_2 of 1.25μm and λ_1 values of 1.25μm and 0.5μm (after Roddier and Roddier [10]).

total phase correction for λ_2 values of 1.25 μm and 2.2 μm, for various λ_1 wavelengths at which the wavefront distortions are sensed. The calculations are based on an assumption that $\overline{h}_p$ is 4 km and that r_o at a wavelength of 500 nm is 10 cm. It can be seen from these figures that the deterioration in the corrected atmospheric optical transfer function due to sensing at visible wavelengths is between 5–10 percent.

3.3 Review Of Current Adaptive Optics Systems

The first experiments on image sharpening using adaptive optics were conducted by BABCOCK [52] during the 1950's. Using a single plane mirror to remove wavefront tilts, Babcock obtained the highest resolution ground based photographs of the planets then available. This work was extended to stellar objects by BUFFINGTON ET AL [53], who constructed a small image sharpening telescope, and was able to achieved sharpened images of several stars. In more recent years the number of groups involved in adaptive optics has rapidly grown and given in table 3.2 are the current projects in service or underdevelopment that utilise adaptive optics for astronomical image sharpening.

3.3.1 University of Hawai

The Image Stabilisation Instrument System (ISIS) has been in operation on the 2.24 m University of Hawaii telescope since 1984 and has successfully produced some image sharpening. The design and operational characteristics of the instrument have been described in some detail by THOMPSON AND RYERSON [54]. Figure 3.4 shows a schematic representation of the optical arrangement of the instrument. Light, converging to the cassegrain focus of the telescope, is incident on an active mirror assembly which reflects the light onto either a dichroic beamsplitter or a circular mirror. The reflected part of the light from the beamsplitter or mirror passes to an output detector, whilst the transmitted part is imaged onto a wide field camera. Behind the beamsplitter a guide probe is positioned at the focal plane of the telescope, and this probe can be moved to acquire a star at any point in the field. The detector head of this guide probe consists of five optical fibres,

Institution (Main Contributor)	Correction Technique	Proposed Use	Status
University of Hawai (Thompson)	Aperture Tilt	Visible Stellar	Operational since 1984
DAO,Montreal (Racine)	Aperture Tilt	Visible Stellar	First observing run March 1989
ESO (Maaswinkel)	Aperture Tilt	IR Stellar	First observing run December 1987
ESO,ONERA,Meudon (Merkle)	Hartmann-Shack	IR Stellar	First observing run October 1989
NOAO,KPNO (Beckers/Goad)	Hartmann-Shack	IR Stellar	First observing run June 1989
NOAO (Roddier/Forbes)	Wavefront Curvature	Visible Stellar	Underdevelopment
NOAO,NAO (Dunn)	Hartmann-Shack	Visible Solar	Underdevelopment
NOAO,PARL (Smithson/Title)	Hartmann-Shack	Visible Solar	Operational since 1986

Table 3.2: Current Adaptive Optics Programmes

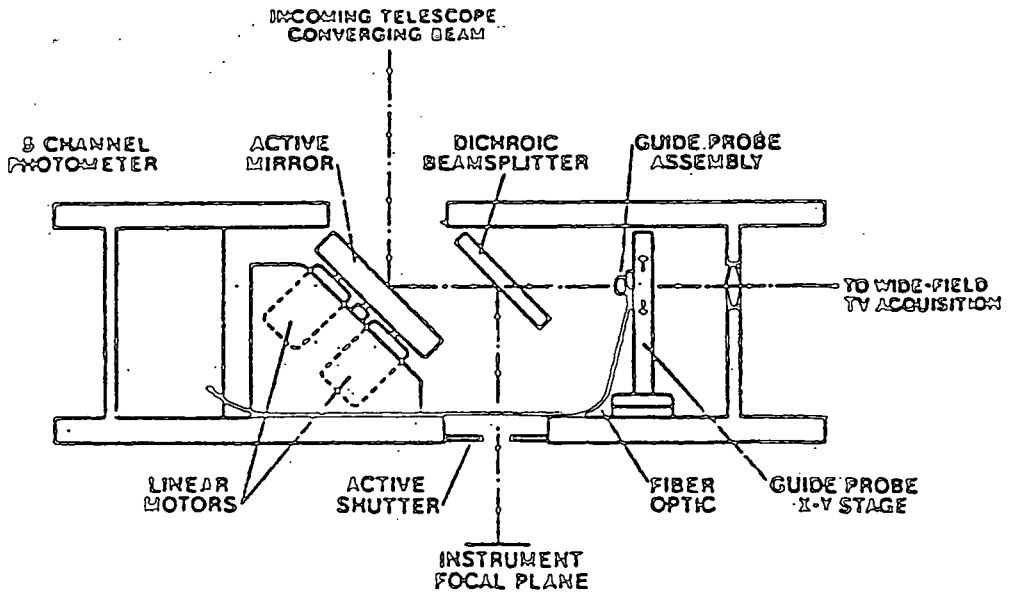

Figure 3.4: Schematic representation of the optical layout of the ISIS image sharpening instrument (from Thompson and Ryerson [54]).

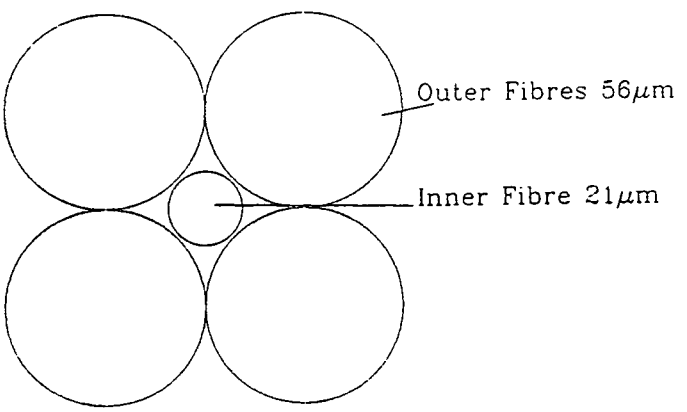

Figure 3.5: Guide probe detector head assembly (from Thompson and Ryerson [54]).

the configuration of which is shown in figure 3.5. The central fibre has a diameter of 21 μm (0.19 arcsec), the outer ones a diameter of 56 μm (0.51 arcsec), and the output end of each fibre is attached to a photomultiplier tube. The position of the reference star is therefore determined by the relative strengths of the signals from each photomultiplier and this information is used to control the tilt correction mirror. The lucky exposure technique can also be utilised in this system by means of a fast shutter system which enables moments of bad seeing to be excluded from the final image.

ISIS has been quite extensively used to obtain sharpened images of astronomical objects (THOMPSON AND VALDES [55]). Thompson typically reports the sharpened FWHM of stellar images obtained, using the full 2.2 m aperture of the telescope, as $\sim$0.60 arcseconds.

3.3.2 DAO, Montreal

A collaboration between the Dominican Astronomical Observatory (DAO) and the University of Montreal, the High Resolution Imaging Camera (HRICAM) has been designed for operation on the 3.4 m Canada-France-Hawaii telescope. The design of the instrument has been described by MCCLURE ET AL. [56] and the optical arrangement of the device is essentially the same as ISIS. The design of the detector head arrangement, however, is slightly different with the light beam from the guide star being incident on the apex of a pyramidal prism which splits the beam into four separate parts, each of which is directed on to a photomultiplier tube. The stabilised output of the whole instrument is recorded with a CCD camera, the image scale of which is 0.1 arcseconds per pixel.

The HRIC underwent its first test on the telescope in June 1989 and it is now in regular use. RACINE [57] reports that through a reduced aperture of 1.2 m, an image FWHM of 0.36 arcseconds was obtainable. An improved version of this instrument is now under development.

3.3.3 Developments At ESO

The European Southern Observatory (ESO) is currently supporting two main adaptive optics developments in collaboration with other organisations.

1) The Direct Image Stabilisation Camera Option (DISCO) is a joint venture of ESO, and the University of Padova. This system has been developed for implementation on the 2.2 m telescope at the La Silla observatory and a description of the instrument is given in MAASWINKEL ET AL. [58]. A schematic summary of the optical layout of the instrument is shown in figure 3.7. An active mirror unit can be positioned anywhere within the main beam of light before the cassegrain focus of the telescope. From this mirror the light is passed on to a dichroic beamsplitter and the transmitted blue part of the light is imaged on to an intensified CCD camera. A subframe of 16×16 or 8×8 pixels can then be selected around the image of a bright guide star in the field and a readout of these pixels is made every 20 ms. The centroid of the star image is then calculated by a 68010 microprocessor and this information used to control the active mirror unit so as to remove the wavefront tilts.

The DISCO system had its first observing run on the 2.2 m telescope in March 1988, the results of which are reported in MAASWINKEL ET AL. [59]. The full aperture of the telescope was used and a stabilised FWHM of 0.66 arcseconds was achieved.

2) The COME-ON project is a collaboration between ESO, ONERA (Office National d'Etudes et de Rescherches Aérospatialles), and the University of Meudon and is part of the development programme for ESO's planned Very Large Telescope Array. The current device is at present built for operation on the 3.6 m telescope at La Silla and the design and principle of operation is described in KERN ET AL. [60]. The optical arrangement of the system is shown schematically in figure 3.8. The system uses a two stage process for wavefront correction; the overall tilt of the wavefront is removed by a single active plane mirror, whilst the phase corrugations along the wavefront are corrected by a thin flexible mirror. The surface deformation of the latter is controlled by 19 piezo-electric actuators attached to the mirror's back. The 'polychromatic' approach is used in this instrument with the wavefront distortion being sensed at optical wavelengths whilst the final corrected

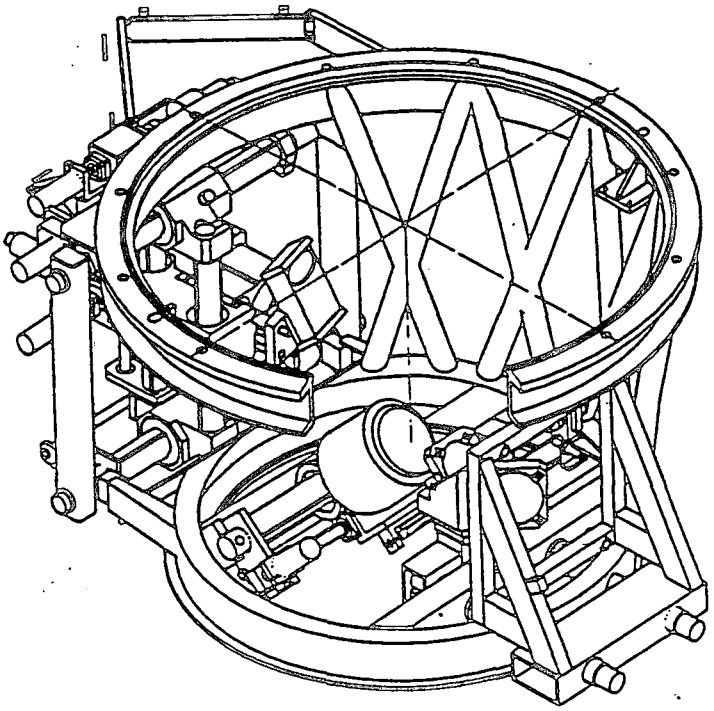

Figure 3.6: 3-dimensional CAD view of the DISCO image sharpening instrument (from Maaswinkel et al. [58]).

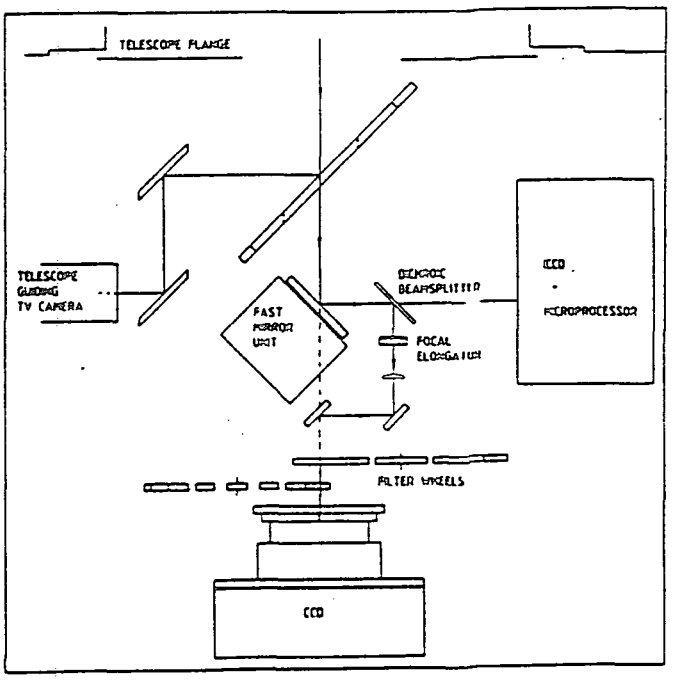

Figure 3.7: Schematic representation of the DISCO optical configuration (from Maaswinkel et al. [58]).

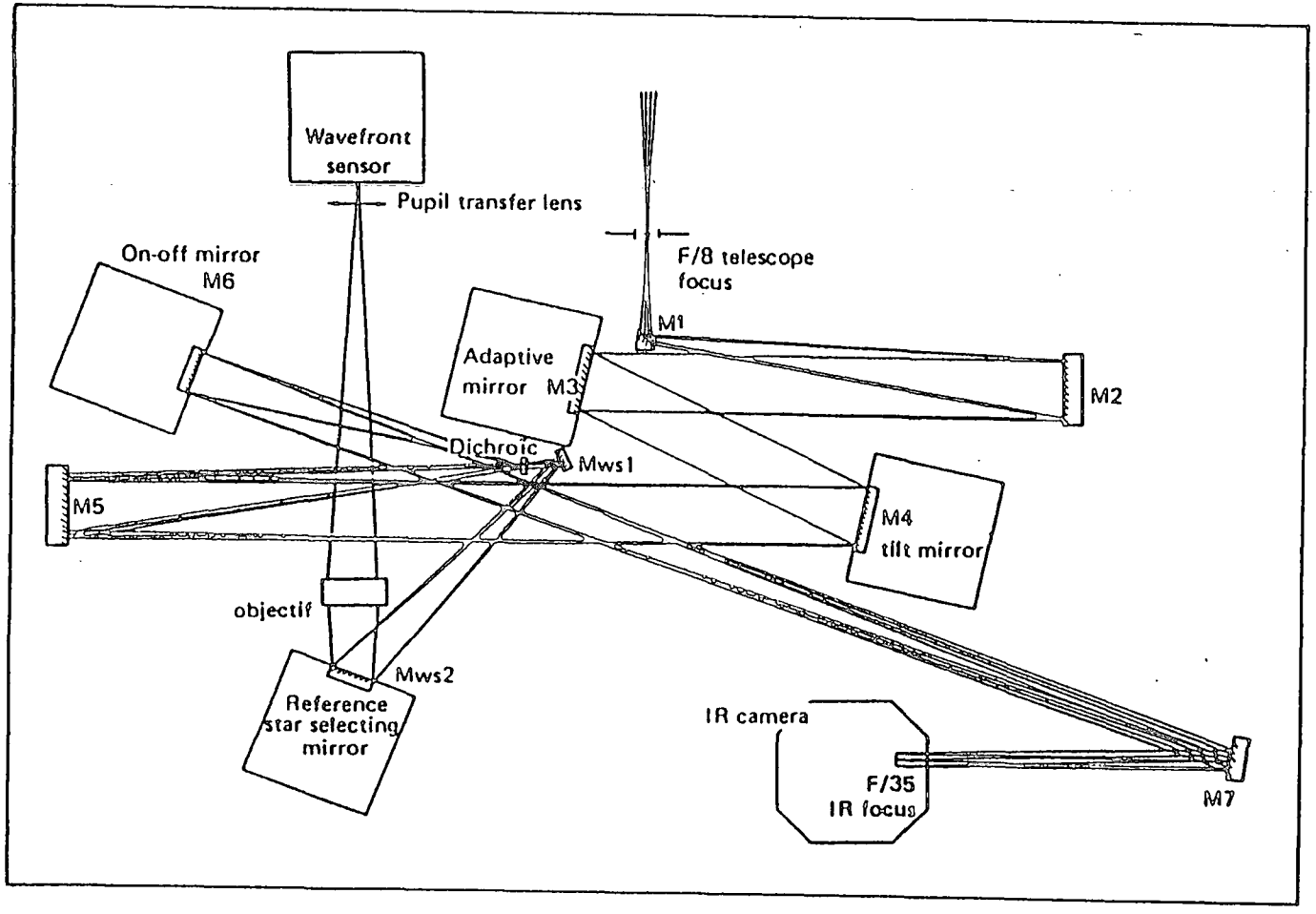

Figure 3.8: Schematic representation of the optical layout of the COME-ON instrument (Kern et al. [60]).

image is recorded in the near infra-red. The light is split by being passed onto a dichroic beamsplitter, the red part of the light being reflected onto the output infra-red camera, whilst the transmitted blue part of the light is focused onto a wavefront sensor. The wavefront sensor used is a Hartmann-Shack arrangement and the image spot pattern it produces is recorded by a proximity focused image intensifier linked to a Reticon detector.

Testing of the instrument has taken place in October 1989 on the 1.52 m telescope at the Observatoire de Haute-Provence and at the 3.6 m telescope at La Silla in February 1990. Reports (MERKLE ET AL. [61], [62]) record that diffraction limited images were obtained at a wavelength of 2.2 μm and partial correction at 1.2 μm.

3.3.4 Developments at NOAO

NOAO (National Optical Astronomy Observatories) is currently involved in four separate adaptive image sharpening projects. Two of these concentrate on stellar image sharpening whilst the remaining two are designed for solar observations.

1) The Beckers/Forbes development program is designed for stellar image sharpening applications and the design of this device is very similar to the COME-ON project. Full wavefront correction is performed using a Hartman-Shack sensing arrangement and a piezo-actuator driven flexible mirror. The system also utilises the 'polychromatic' approach with the wavefront distortions being detected at wavelengths of 0.6–0.8 μm and the corrected images being recorded at 2.2 μm. A full description of the instrument is given in GOAD ET AL. [63].

2) The Roddier/Forbes adaptive optics system is a relatively innovative one in that the curvature of the distorted wavefront is sensed by comparing the intensity distributions across the wavefront at two positions on either side of the focal plane, the technique is more completely described in RODDIER [64]. The wavefront is then corrected using a bimorph piezo-electric wafer.

3) The Smithson/Title programme is a collaboration between NOAO and the Lockheed Palo Alto Research Laboratories. The system is designed for solar studies at the Sacramento Peak observatory. Image correction is achieved using a 19

element hexagonally segmented mirror, each element being controlled by three piezo-actuators. Wavefront distortion sensing is performed using a Hartmann-Shack detector, the position of the images produced by each element of the lenslet array being sensed using a four element detector (quad cell) approach similar to that used in the DAO's high resolution imaging camera.

In guiding on solar images a problem is posed in that there are few objects that stand out on the solar surface that can be used as reference objects to determine the wavefront distortions. Certain objects, however, such as sunspots can be used and in moments of very good seeing Smithson has reported that the instrument was able to lock onto solar granulation.

4) The Dunn programme is again a system designed for solar studies, a description of the device is given in DUNN [65]. The instrument is designed for operation at the Vacuum Tower Telescope (VTT) at the Sac Peak observatory. A 96 element triangularly segmented mirror is used to correct the wavefront distortion. Each segment is controlled by three piezo-actuators, with an additional piezo-actuator connecting the vertices of six adjacent segments. The wavefront sensing in this device is performed with a Hartmann-Shack arrangement where the image from each lenslet is imaged on to a 32×32 pixel Reticon detector. In order to overcome the limitations imposed using a low contrast reference object, the instrument plans to incorporate a correlation tracking technique (see O. VON DER LÜHE [66]), where a reference frame is generated and then subsequent short exposure images cross-correlated with it to find their relative shifts. Due to the evolution of solar granulation the reference frame has to be updated every few minutes.

Chapter 4

Technical Description Of MARTINI

4.1 Introduction

The MARTINI image sharpening device, designed and built in Durham, is based upon removing in real-time the seeing induced tilt of a wavefront from an astronomical object. In principle a possible factor of three improvement in the FWHM of corrected images over that of uncorrected images can be attained, if the size of the aperture used for the observations is optimised to the prevalent seeing conditions ($D \approx 4r_o$).

The design of the MARTINI system is similar in concept to the ISIS instrument of Thompson and Ryerson described in the previous chapter, with the removal wavefront tilts achieved by the action of a rapidly guided plane mirror. However MARTINI differs from this device in two significant design features. The first difference in design being that, instead of a single aperture, a multiplicity of apertures is used each with its own tilt correction system. The sharpened images formed by each of these apertures are combined to form the final output of the system. This allows fuller coverage of the primary mirror to be achieved when using seeing matched apertures, thus increasing the light throughput of the device. The second major way it differs in design from the ISIS instrument is that in the MARTINI system the plane of tilt correction is situated 60 cm downstream from the primary Nasmyth focus of the WHT. This positioning of the correction plane means that it is at the conjugate focus to a height above the telescope of 3.6 km and such an

arrangement can be seen from table 2.3 of chapter 2, to produce a reduced average turbulent layer height and thus increase the expected size of the isoplanatic patch.

4.2 Optical Layout

Light from a selected astronomical field, which includes a bright guide star, enters the MARTINI system through a hole in the centre of a toroidal mirror placed at the Nasmyth focal plane (A) of the WHT (see figure 4.1). The divergent beam of light from the focus is then incident on an aperture mask positioned 60 cm downstream from the focal plane. This aperture mask consists of a set of six identical circular sub-apertures, the size of which can be varied to match the atmospheric seeing conditions prevalent at the time of observation. Immediately behind each sub-aperture is a piezo-actuator driven wavefront tilt compensating mirror, which reflects the light from the sub-apertures back on to the toroidal mirror. The toroidal mirror then refocuses the light to a point 60 cm behind the aperture mask assembly and 14 cm off-axis (B). The total magnification of the system is designed to be 1:1, so that the image scale at this re-imaged secondary focus is the same as at the true Nasmyth focus (i.e. 4.46 arcsec mm^{-1}).

The light at the secondary focus is split into two separate parts by a beam splitter. The reflected part is diverted off and the light from the guide star is imaged onto the photocathode of an Image Photon Detector (IPD) via a 'split lens' and a neutral density filter slide system. The function of the split lens is to magnify and separate on the IPD cathode the images of the guide star formed through each individual sub-aperture. The positions of these images, as recorded by the detector, are then used in a servo system to control the tilt compensating mirrors in such a way as to remove the images' seeing motions. Thus when MARTINI is operating the light that is transmitted through the beam splitter at the re-imaged Nasmyth focus constitutes the final real-time corrected output of the system. This light can be fed into an instrument of the observer's choice such as a CCD camera or a spectrograph.

The MARTINI system also includes an artificial star unit which is used for guide star aquisition and alignment purposes. This system is positioned in front

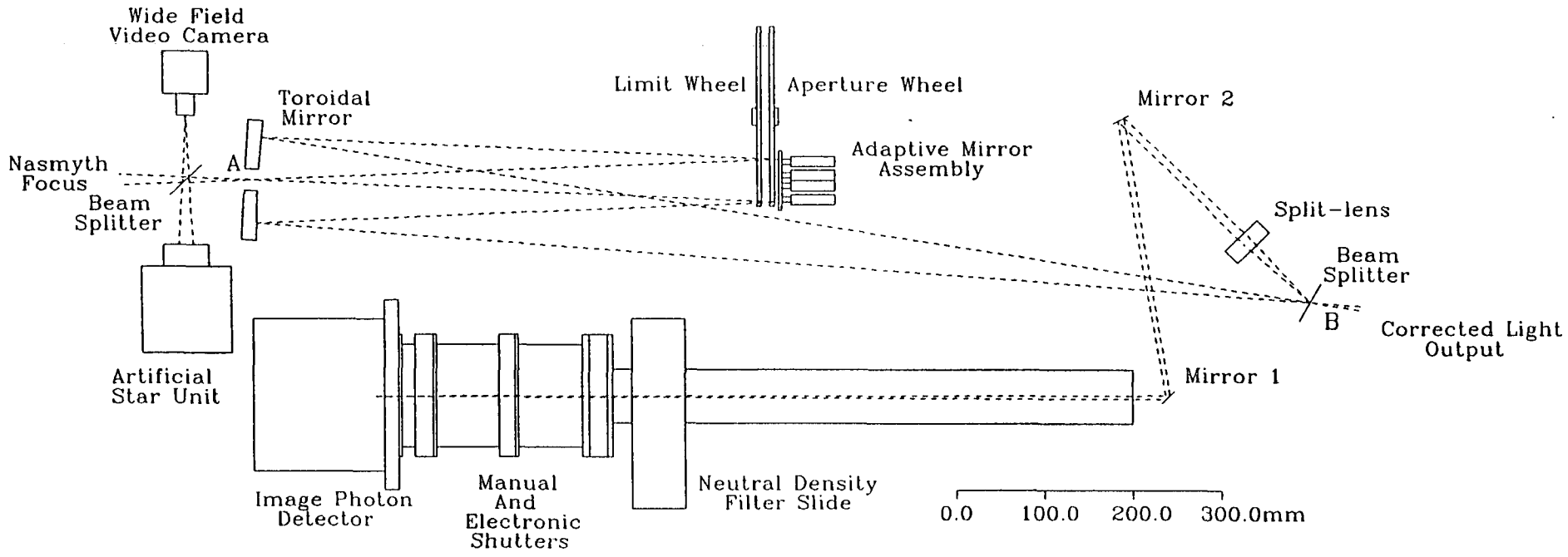

Figure 4.1: Optical layout of the MARTINI image sharpening instrument

of the toroid mirror and the light from it is introduced into the Nasmyth focus via a removable beam-splitter.

4.3 Toroidal Mirror

The design of the optical arrangement is such that the re-imaging toroidal mirror is required to produce diffraction limited images at an off-axis focal position. This mirror was manufactured by mechanically stressing a concave spherically surfaced optical blank into the required asymmetric shape. The stressing moments were applied by a set of 24 leaf springs attached to the edge of the mirror. The blank was then ground and polished back into a spherical shape. When the stressing was subsequently released, the surface of the blank assumed a curvature similar to that when originally stressed, but rotated by 90 degrees.

Interferometric tests on the finished mirror showed that the measured wavefront errors across the surface of the mirror were less than one fifth of a wavelength out to a radius of approximately 65 mm (see figure 4.2). The point of minimum astigmatism was found to be produced at an image-object separation of 140($\pm$2)mm; for object-image separations away from this optimum the images formed show a small amount of spherical aberration, the exact amount depending on the size of the sub-aperture used.

4.4 Aperture And Limit Wheel Assembly

The aperture wheel assembly, shown in figure 4.3, consists of a rotatable thin brass plate in which there are a series of sub-aperture masks. The sub-apertures in each mask are positioned in a circular pattern of 3.65 cm diameter and 1.825 cm centre to centre spacing. The positioning of the aperture masks can be performed remotely under computer control. The available sub-aperture sizes along with their equivalent aperture when imaged back through the telescope optical system on to the 4.2 m primary are given in table 4.1.

The individual apertures or combinations of apertures in each sub-aperture

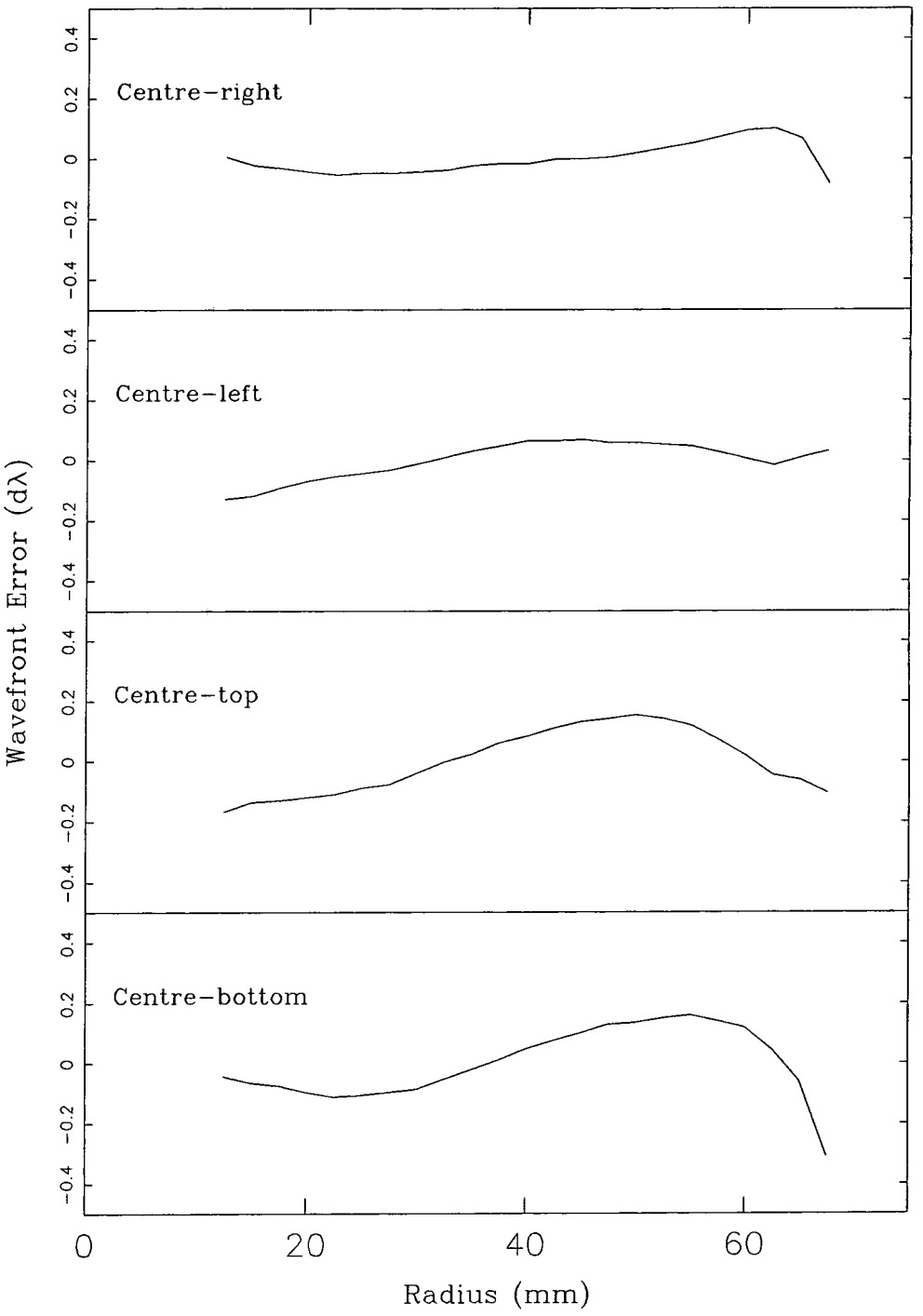

Figure 4.2: Toroid mirror wavefront errors versus radial distance from the toroid's central hole measured at a wavelength of 546.1 nm.

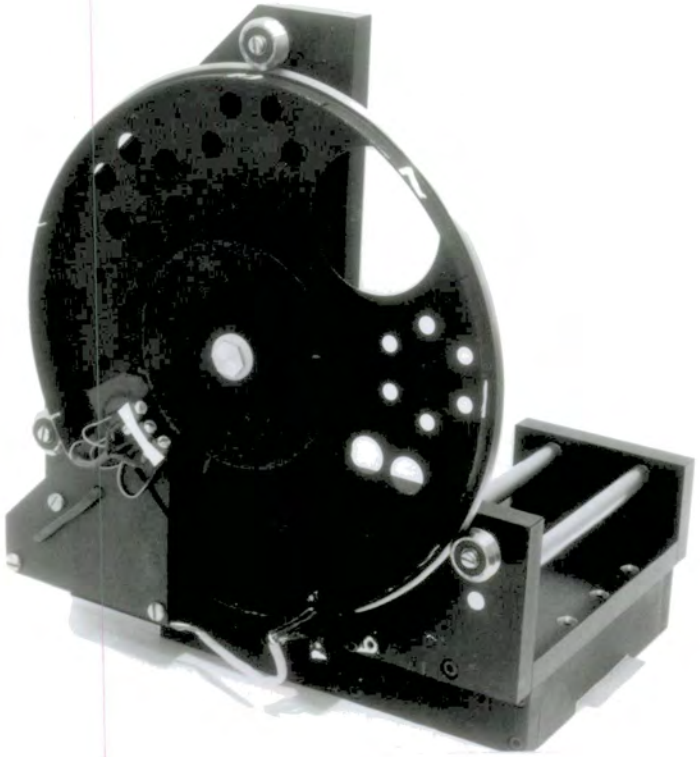

Figure 4.3: Aperture wheel assembly.

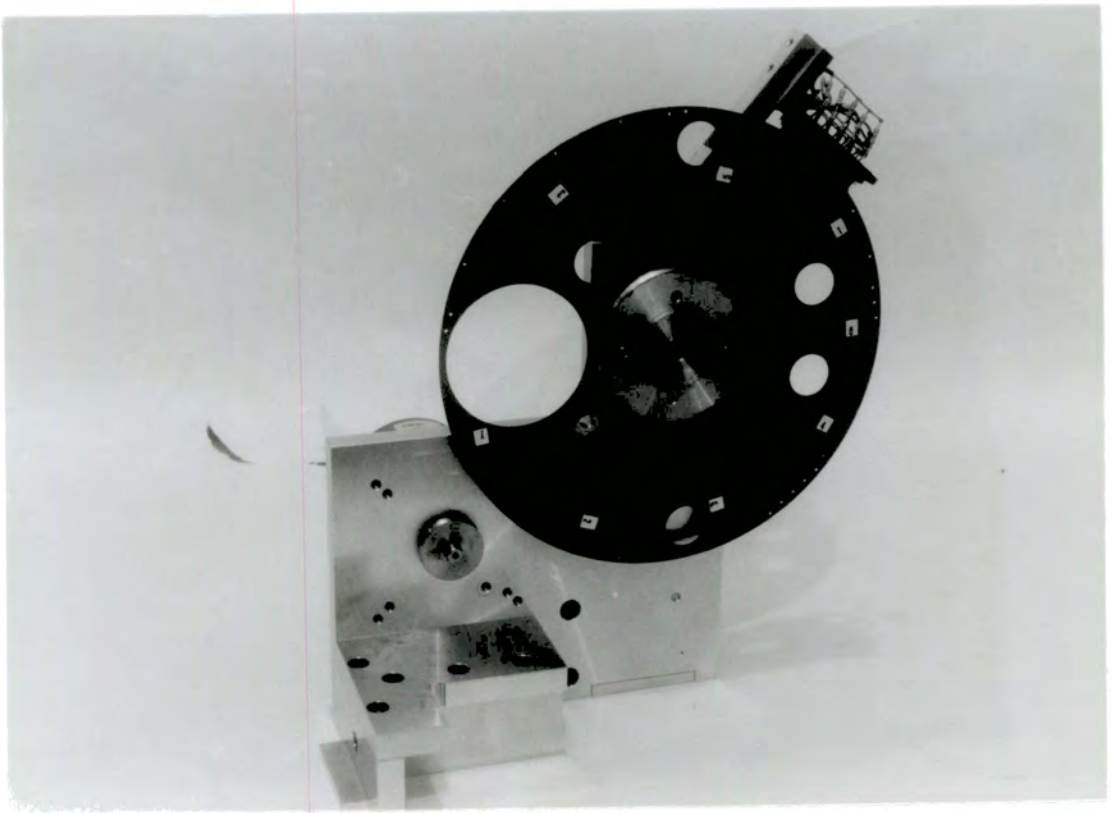

Figure 4.4: Limit wheel assembly.

mask can be selected using the limit wheel, shown in figure 4.4, which can also be controlled remotely. Further combinations of the sub-apertures can be arranged using manually inserted masks.

Aperture No	Diameter (mm)	Equivalent Aperture (cm)
0	5.45	41.96
1	6.21	47.82
2	7.58	58.37
3	9.73	74.92
4	11.63	89.55
5	14.36	110.57
6	17.30	133.21
7*	55.35	426.12
* 6 inserts for 27.49cm		

Table 4.1: Selectable sub-aperture sizes and their equivalent diameters on the telescope primary.

4.5 Active Mirror Assembly

This consists of a plane circular mirror, of diameter 74 mm, divided up into six equal pie-shaped segments. To the back of each of the mirror segments are attached three piezo-electric actuators in a triangular pattern (see figure 4.5). These actuators are used to control the mirror segment's position and tilt; a picture of the whole assembly is shown in figure 4.6,

The actuators used were Burleigh PZL-015s. These are purely reactive devices (capacitance $\approx 1\,\mu F$) and consist of a stack of Lead Zirconium Titonate crystals. They provide a travel range of approximately 15 μm with an applied voltage of 0–150 Volts; a typical actuator extension versus voltage plot is shown in figure 4.7. It can be seen from this figure that the PZLs show a considerable hysteresis which is

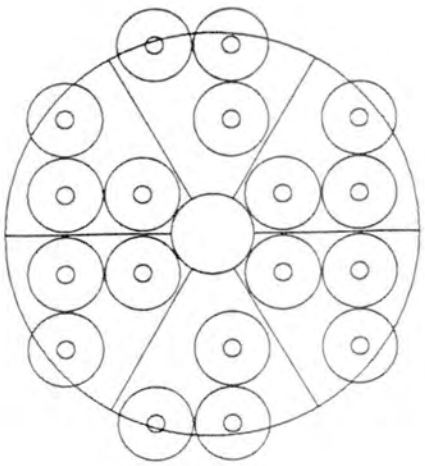

Figure 4.5: Actuator arrangement.

Figure 4.6: Active mirror assembly.

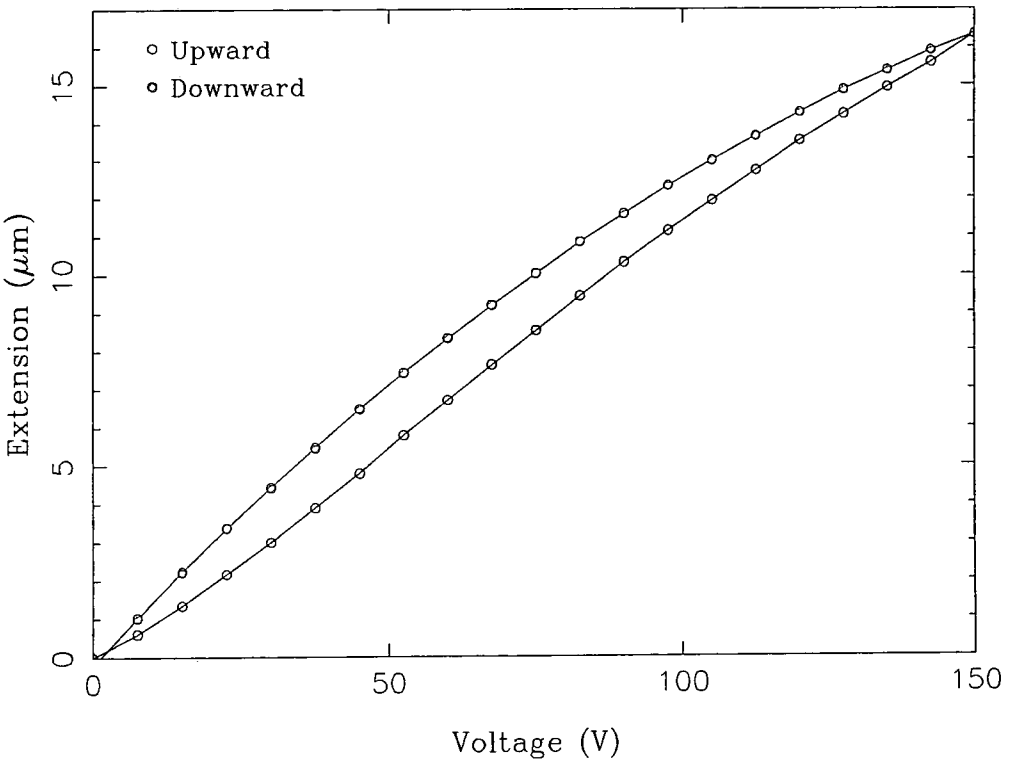

Figure 4.7: Typical PZL-015 actuator extension versus voltage curve.

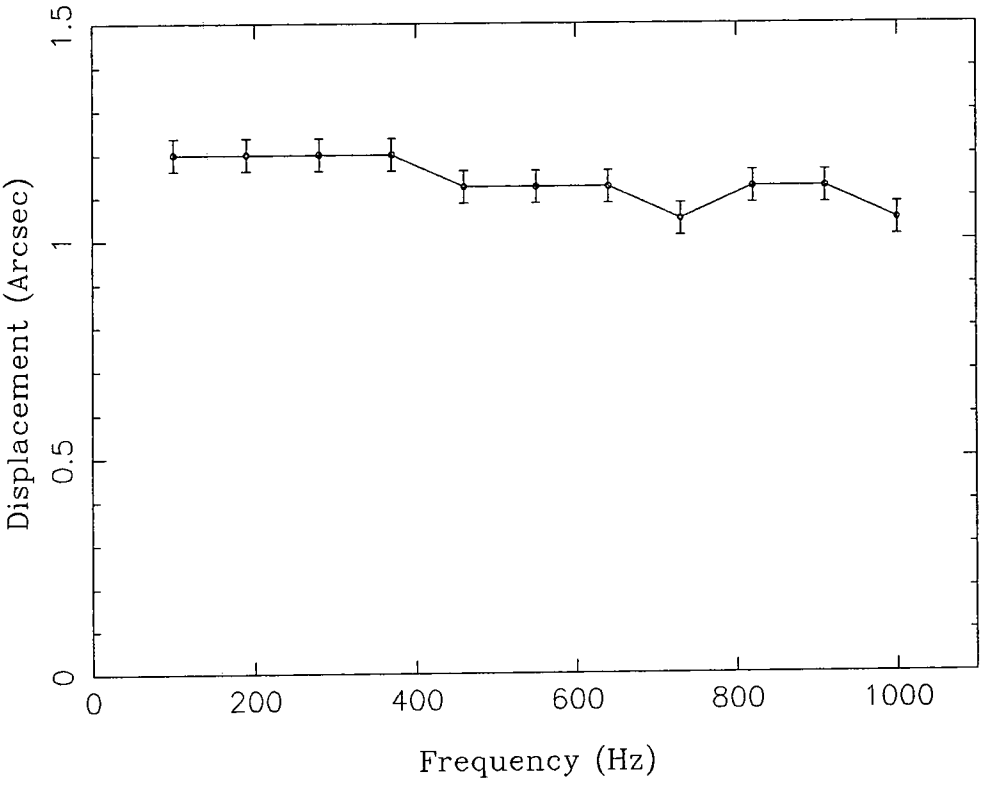

Figure 4.8: Frequency response of tilt mirror segment.

in the order of 10–15 percent of the maximum extension. The 15 μm travel range of these actuators, in conjunction with the lever arm employed, enables each mirror segment to be tilted through an angular extent of ± 3 arcseconds.

Each of the actuators connected to a single tilt mirror segment, is driven by one of the three output channels of a Photon Control MDA-amplifier unit. Six such amplifier units are therefore used in all; one for each mirror segment. The control of these units is provided by the outputs of an eighteen channel digital to analogue converter (DAC) connected to the main real-time control computer of the instrument. The DAC channels provide dc-voltage levels in the range 0–5 Volts, and these voltages are then amplified by a factor of 30 by the MDA amplifier units to produce the necessary 0–150 Volt range required to drive the actuators.

The frequency response of the tilt mirrors was tested by passing a voltage sine wave input into one of the actuators connected to mirror segment and measuring the displacement of a light beam reflected off the mirror's surface (the voltage sine wave amplitude chosen as to produce a ~ 1 arcsecond mirror tilt corresponding to the typical angular range over required during real-time image correction). The results are shown plotted in figure 4.8 and it can be seen that the mirror response is reasonably linear up to the maximum frequency injected, which was close to 1000 Hz. This frequency is well above that of the frequency of mirror tilt operation intended with the MARTINI system which is designed at present to work at frequencies of less than 100 Hz.

4.6 Split Lens Assembly

This consists of a 10 cm focal length achromatic doublet that has been cut into six pie-shaped segments (see figure 4.9), the width of the cuts chosen so that when the segments are reassembled they no longer have a common optical axis and thus the focal points of the segments are separated. To achieve the required guide star image separation on the IPD detector, the width of the cuts was 0.78 mm which, combined with an optical configuration giving a magnification of 13, caused the six guide star images at the IPD photocathode to be equally spaced on a 22.8 mm diameter circle. With such a configuration the image scale at the IPD is 0.33 arcsec mm^{-1},

and therefore the 38 mm extent of the IPD cathode corresponds to a total field size of 13 arcseconds.

A schematic of the optical arrangement of the split lens as used in the MARTINI system is shown in figure 4.10 and it can be seen that the pencils of light from each sub-aperture converge at a point between the lens and IPD detector, thus enabling a field stop to be placed at this position to prevent any extraneous light from reaching the photocathode. Figure 4.10 also shows that the cones of light from each of the sub-apertures pass through the lens segments at off-axis positions, therefore producing a slight distortion in the final images due to chromatic aberration and coma. A ray tracing computer programme was used to predict the magnitude of this effect, in which a point source was simulated 0.78 mm (half the cut width) above the optical axis of a lens and a series of test rays were drawn passing through the lens in such a way as to represent the path that the cone of light from an individual sub-aperture would take. The resulting positions of the test rays at the focal plane for three different wavelengths (486.1nm, 587.5nm, and 656.3nm) are shown in figure 4.11. The overall distortion expected can be seen to be less than 100 microns which, using the image scale given above, corresponds to an image blur of less than 0.03 arcseconds.

4.7 Beam Splitter

A choice of beam splitters, used to divide the light between the IPD and the instrument recording the final corrected output, is available. Standard beam splitters can be used which give 50:50 and 70:30 ratios of reflection and transmission of light. However, these beam splitters use the light inefficiently and instead dichroic beam splitters provide a more efficient use of the light, the blue component of the light being diverted on to the IPD, whilst the red component is sent to the output instrument. This still poses problems in that the final image of the astronomical field contains the image of the bright guide star. What is actually desired is that the light from the guide star alone is totally removed to be imaged on the IPD, whilst light from the rest of the field is transmitted to the output instrument. To achieve this a beam splitter was fabricated that consisted of a 1 mm diameter circular mirror aluminised on to the center of a glass plate. This plate can be placed

Figure 4.9: Split lens system

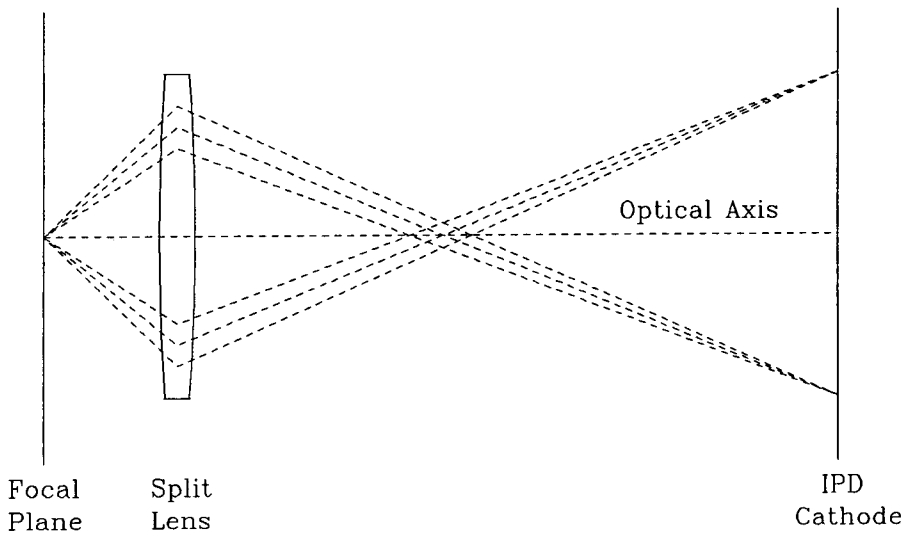

Figure 4.10: Schematic diagram of the Split lens optical configuration

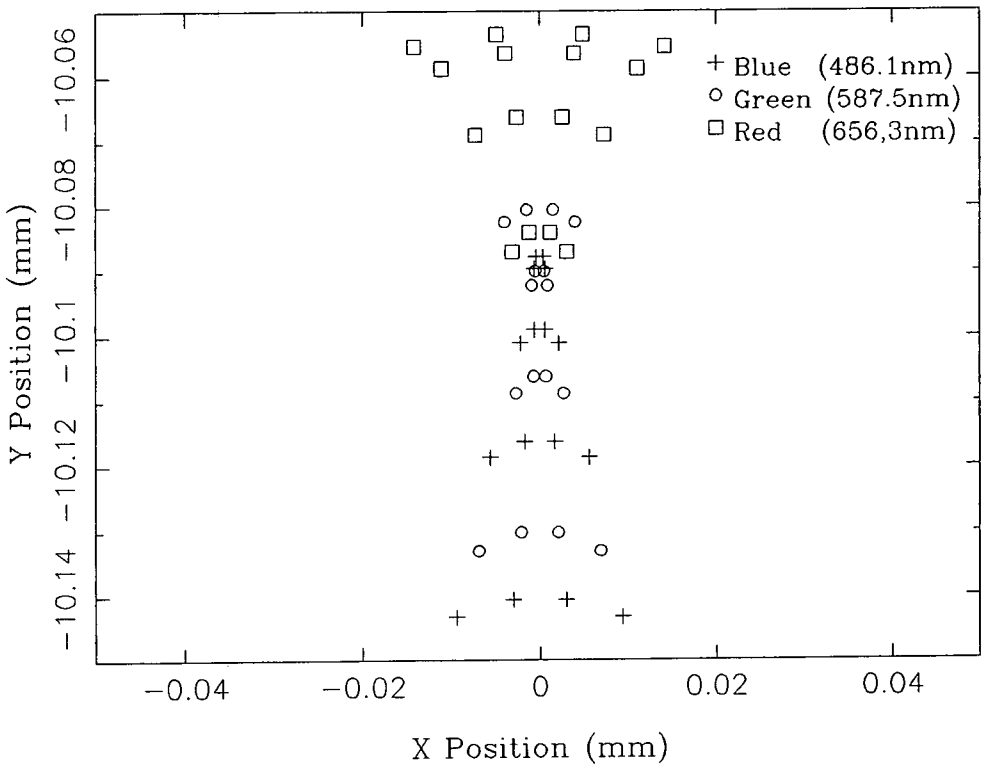

Figure 4.11: Results of the ray tracing programme, shown are the expected distributions for the test rays of wavelength 486.1nm, 587.5nm, and 656.3nm.

at the re-imaged Nasmyth focus in such a way that the circular mirror removes the guide star light alone.

4.8 Artificial Star System

The artificial star system consists of an illuminated pinhole fed with light from a fibre optic cable connected via a 'hot' mirror filter to a tungsten light source; the filter is present to remove the source's infra-red component in order to reduce abberations. The light from the pinhole is then imaged by an achromatic lens and actively controlled plane mirror to a focus at the centre of the MARTINI toroidal mirror, the light being introduced into the main Nasmyth beam via a removable beam splitter. A schematic diagram of the whole system is shown in figure 4.12.

The artificial star image formed at the Nasmyth focus can be driven in both an X and Y direction by the action of the active plane mirror, the tilt of which is controlled by two linear motors attached to its back. These linear motors are themselves controlled by an IBM-AT personal computer. This system can be used to move the artificial star image in such a way as to simulate the motion of a real star, a facility which was found to be particularly useful in testing the image sharpening performance of the MARTINI real-time correction algorithms.

In its fixed mode the artificial star is used in the setting up procedure of the MARTINI system to ensure the correct alignment of the optical elements. Once this has been achieved, the artificial star image can be used as a star acquisition aid as its position on the wide field CCD camera marks the exact point to which the guide star to be used for image correction must be brought in order that star is acquired on the IPD detector.

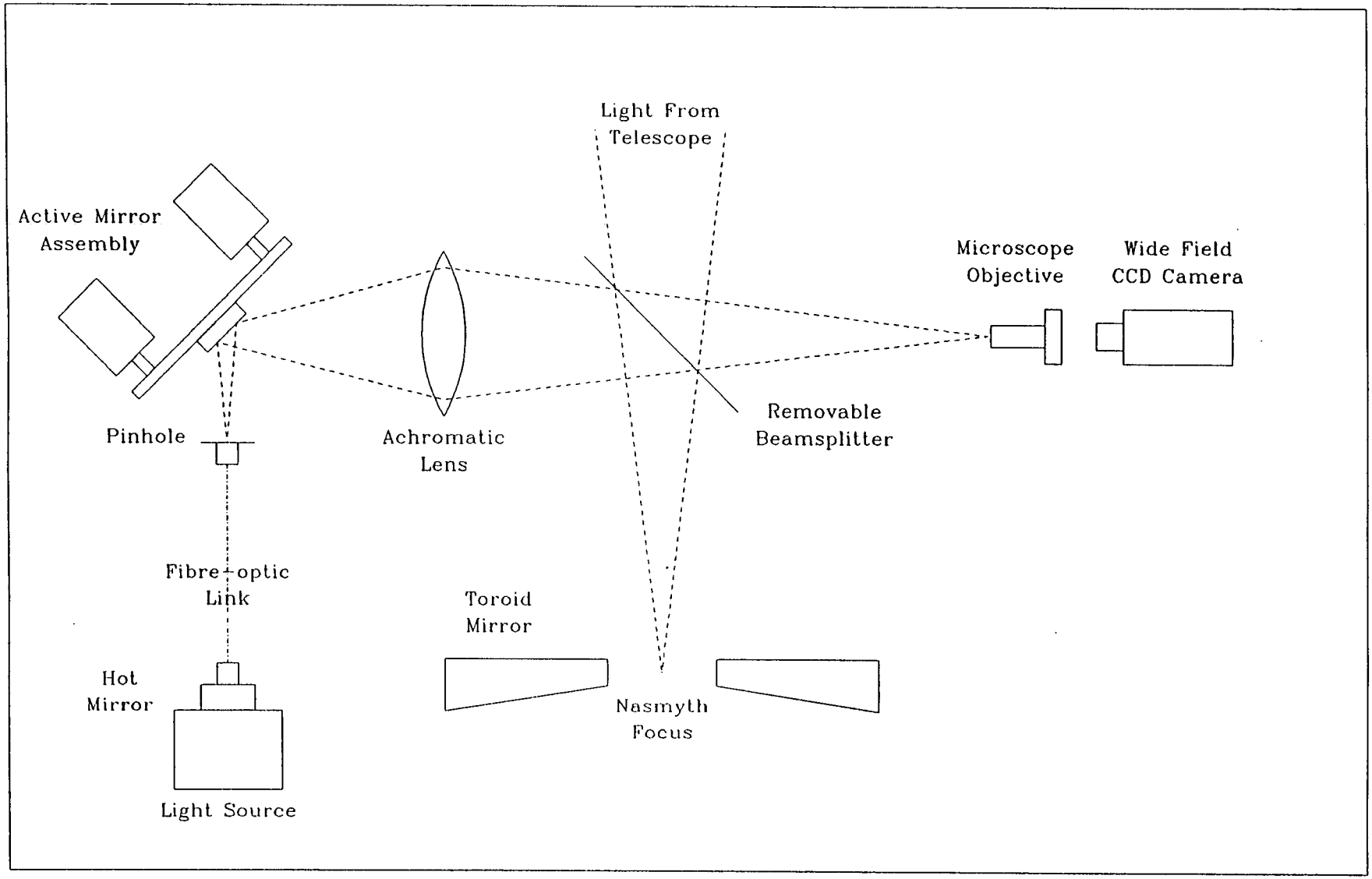

Figure 4.12: Schematic of the artificial star system.

4.9 Image Photon Detector

4.9.1 Design And Principle Of Operation

The Image Photon Detector (IPD) (see REES ET AL. [67]) consists of two units; the detector head and the photon event processing electronics. The design of the IPD head is shown schematically in figure 4.13; it basically consists of a glass vacuum tube containing a photocathode, an array of microchannel plates (MCPs), and a resistive anode. These are all connected to a high voltage supply via a resistor chain as shown in figure 4.14.

The principle of operation of the IPD is as follows. A photon incident on the photocathode of the IPD releases an electron which is accelerated by an electric field on to the first microchannel plate. This field being sufficiently strong to ensure that lateral drift of the electron as it crosses the small photocathode-microchannel plate gap is negligible. The photocathode is therefore said to be proximity focused on to the first MCP. The MCPs now amplify the original electron signal by a factor of $\sim 10^7$, the final plate being driven into saturation thus producing a well defined number of electrons for each photon event. Positive ion feedback, which can deteriorate the performance of the photocathode, is reduced by coating the first plate with a layer of aluminium oxide and by having the channels in the two plates inclined at an angle to each other. The electron cloud that emerges from the last MCP is incident on the resistive anode and the charge pulse produced is detected by pre-amplifiers connected to the anode's four corners.

The particular type of anode used is one of a circularly arc-terminated design, (see LAMPTON AND CARLSON [68]), the edges being bordered by line resistors of values $R_L = r/a$, where r is the resistivity of the anode and a is the radius of the boundary arc (see figure 4.15). Such a design effectively causes the anode to appear as an infinite resistive sheet and the position of any charge pulse incident can be found by a simple relationship between the charges detected at the anode's four corners.

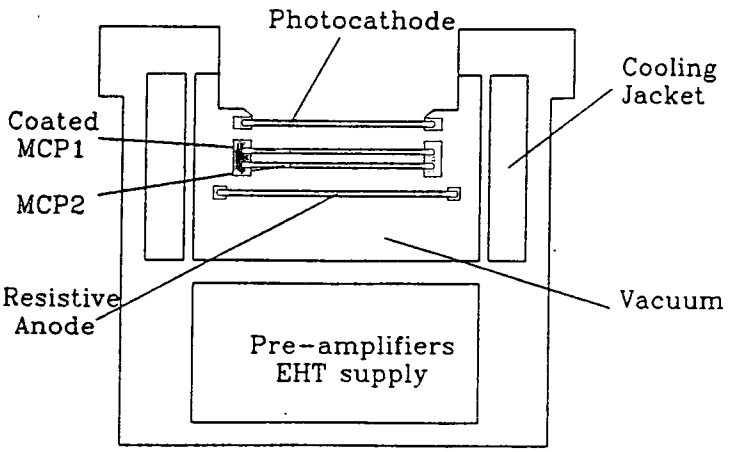

Figure 4.13: Schematic diagram of the design of the IPD detector head.

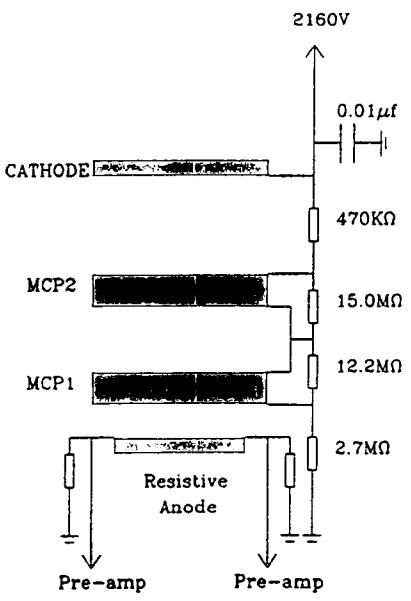

Figure 4.14: High voltage power supply.

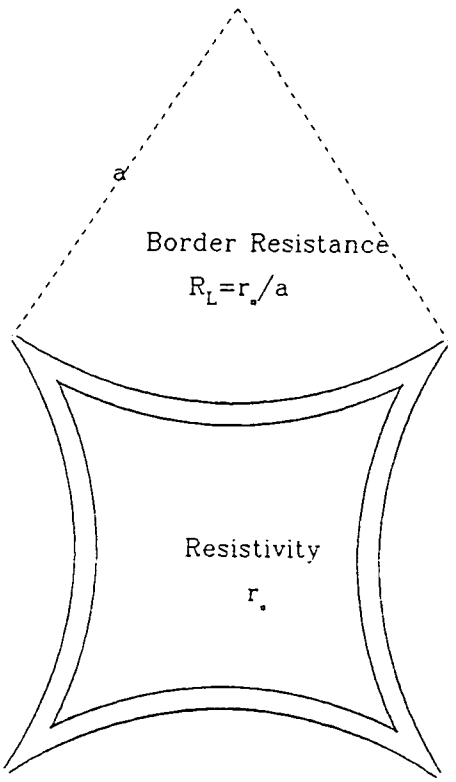

Figure 4.15: Resistive anode design.

4.9.2 Processing Electronics

The basic design of the IPD processing electronics is shown schematically in figure 4.16. When a photon is detected by the IPD head, the electronics converts the four voltage pulses from the anode pre-amplifiers into X,Y coordinates, which are then output in an analogue and a digital form. Each accepted X–Y signal is preceeded by a 1 μs strobe pulse.

The counting system of the IPD electronics is of a paralysed variety; when a photon is detected the system is insensitive to any other photon arrivals for a fixed time interval (the 'dead-time'). The counting efficiency E of such a system is given by BLACKMAN AND MICHIELS [70] as

$$E = \frac{1}{1 + RT}, \tag{4.1}$$

where R is the real detected count rate and T is the system dead-time. To determine this dead-time the processed count was measured for sources of known photon emission rate. Figure 4.17 shows the experimental points along with theoretical curves for dead-times of 4, 6 and 8 μ. It can be seen that a dead-time of 6–8 μs provides the best fit to the observed data. This then puts an maximum upper limit to the photon rate that can be detected of $\sim$130 KHz and even at lower rates can lead to a significant loss of photons. For example at an incident rate of 40 KHz a photon loss of $\sim$ 20 percent is expected. However, this is not a problem in the MARTINI system where the photon count rates used are only between 6–12 Khz. A more serious limitation is the local saturation of the microchannel plates, this arises since each of the microchannels in a plate acts like a capacitor which is discharged when an electron passes through it. Thus the microchannel is 'dead' for a time whilst the lost charge is replaced and this limits the maximum local count rate that can be detected by the IPD to approximately 10 photons per 100 μm^2 per second (manufacturer's specification). To avoid problems with this effect in the MARTINI system, the images of the reference star on the IPD are magnified by a factor of 13 giving an image scale of $\sim$ 0.3 arcsec mm^{-1}, thus spreading the images out over a wide area of the detector.

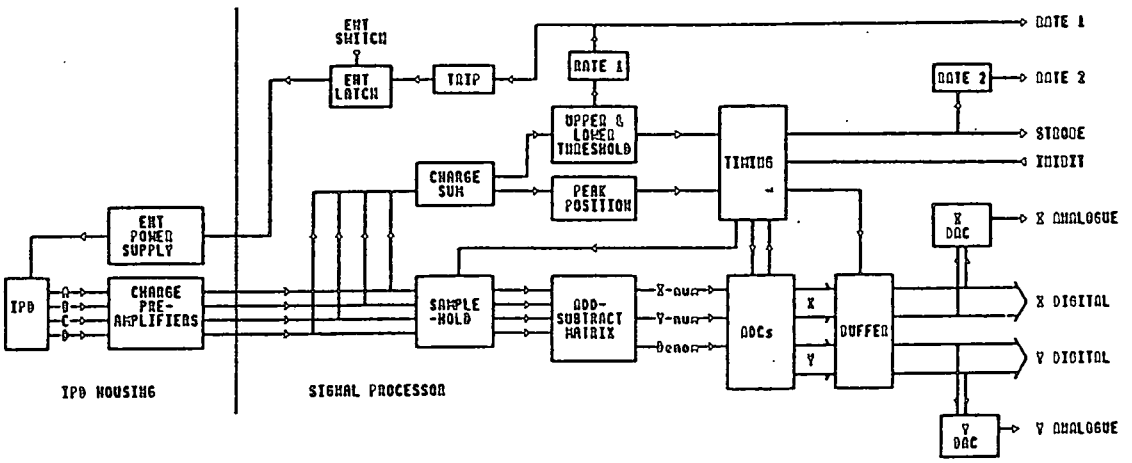

Figure 4.16: Design of the IPD processing electronics (from McWhirter et al. [69]).

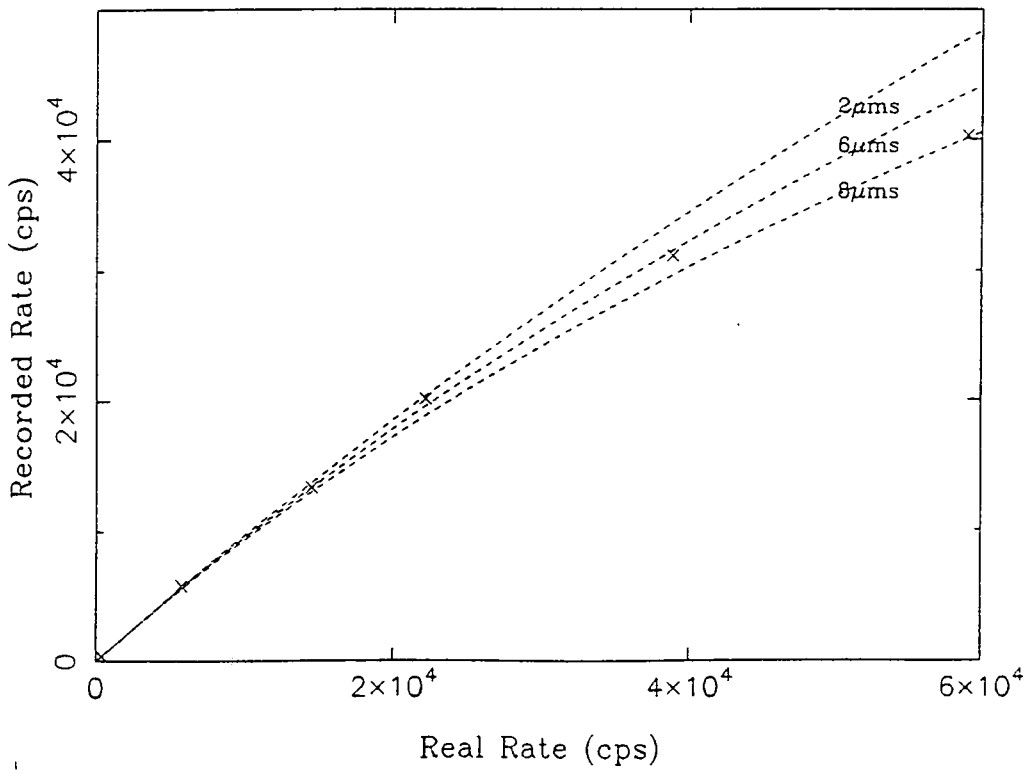

Figure 4.17: Electronically processed photon rate versus real detected photon rate. Also shown (dashed lines) are the theoretical curves for dead-times of 4, 6, and 8 μs.

4.9.3 IPD Efficiency and Resolution

The photocathode provided was of an extended red-sensitive S20 type. The peak relative quantum efficiency of such a photocathode is expected to be about 20 percent. However, using testing facilities at the Royal Greenwich Observatory, the actual peak sensitivity of the IPD cathode was measured as approximately 4 percent, the full relative quantum efficiency (RQE) of the photocathode versus wavelength being shown in figure 4.18. Also shown in this figure is the measured detected quantum efficiency (DQE) versus wavelength for the whole IPD detector system. The difference between the DQE of the whole system and the RQE of the photocathode is mainly caused by loss of electrons emitted by the photocathode at the first microchannel plate due to the plate's open area ratio and anti-positive ion feedback protective layer.

The poor sensitivity of the MARTINI IPD meant that in the first two observating runs with the instrument at the William Hershel Telescope, the faintest guide star that could be used was limited to $\sim 10^{th}$ magnitude. In subsequent runs an IPD with a reconditioned photocathode was used which had a peak DQE of 6 percent as opposed to the original value of 1.5 percent. This improved performance enabled guide stars as faint as 13^{th} to be used.

The efficiency of the IPD's photocathode is not uniform over its surface and figure 4.19 shows the variation as determined by uniformly illuminating the surface of the IPD with a white light source. As can be seen the efficiency is highest in the centre of the cathode with a rapid decline towards the edge.

The size of an individual 10-bit pixel was measured as corresponding $39.86\,\mu m$ in X and $39.03\,\mu m$ in Y. The extent of the photocathode was measured as extending 940 pixels in X ($37.5\,mm$) and 976 pixels in Y ($38.1\,mm$), with its centre at a coordinate position of $506, 520$. The resolution of the IPD was measured by imaging light from small pinholes on to the surface of the photocathode and measuring the the FWHM of the images recorded. It was found that the resolution varied across the IPD surface, but was typically between 160–$300\,\mu m$. Although this resolution is poor in an absolute sense, because of the image scale used in the MARTINI system this resolution corrsponds to an error of only ~ 0.1 arcseconds

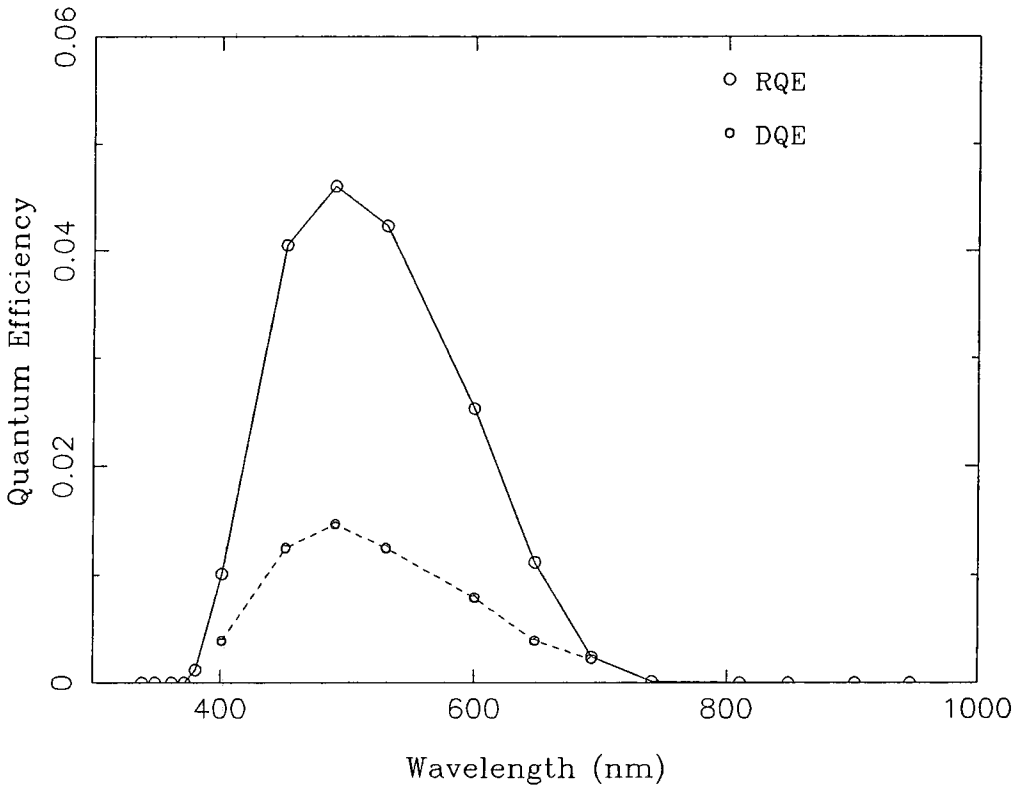

Figure 4.18: Relative quantum efficiency of the IPD photocathode, and total IPD detected quantum efficiency, versus wavelength.

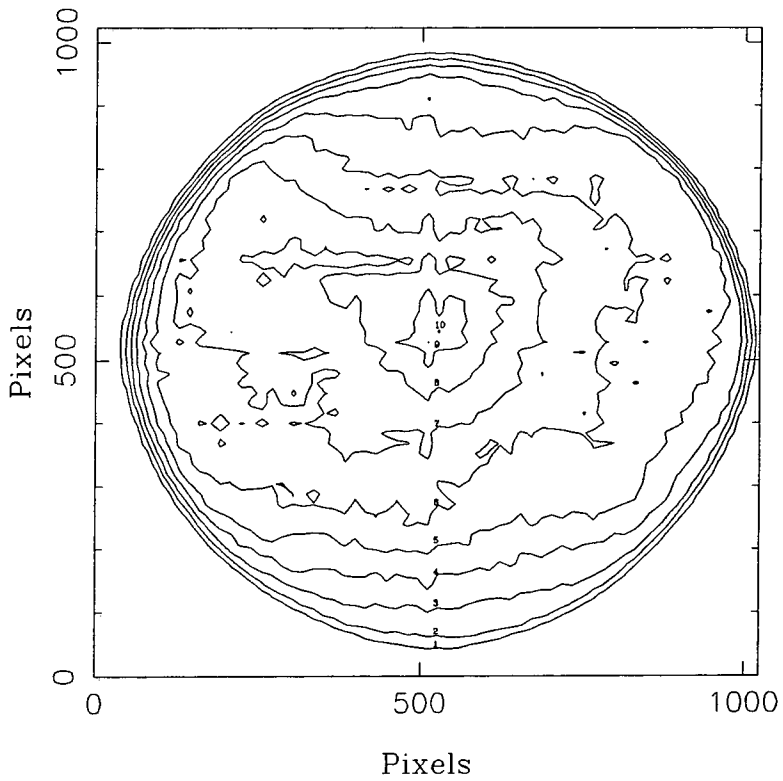

Figure 4.19: Relative efficiency of the IPD photocathode. Contour levels (marked 1-10) give the relative efficiency from 0.1–1.0 in steps of 0.1.

in determining the individual photon coordinates.

4.9.4 Pulse Height Spectrum

Figure 4.20 shows the pulse height distribution of the summed pre-amplifier pulses produced by each photon event as recorded with a multichannel pulse height analyser. The peak in the distribution is due to saturation of the final microchannel plate in the detector head, whilst the peak around channel zero is due to noise effects. To discriminate against the noise, the electronics of the IPD will only accept a photon event if the summed pulse is between a lower and an upper voltage threshold level. Optimally the position of the lower threshold should be in the centre of the trough between the low voltage noise pulse peak and the saturation peak. The setting of the upper threshold is less critical; it should be set above the main distribution to discriminate against large pulses produced by co-incident events. To find the position and efficiency of the threshold levels, the pulse height spectrum of the summed pulses, gated with the strobe pulse, was recorded. Figure 4.21 shows the spectra produced with the summed pulse in coincidence and anti-coincidence with the strobe. The figure clearly shows the positions of the thresholds and it can be seen that the settings were essentially optimised. (The spectrum in figure 4.21 seems shifted to higher voltages compared to that of figure 4.20; this is due to some amplification of the pulses caused by the gating electronics).

4.10 Astronomical Detection Limits

The limiting magnitude of an astronomical object that can be detected using the MARTINI system is strongly dependent on the prevalent seeing conditions since this determines the sub-aperture size that is to be used for the observations. The V band magnitude limits for several different values of the coherence parameter r_o are given in the table 4.2 for exposure times of 1000 and 3000 seconds. The figures for the MARTINI system assume that a seeing matched aperture is used and that full correction to the theoretical short exposure image is attained. The criteria for the detection limit is that a signal to noise ratio of 10 or greater is achieved (see

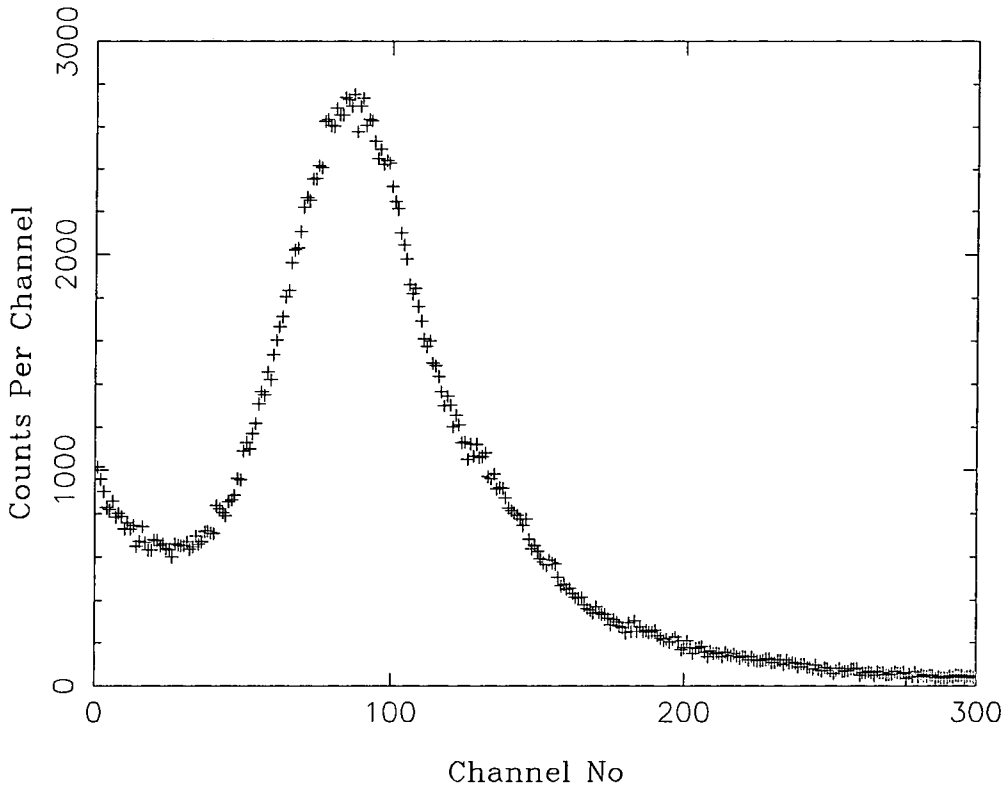

Figure 4.20: Pulse height spectrum of summed IPD pre-amplifier pulses.

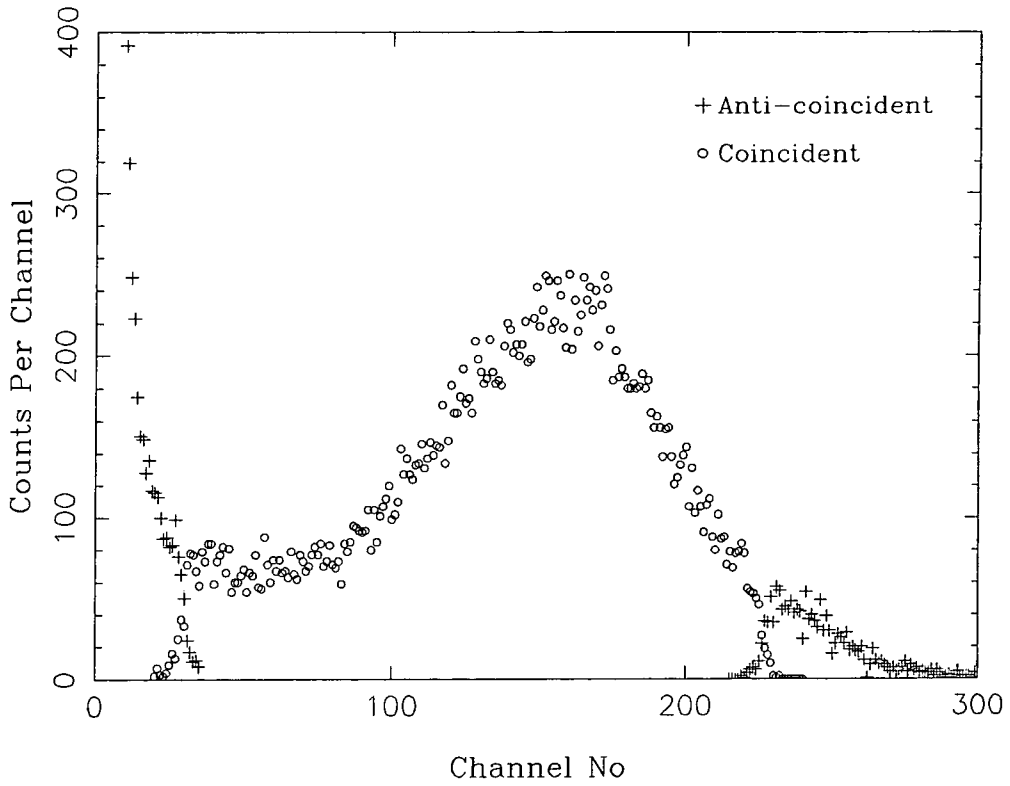

Figure 4.21: Pulse height spectrum of summed pre-amplifier pulses gated in anti-coincidence and coincidence with the IPD strobe pulse.

appendix D).

r_o	Magnitude Limit 1000sec Exposure		Magnitude Limit 3000sec Exposure	
	Martini	WHT	Martini	WHT
0.10	22.1	24.1	23.1	24.8
0.15	23.3	24.6	24.2	25.2
0.20	24.1	24.8	24.9	25.5

Table 4.2: V-band detection limits for astronomical imaging as a function of the coherence parameter r_o, for both the MARTINI system operating in full real-time image correction mode and the uncorrected full aperture WHT.

As can be seen from the table, the magnitude limits that the MARTINI system gives, even for excellent seeing conditions and assuming full tilt correction, are not as faint as that achieved by using the uncorrected full aperture of the WHT telescope. However, the limits are still deep enough to enable worth-while high resolution astronomy to be carried out.

4.11 Field of View

The maximum possible field of view achievable with the MARTINI system is governed by the size of the hole in the centre of the toroidal mirror which allows light from the Nasmyth focus to enter the system. The diameter of this hole is 25 mm corresponding to a field size of 109 arcseconds at the Nasmyth focal plane. However, this field will be vignetted due to the position of the aperture masks. The reason for this vignetting is that at the aperture mask the light from a field star is in the form of a ring 55 mm in diameter with a central hole of diameter 10 mm. If the light comes from a field point in the centre of the toroidal mirror hole this ring fits symmetrically over the mask of sub-apertures, but for a field point that is towards the edge of the toroid hole, this ring is displaced by the distance the

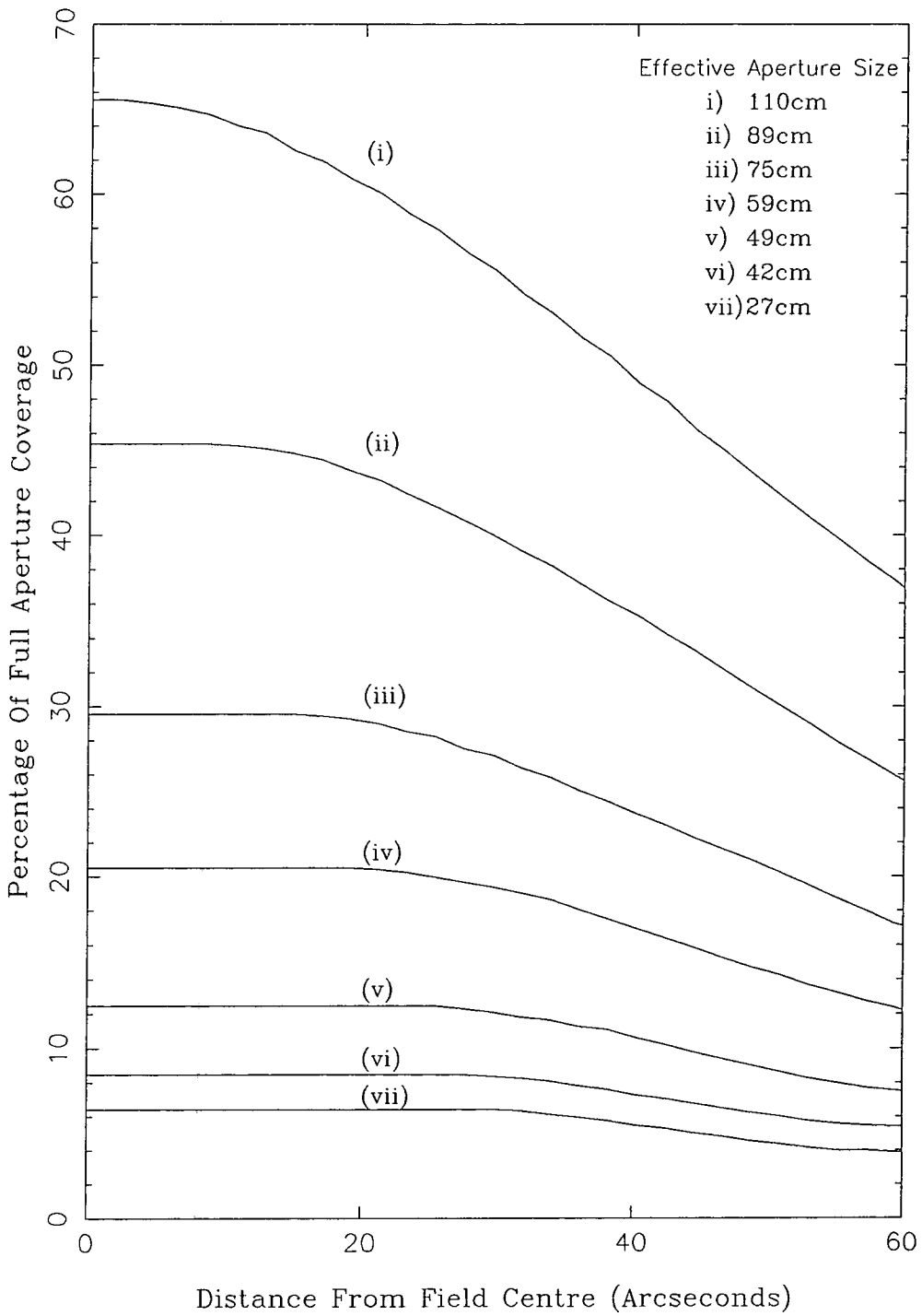

Figure 4.22: Variation of field intensity with distance from the centre of the toroid mirror for the selectable sub-aperture diameters.

point is from the centre. Therefore moving from the centre of the toroidal mirror, a point is reached where the ring of light from a field star does not wholly enclose the six sub-apertures and so vignetting occurs. The actual amount of vignetting is dependant on the sub-aperture mask size and the expected variation of vignetting for each of the aperture sizes available with MARTINI is shown in figure 4.22. Also shown in this figure is the percentage of the full aperture coverage that each sub-aperture mask provides.

4.12 MARTINI System Control

4.12.1 System Design

The requirements of the MARTINI control system are to read the X,Y coordinate pair produced by each detected photon event, determine the sub-aperture that the photon has passes though, determine the new position and motion of the guide star image in that sub-aperture, and update the active mirrors as to remove any image motion. The system has to perform these calculations in real time and be able to cope with photon arrival rates of up to 12 KHz (2 KHz per aperture channel). The system also has to control various peripheral devices such as aperture wheels and filter slides.

To satisfy these requirements a dedicated Motorola MC68020 microprocessor based system was chosen to perform the major event processing and tilt mirror positioning calculations. The programming and control interface to the 68020 system is through an IBM-AT personal computer connected to the 68020 via a fast link. A schematic representation of the overall design of the system is shown in figure 4.23. In the initial MARTINI design the 68020 system and the IBM-AT interface are situated in the GHRIL control room on the WHT Nasmyth platform, but in future developments of the system it is planned that the operation of the system will be remotely controlled via an Ethernet connection from the main WHT control room.

In reading the photon coordinates the 68020 employes a polling routine and on the arrival of a photon event from the IPD processing electronics the micropro-

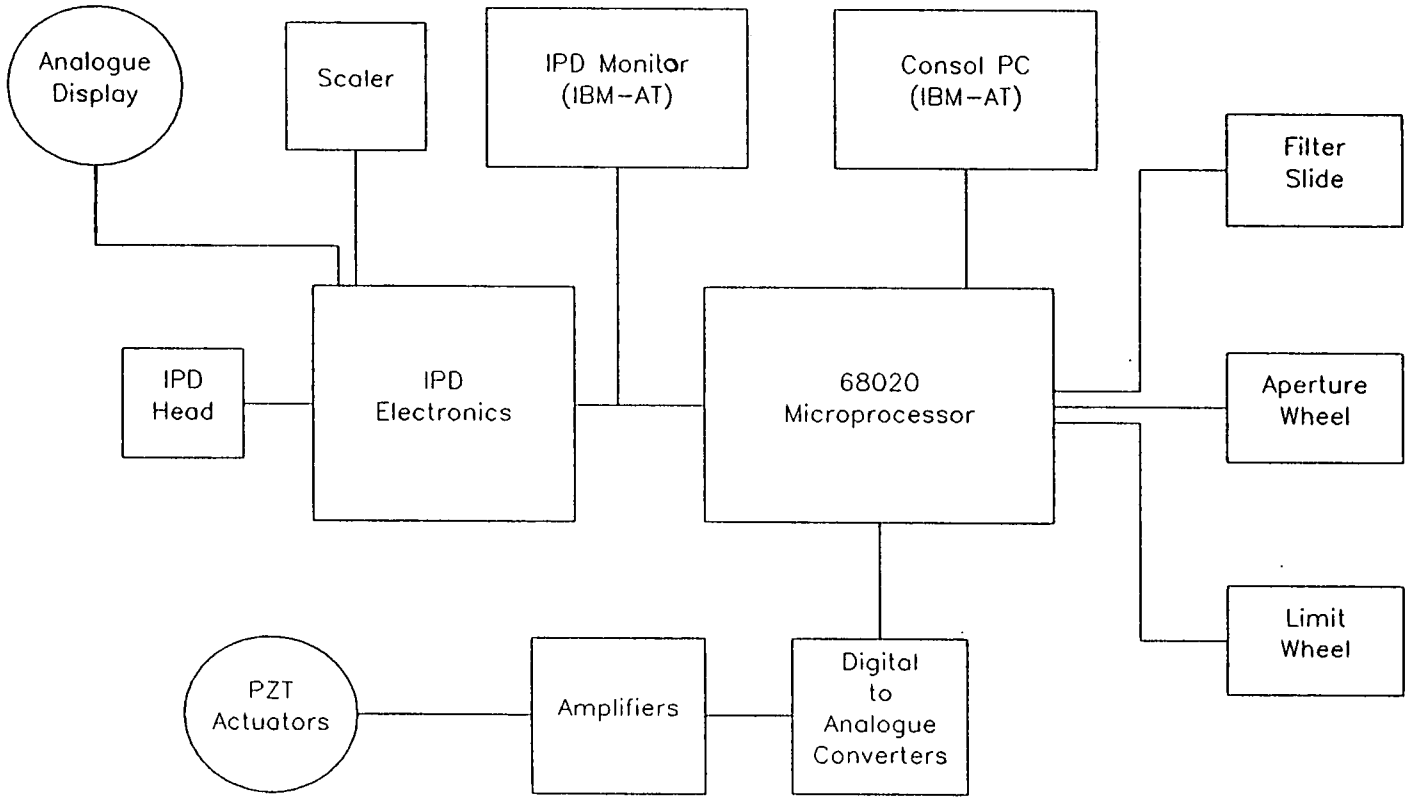

Figure 4.23: Schematic design of the MARTINI control system.

cessor unit computes whether the photon has fallen in an aperture or whether the photon is rejected as an noise event. If the event is rejected the system returns to the polling routine; if the event is accepted the event coordinates are used in the Cumulative Single Photon Servo (CUSPS) algorithm to calculate the new position of the aperture's guide star image and the voltages required to be applied to the PZL actuators in order that the guide star image is recentered. The required voltages for each actuator are calculated in the form of an 8-bit number which is then converted into an analogue voltage level via an eighteen channel digital to analogue convertor.

During the processing of an event the system is not completely dead to any other photon arrivals and the coordinates of up to two additional events can be stored, any more will be lost. This double-buffering causes the frequency response of the system to be relatively linear up to some limit where a rapid turn off occurs. For the algorithm used this limiting frequency was between 8–12 KHz (1300-2000 counts/second per aperture).

4.12.2 CUSPS-Cumulative Single Photon Servo

The IPD detector records a stream of photon positions from the six images of the guide star formed on the IPD. On each photon arrival in an aperture the new centroid position of the corresponding guide star image is calculated by means of the CUSPS algorithm. The object of this algorithm is to minimise the effects of the point spread function, background events, detector resolution, and errors due to inaccuracies in the positioning of the tilt correction mirrors.

When a photon is detected in an aperture, the offsets dx, dy of the photon from a reference origin in that aperture, determined beforehand using a fixed artificial star, are computed and added to cumulative indices Cx, Cy where

$$C_x = C_x + dx$$

$$C_y = C_y + dy.$$

These cumulative indices are then used as inputs to a low band pass linear digital filter. The filter used is of infinite response variety with a recurrence relation given

by

$$\overline{X}_N = fX_N + (1-f)\overline{X}_{N-1}, \tag{4.2}$$

where $\overline{X}$ is the output of the filter, X the input, and f a fraction such that $0 < f < 1$. This filter can conveniently be expressed in terms of its properties in the Z-transform plane as having a pole at $(1-f), 0$ and a zero at $0, 0$ (see figure 4.24). The frequency response $H(\omega)$ of the filter is given by the expression

$$H(\omega) = \frac{1}{\sqrt{1+(1-f)^2 - 2(1-f)\cos\omega T}}, \tag{4.3}$$

where T is the sample interval of the data (see figure 4.25).

The output of this digital filter is used to generate a estimate of the new required position of the tilt mirror $mpos_N$ as follows

$$mpos_N = g(\overline{X}_N + v(\overline{X}_N - \overline{X}_{N-1})), \tag{4.4}$$

where g is a gain constant and v a velocity constant. The inclusion of the velocity term is necessary since the use of the filter in estimating the star image centroid introduces an effective phase difference between the input and output.

The difference $nstep$ between the new mirror position required and the last mirror position $mpos_{N-1}$ is now calculated.

$$nstep = \frac{(mpos_N - mpos_{N-1})}{SF}, \tag{4.5}$$

where scale factor SF is a constant which converts pixel steps into the corresponding number of 0.0625 micron steps used in the piezo-actuator movement array $\mathrm{Hys}_{j,k}$ (see appendix E). The new voltage ma_N to be applied to the actuator to produce the required movement, was now found using the old voltage ma_{N-1} and $nstep$ as the indices of the array $\mathrm{Hys}_{j,k}$ so that

$$ma_N = \mathrm{Hys}_{ma_{N-1},nstep}. \tag{4.6}$$

If the required movement change was smaller than the actuator array step size it is ignored. It should be mentioned that when the system is working at the planned count rates the mirror position changes are expected to be small, so any errors introduced due to incorrect mirror positioning will be minimal.

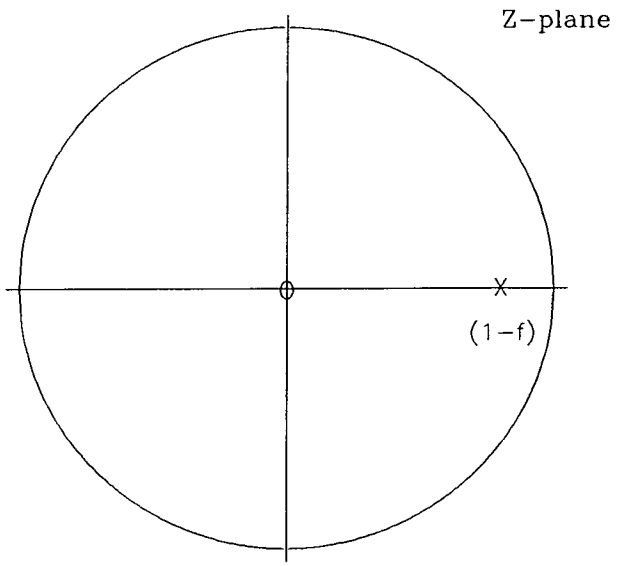

Figure 4.24: Z-plane representation of the CUSPS filter

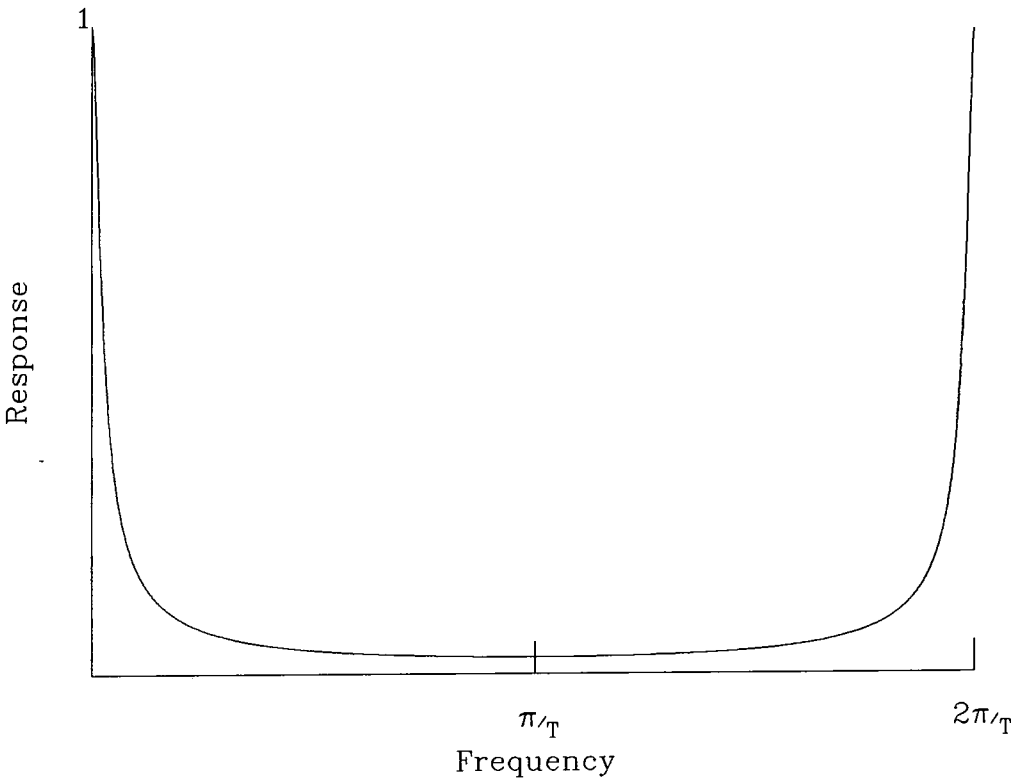

Figure 4.25: Frequency response of the linear digital filter

4.12.3 Computer Simulations of CUSPS Performance

A stream of real star photon event data was used to test the performance of the CUSPS algorithm. This data consisted of photon events from a single star image recorded on the IPD at high magnification and at a count rate of $\simeq 15,000$ photons a second. A lower count rate R_l was then produced by tagging photons at time intervals dt chosen randomly from a distribution given by $\exp(-dt/R_l)$. These tagged events were then used as the input to the CUSPS image sharpening algorithm. The corrected light output of the whole MARTINI system was simulated by subtracting the outputed value of the mirror position as calculated by CUSPS after each tagged event, from the positions of all the subsequent photon events in the untagged high rate stream.

Photon Rate (counts/sec)	CUSPS Parameters $1/f, v$	Uncorrected FWHM (arcsec)	Corrected FWHM (arcsec)
1000	140,12	0.60	0.51
2000	250,14	0.60	0.48
4000	310,16	0.60	0.42

Table 4.3: Performance of CUSPS for various input count rates. The FWHM that could be obtained from direct filtering of the high rate stream was 0.36 arcseconds.

This procedure was repeated for various values of the CUSPS input rate R_l and for each rate the parameters f, v of the filter were adjusted to produce the minimum root mean square (RMS) deviation of the final corrected image formed by the filtered photon stream. It was found that the CUSPS algorithm produced a similar degree of correction for a wide range of f values, but the choice of v is more crucial. Table 4.3 shows the image sharpening that was produced for inputed photon event rates to the CUSPS algorithm of 1000, 2000, and 4000 counts per second. The sharpened FWHM that could be obtained by a simple running mean

filter applied to the high rate stream was 0.36 arcseconds.

The degree of sharpening that could be attained by use of the CUSPS algorithm was not as good as expected and part of the reason for this can be seen in figure 4.26 which shows the power spectrum of image motion before and after CUSPS correction. The action of the CUSPS algorithm effectively reduces the low frequency image motion up to a 'cut-off' frequency where the corrected power spectrum rejoins the uncorrected spectrum. This cut-off frequency is determined by the photon count rate and the effective number of photon used in estimating the image centroid. No correction of image motion can be achieved at frequencies above this cut-off point and in fact the action of the CUSPS algorithm at frequencies just above the cut-off point seems to inject power into the image motion. This injection of power, might explain the limited sharpening performance and it is planned in future developments of the MARTINI system to remove this effect by the application of analogue filters to the voltage output.

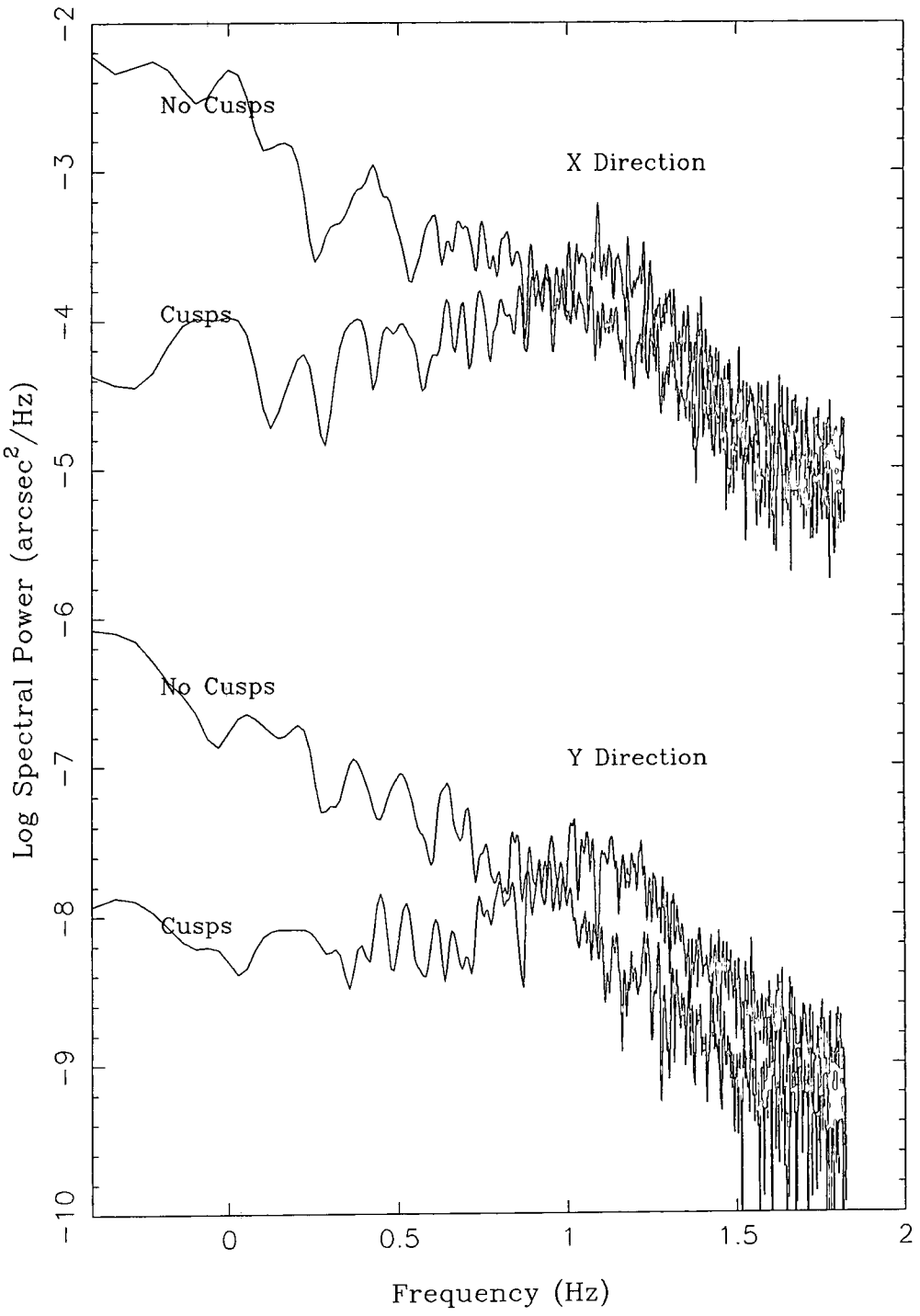

Figure 4.26: Power spectra of image motion before and after filtering with the CUSPS algorithm.

Chapter 5

Results Of The MARTINI Observations

5.1 Introduction

The MARTINI system has now been used at the WHT on four separate observing runs. The results described in this chapter were obtained during the first two runs, though results of particular relevance from the February run have been included. The first two runs were:

September 1988 : 3 nights using MARTINI in non-adaptive mode.

June 1989 : 5 nights using MARTINI in mainly real-time adaptive mode.

In the September run attempts were made to determine the characteristics of seeing at the WHT which are critical to the full adaptive operation of MARTINI. The characteristics that were investigated were:-

1. The size of the coherence parameter r_o and its variation. This gives information on the size of the $4r_o$ sub-apertures that can be used with the MARTINI system.

2. The power spectrum of image motion. This determines the range of frequencies in the image motion that must be removed in order to get adequate sharpening.

3. The degree of image sharpening that could be achieved with post-exposure superposition of short exposure images. This is equivalent to the technique of adaptive optics wavefront tilt correction used in the MARTINI system.

In the June run the main emphasis was on real-time adaptive image correction though non-adaptive post-exposure studies were made of seeing characteristics. The main aims of this run were:-

1. To investigate the performance of the real-time correction system.
2. To obtain information on the isoplanatic patch size for tilt correction.
3. To establish if an optimum aperture for tilt correction existed.

5.2 The September 1988 Run

5.2.1 Introduction

This observing run took place on the nights of the 21,22,23 September. The purpose was to to investigate the parameters of atmospheric seeing at the observatory site and gain first hand experience of installing and running the MARTINI optics and data recording systems at the WHT. Real time correction of astronomical images was not attempted during this run.

The optical arrangement used for the observations was basically the same as that shown in figure 4.1 of chapter 4, except that the piezo-translator driven tilt mirrors were replaced by a single plane mirror. Acquisition of stellar objects was attained by means of two CCD video cameras, one positioned before the toroidal mirror giving a low magnification wide field, and the other placed downstream of the re-imaged Nasmyth focus giving a small highly magnified field. The split lens assembly could be replaced with a selection of ordinary lenses to give a single high magnification image of an object on the IPD. The lenses available gave magnifications which corresponded to image scales of 3, 10, and 22 arcseconds over the full 38 mm extent of the IPD photocathode.

The toroid-tilt mirror axis of the MARTINI system was aligned along the mechanical altitude axis of the telescope. The altitude axis was used since it is easily defined by setting up a laser so that its light beam passed through the centre of two target plates that can be attached to either side of the telescope axis. This light beam can then be used as a reference in setting up the optical elements of the system. However, a slight problem arises in using the altitude axis in that it was found that this axis is not exactly coincident with the optical axis of the telescope system, thus causing images to describe a slow circular motion around some nominal point in the field of view. In this particular observing run, however, this did not pose any inconvenience as the duration of exposures were of only 5–10 seconds during which time there was negligible motion due to this effect. In fact, due to the short length of exposures, it was also considered unnecessary to have the WHT's Nasmyth image de-rotator in place.

The instrument used for recording the observations was the IPD detector. This was interfaced to an IBM-AT personal computer and the data was stored in the form of the 10-bit X and Y IPD pixel position and arrival time of individual photon events. The arrival time of each photon being determined using a 12-bit clock to a precision of 40 microseconds. Data was recorded and stored in sets of 100,000 photon events, this limit being imposed by the IBM-AT's available memory. Typically ten such 'timetag' data sets were taken in quick succession on each object observed. The astronomical objects chosen for study were a series of single and multiple stars. No colour filters or atmospheric dispersion corrector were used, so objects observed far from zenith were considerably effected by atmospheric dispersive effects.

5.2.2 Detected Count Rate

IPD count rates were recorded for a range of stars of different magnitudes, the incident flux of photons from bright stars being kept down to below 15,000 counts per second using neutral density filters in order to avoid local saturation effects on the IPD. The recorded rates were then corrected for the neutral density filter and the aperture size used for the observation, to obtain the nominal unfiltered rate that would be detected by the IPD through a single 40 cm aperture neglecting

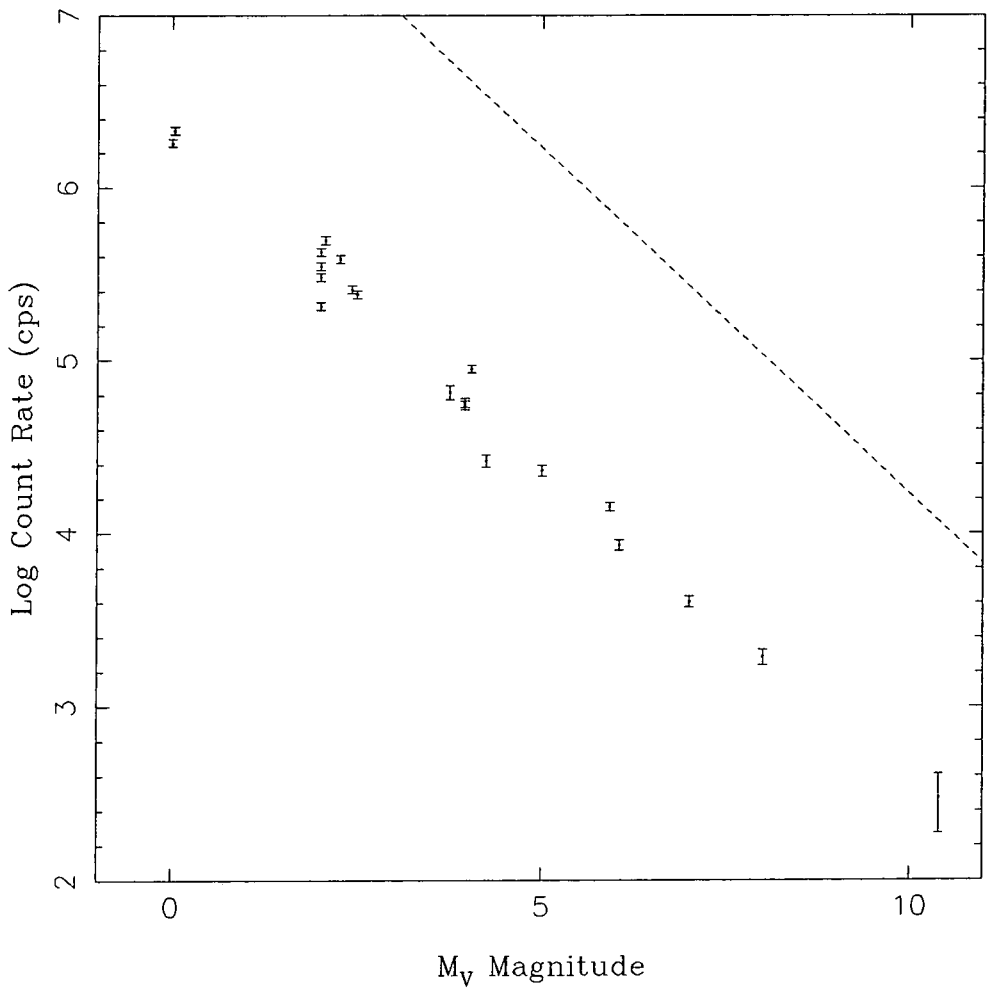

Figure 5.1: IPD Count rate versus star V–band magnitude. Also shown (dashed line) is the theoretically expected count rate to be detected by an IPD (peak DQE $\sim 8\,\%$) as calculated in appendix C.

such effects as the device dead-time and local saturation. Figure 5.1 shows these rates plotted against the star V–band magnitude, also shown in this figure is the theoretically expected photon count rate versus magnitude as calculated in appendix C assuming an IPD detector with a peak DQE of ~ 8 percent. As can be seen the count rates recorded by the MARTNI IPD was well below the theoretically expected values. This reduced performance was probably due to a combination of effects such as the low quantum efficiency of the IPD used in the observations (peak DQE of only ~ 1.5 percent) and light losses at the surfaces of the optical elements of the telescope and MARTINI system.

5.2.3 Post-Exposure Sharpening

Each 100,000 photon timetag data set was binned into sequential segments ('frames') of 7.5 ms duration. Typically for the 3 arcsecond field data this resulted in about 70 photons per frame. The time of 7.5 ms was chosen as sufficiently long to enable there to be enough photon events in each frame so that the position of the image centroid could be well established and problems of artificial sharpening avoided, whilst being still of a short enough length to ensure that there was negligible movement of the image due to seeing effects. A way of determining the optimum frame length was found to be by calculating the average movement of the centroid position between adjacent frames as a function of frame duration. If the frame duration is too short then there are too few photons in the frame to determine the centroid accurately and the centroid position just jumps around the point spread function and therefore the average centroid movement between frames is large. As the frame length is increased the average movement size is seen at first to decrease as the centroid is more accurately determined, but if the frame length becomes too long the seeing motion of the image begins to dominate and the average movement step size will begin to increase again. Therefore if the average step size between centroids is plotted against frame duration the resulting curve is seen to go through a minimum (such a curve is shown plotted in figure 5.2). Typically for the count rates used this minimum occurred at approximately 5 ms, thus the chosen frame time of 7.5 milliseconds is in the regime where problems of artificial sharpening are avoided.

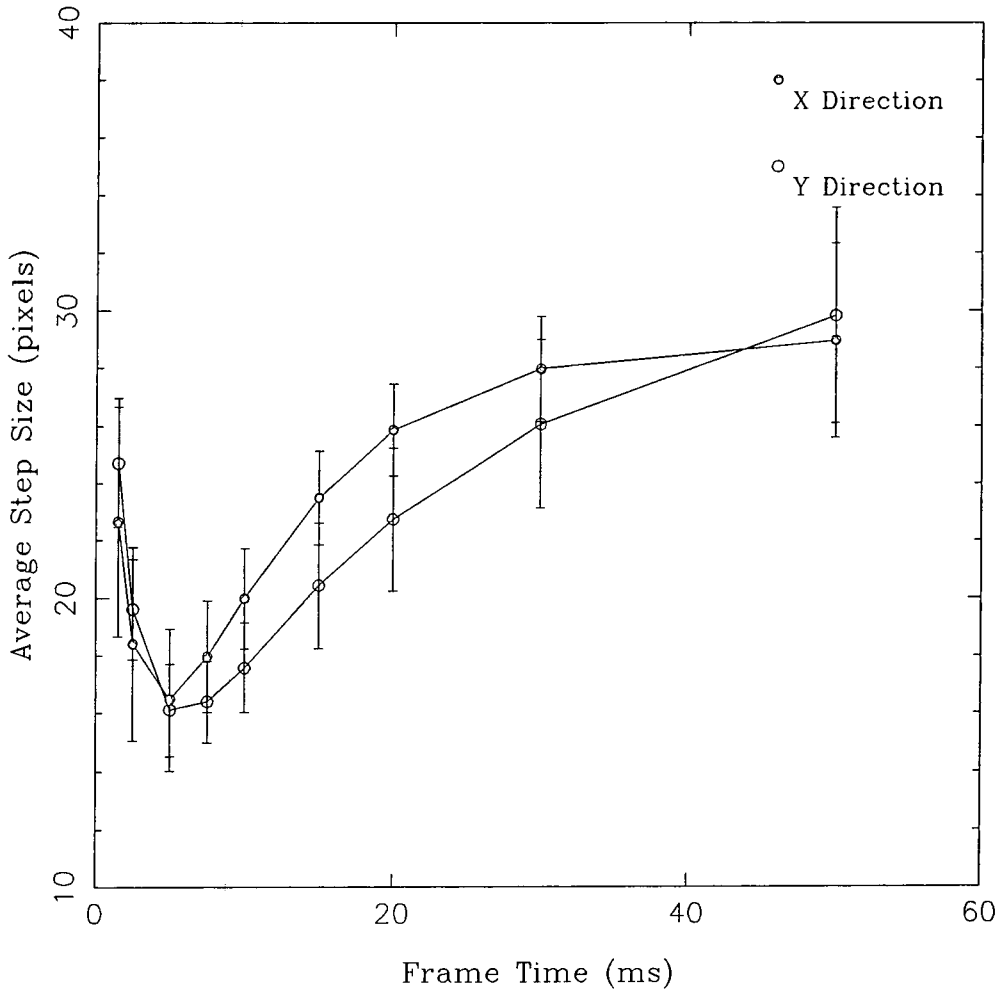

Figure 5.2: Average X and Y step size between centroids versus frame time for the star Beta Pegasi.

The centroid of the star image in a 7.5 ms frame was found using a two stage process in order to reduce the effects of background contamination. In the first stage the centroid was found using all the photons in the frame, whilst in the second stage a one arcsecond window was centered on this centroid and the centroid then recalculated excluding those photons that lay outside the window. The centroids thus determined were then used to centre and superimpose each frame to produce a sharpened 'short exposure' point spread function. The effect of the non-uniformity of the IPD photocathode efficiency was removed by multiplying each photon event in a frame by the inverse of the relative efficiency of the photocathode at the event's coordinate position. This procedure was repeated for each data set in a series of ten, and the resulting images were themselves superimposed. The 'long exposure' image was obtained by finding the average position of all the 100,000 photons events of a data set without binning and then using this value to recenter all the events. This recentering was necessary because, due to tracking errors, the telescope was repositioned between each 100,000 timetag data, thus the long exposure image could not be built up from the direct superposition of the ten data sets in a series. The final long exposure image therefore was obtained by superimposing the ten recentered timetag data sets of a series. Figure 5.3 shows a comparison of an image obtained by post-exposure sharpening to that of the long exposure image of the same object.

The full width half maxima of both the unsharpened and sharpened images were then measured by taking three parallel slices through each image, one slice through the peak pixel and the other slices one pixel either side of it. To avoid problems with the effects of atmospheric dispersion, the direction of the slice was chosen as to be orthogonal to the maximum distortion of the image. The resulting three slices were then summed and the peak value N of the resulting profile found. The FWHM of this summed slice was then determined by finding the points where the profile intersected the half peak value. Errors on the FWHM were estimated by re-determining the FWHM of the summed slice with peak values chosen of $N - 2\sqrt{N}$ and $N + 2\sqrt{N}$. Typical errors on the FWHM of long exposure images and on the post-exposure sharpened images were found to be ± 0.05 and ± 0.02 arcseconds respectively.

The results of post-exposure sharpening on the various stars observed on the

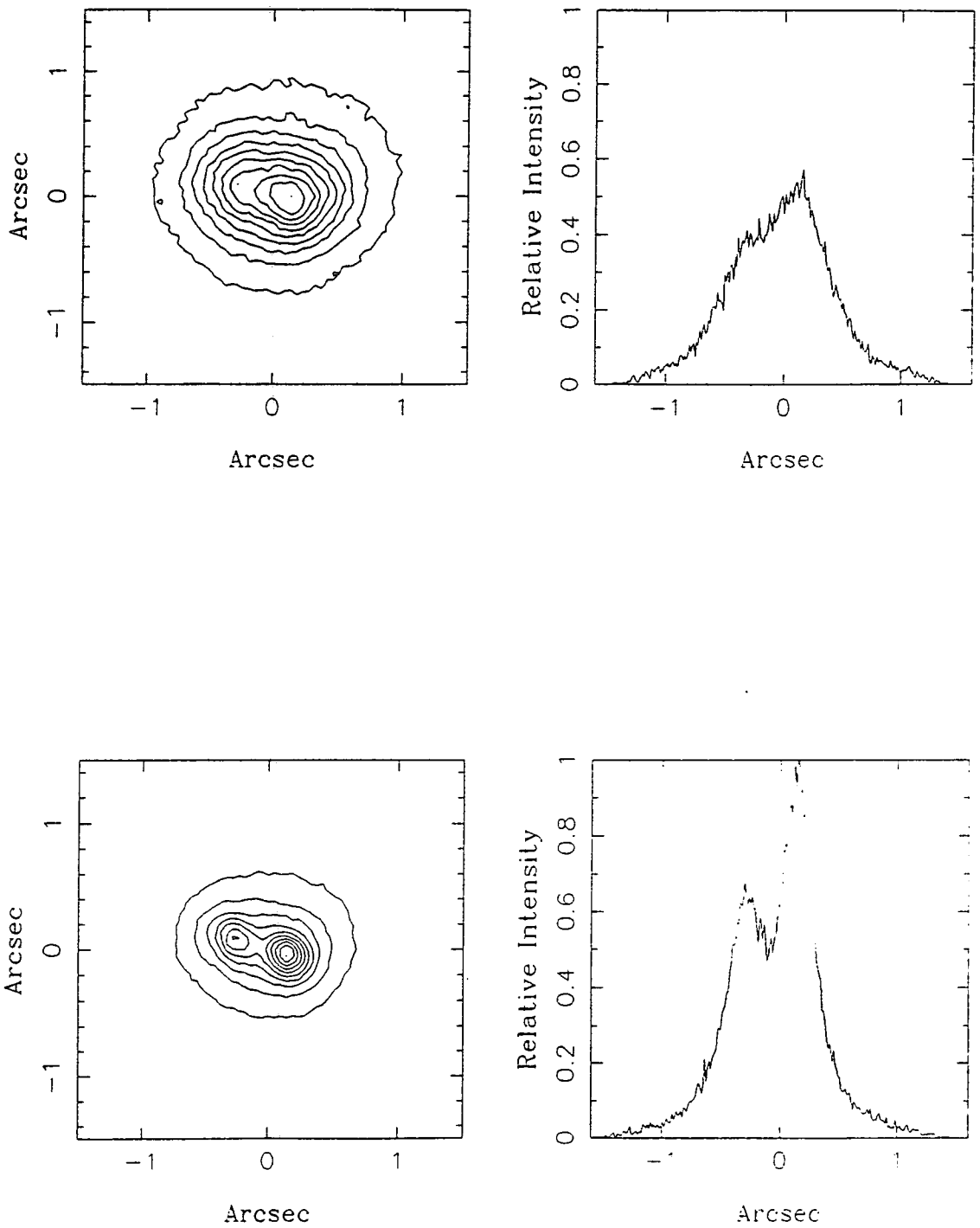

Figure 5.3: Contour maps and profiles of the binary star 72 Pegasi before (top) and after (bottom) post-exposure sharpening. The two components are separated by 0.5 arcseconds.

Time (BST)	Zenith Angle (degrees)	Aperture (cm)	FWHM Unsharpened (arcsec)	FWHM Sharpened (arcsec)	σ_m 10^{-2}arcsec^2
Night1					
04.48	9.6	40	0.51	0.31	21.2 $\pm$2.6
05.43	60.5	40	0.57	0.34	23.1 $\pm$2.9
06.27	39.1	40	0.83	0.36	30.2 $\pm$3.1
Night2					
00.04	27.7	60	0.53	0.26	19.7 $\pm$2.6
01.11	13.6	60	0.69	0.31	23.0 $\pm$3.6
01.40	34.0	60	0.61	0.26	22.8 $\pm$2.5
03.06	19.6	60	0.63	0.28	17.2 $\pm$2.2
03.10	19.6	60	0.58	0.30	17.1 $\pm$6.9
03.53	13.7	60	0.39	0.22	18.8 $\pm$2.1
Night3					
00.03	34.6	60	0.57	0.26	22.2 $\pm$2.6
00.26	8.2	60	0.59	0.26	22.1 $\pm$3.1

Table 5.1: Unsharpened and post-exposure sharpened full width half maxima and standard deviation of image motion for data recorded on the 1, 2, 3 September 1989.

three nights of the observing run are presented in table 5.1. Also shown in this table are the average standard deviations of image motion for each of the observations as calculated from the centroids established using the 7.5 ms binning technique.

5.2.4 Determination of L_o and r_o

The value of the coherence parameter r_o was estimated from the FWHM, given in arcseconds, of the long exposure unsharpened images using the relation, given in §2.6 of chapter 2, that

$$r_o = 2.0 \times 10^6 \frac{\lambda}{\mathrm{FWHM}}, \tag{5.1}$$

where λ was chosen as that wavelength that marked the mean point of the distribution $\mathrm{F}(\lambda)$ given by

$$\mathrm{F}(\lambda) = \mathrm{C}(\lambda)\,\mathrm{At}(\lambda)\,\mathrm{P_{Te}}(\lambda), \tag{5.2}$$

where $\mathrm{C}(\lambda)$ is the IPD photocathode efficiency, $\mathrm{At}(\lambda)$ is the atmospheric transmission and $\mathrm{P_{Te}}(\lambda)$ is the expected photon count rate for the particular effective temperature of the star observed. The resulting value of r_o was then corrected for its $\sec\theta$ dependance to obtain the nominal value at the zenith. The results that were obtained for the data recorded on the three nights of the observing run are shown in figure 5.4.

It must be noted that the equation 5.1 is only correct if it is assumed that the outer scale of turbulence is very much greater than the aperture diameter used for the observations. Evidence that this assumption may be incorrect is given in figure 5.5 which shows the FWHM of those long exposure images obtained through a 60 cm aperture plotted against the measured standard deviation of the image motion. Also shown are the theoretical curves, as derived in §2.5 of chapter 2, for various values of the outer scale of turbulence L_o. It can be seen from the figure that though the scatter of the experimental point is high, the majority of points lie above the $L \approx \infty$ curve indicating that this approximation is incorrect and that the true size of L_o may be only a few metres. The effect of having an L_o of such a length is to decrease the size of the long exposure FWHM expected for a particular given value of the coherence parameter, thus the r_o values determined using equation 5.1 are probably overestimates of their true size.

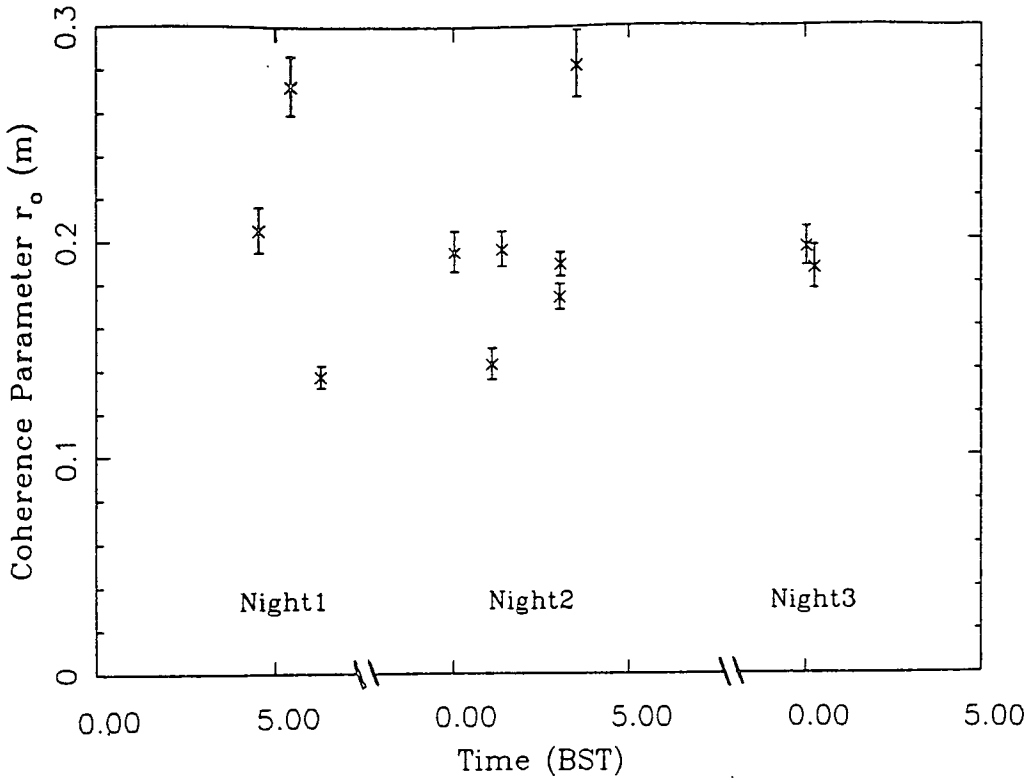

Figure 5.4: Value of the coherence parameter r_o at zenith as calculated from the long exposure full width half maxima.

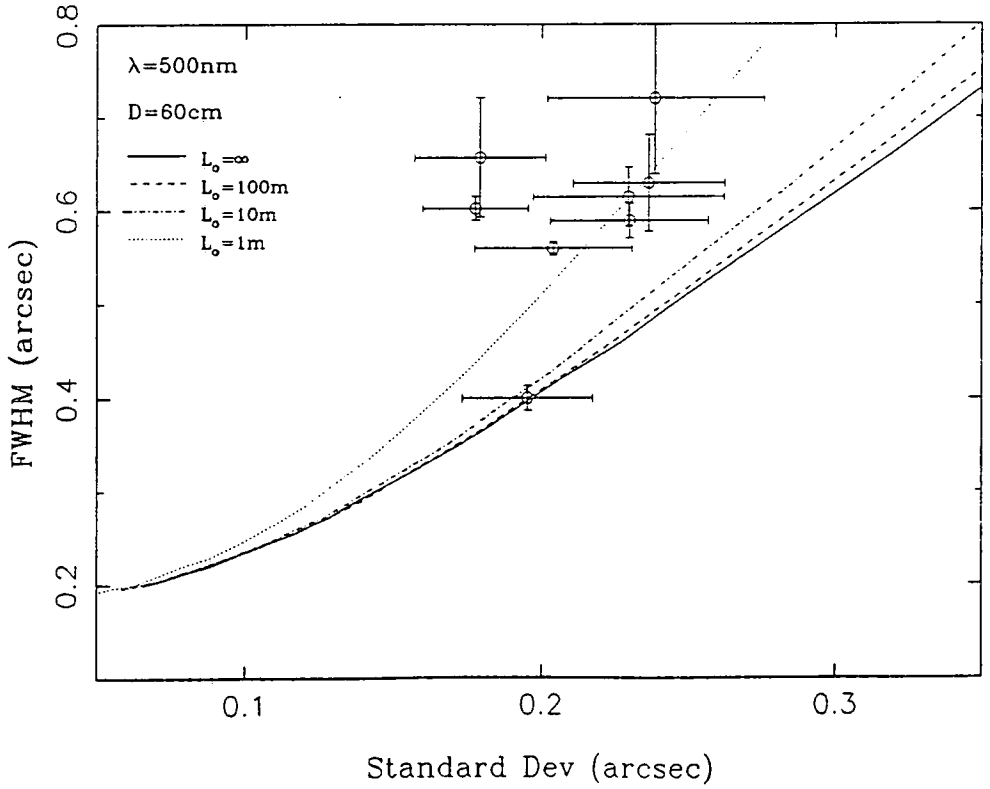

Figure 5.5: Plot of the full width half maximum of the long exposure images versus the standard deviation of image centroid motion. Also shown is the theoretical relationship expected for various values of the outer scale of turbulence L_o.

5.2.5 Point Spread and Modulation Transfer Functions

A fit was made to the experimentally determined unsharpened and post-exposure sharpened star image profiles with the long and short exposure profiles predicted from the seeing theory in §2.2.1 of chapter 2. The r_o value used in determining the theoretical profiles being chosen as to produce the profile that gave the least square error fit to the experimental data. A typical example of the results of this profile fitting for the star Beta Pegasi is shown in figures 5.6 and 5.7 (solid lines).

It was found in this profile fitting that a larger value of r_o resulted from the long exposure profile fitting that than determined from the the sharpened exposure fitting. As indicated in the previous section this discrepancy could be due to the effect of the outer scale of turbulence, as the theoretical profiles used for the fitting were calculated assuming L_o is effectively infinity. If the size of the outer scale of turbulence is in fact a few metres then this will have a major effect on the theoretical long exposure image expected, but the effect on short exposure imaging is small. Therefore the r_o value as determined from the post-exposure sharpened image was used in fitting the observed long exposure image with a profile as determined from the theory in §2.5 of chapter 2; with the value of L_o being chosen as to produce the best least square fit. An example of result of such a profile fitting is shown in figure 5.6 (dashed line).

5.2.6 Power Spectra of Image Motion

From the 'timetag' photon data of the star images recorded on the 3 arcsec image scale, a time series of image centroid positions, $X_1, X_2 \ldots X_{N-1}, X_N$, was determined using the method outlined in §5.2.3. Using these positions the autovariance of the image centroid motion was calculated for both X and Y motion. The autocovariance function c_k is given by

$$c_k = \frac{\sum_{n=0}^{n=\mathrm{N}-k} X_n X_{n+k}}{\mathrm{N} - k}, \tag{5.3}$$

All the autocovariance curves so produced show a spike at zero time shift due to the influence of the random nature of the point spread function. To remove this

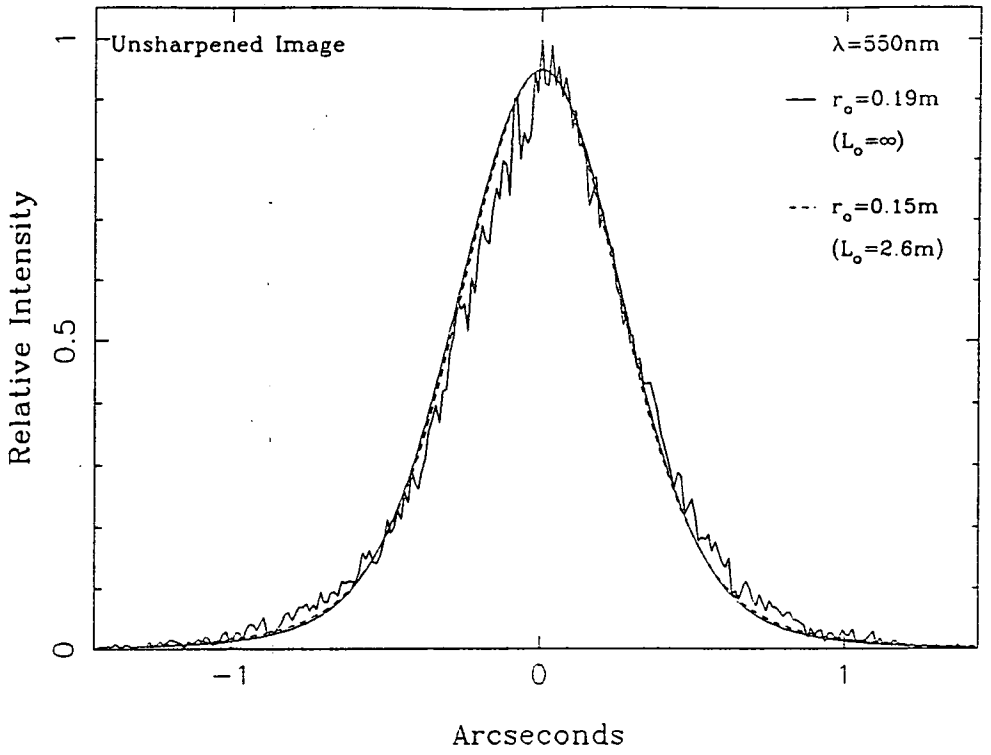

Figure 5.6: Results of the profile fitting of the long exposure image of Beta Pegasi. Shown are the theoretical profile fits achieved assuming $L_o \gg D$ (solid line) and (dashed) an L_o of 2.6 m.

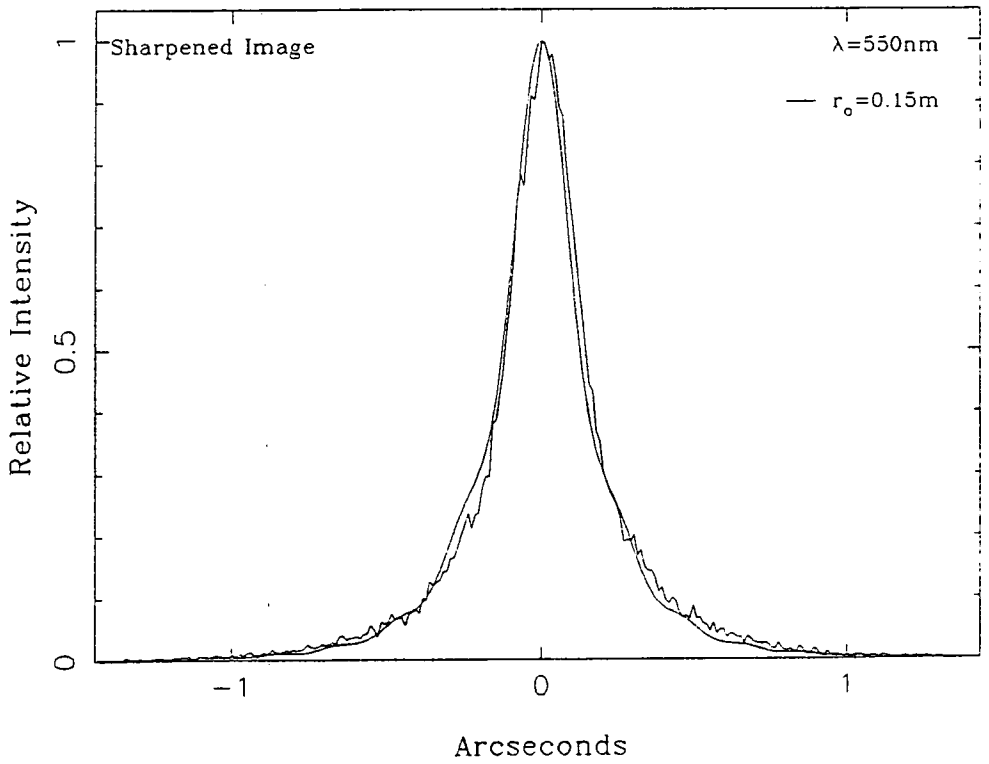

Figure 5.7: Results of the profile fitting of the post-exposure sharpened image of Beta Pegasi.

effect the zero shift term was reset as

$$c_0 = c_1 + \frac{c_1 - c_2}{2}.$$

The power spectrum of image motion, $P(f)$, was determined from the autocovariance using the relation

$$P(f) = \alpha_o c_0 + 2 \sum_{k=1}^{k=k_{max}} \alpha_k c_k \cos(2\pi f k dt), \tag{5.4}$$

where α_k are a set of Parzen Window smoothing constants given by

$$\alpha_k = 1 - 6\left(\frac{k}{\mathrm{N}}\right)^2 + 6\left(\frac{k}{\mathrm{N}}\right)^3 \qquad 0 \leq k \leq \frac{\mathrm{N}}{2}$$

$$\alpha_k = 2\left(1 - \frac{k}{\mathrm{N}}\right)^3 \qquad \frac{\mathrm{N}}{2} \leq k \leq \mathrm{N}.$$

The highest frequency up to which the power spectrum can be investigated is limited by the time duration τ of the frames used to determine the star image centroids. This upper frequency limit f_{Nyq}, termed the Nyquist frequency, being given by

$$f_{\mathrm{Nyq}} = 1/2\tau.$$

Since the length of the frames used was 7.5 ms this gave an upper frequency limit of 66.6 Hz. The low frequency limit to the power spectrum is determined by the total duration of individual timetag data sets which, depending on the photon count rates, was for most sets about 5–7 seconds giving a lower frequency limit of between 0.3–0.4 Hz.

Using the method outlined above, power spectra were determined for each of the timetag data sets in an observation set of ten and these individual power spectra were then co-added to obtain an averaged power spectrum. On the first two nights of the observing run it was found that the power spectra curves obtained showed a behaviour over most of the frequency range that obeyed an approximately $f^{-\frac{5}{3}}$ power dependency on the frequency with a slight turn over at low frequencies to a power dependency of approximately $f^{-\frac{2}{3}}$. Such a typical power spectrum obtained on the first night for the star Alpha Arietis is shown in figure 5.8. The power spectra obtained on the third night, however, seemed to exhibited a slightly sharper fall off at high frequencies and figure 5.9 shows such a power spectrum obtained on the third night of the run for the star Beta Pegasi. Though it is

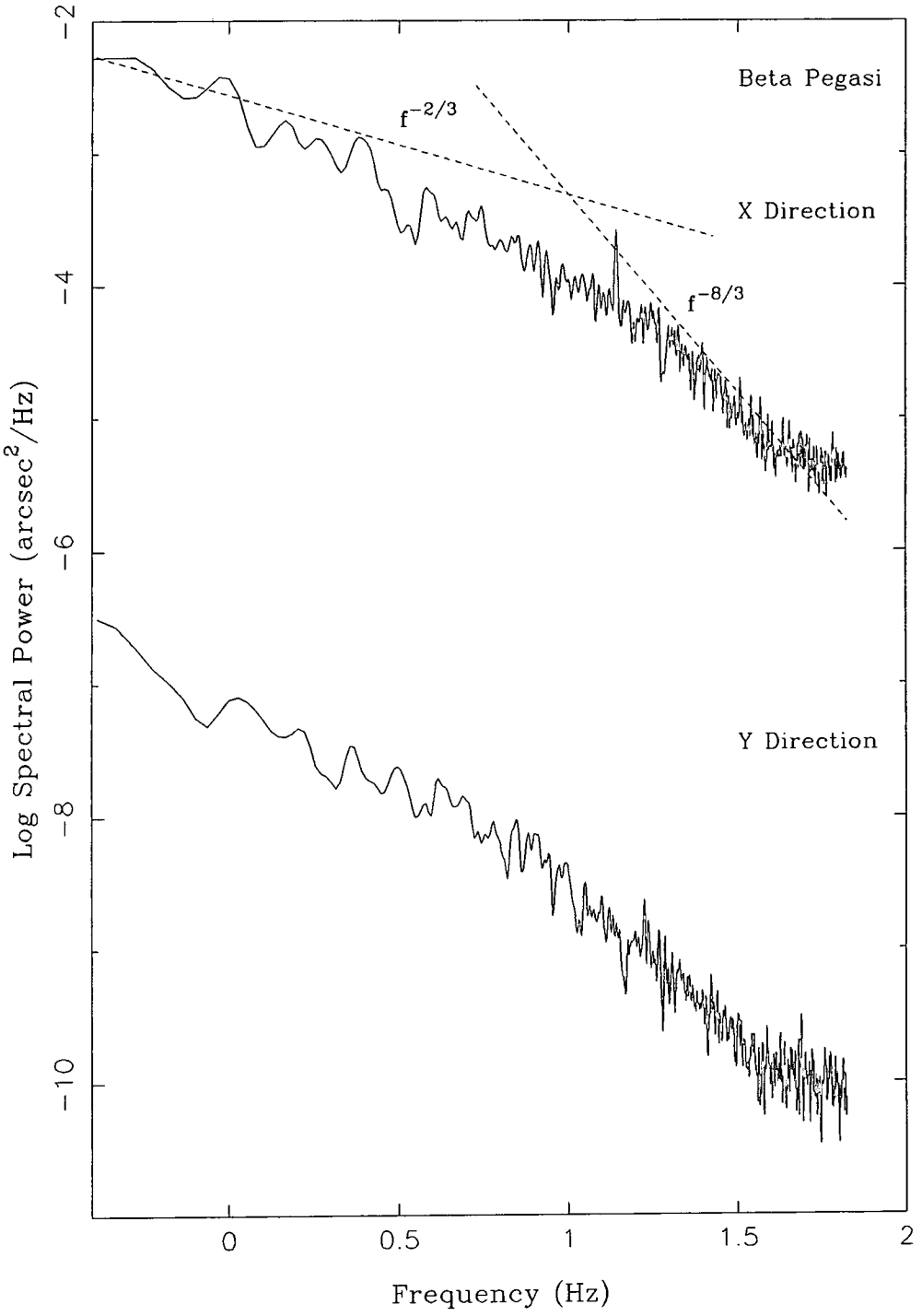

Figure 5.8: The X and Y power spectra of image motion for Alpha Aries observed on the night of the 21/9/88 through a 40 cm aperture. The Y direction power spectrum is plotted shifted down by a factor of 10^{-4}.

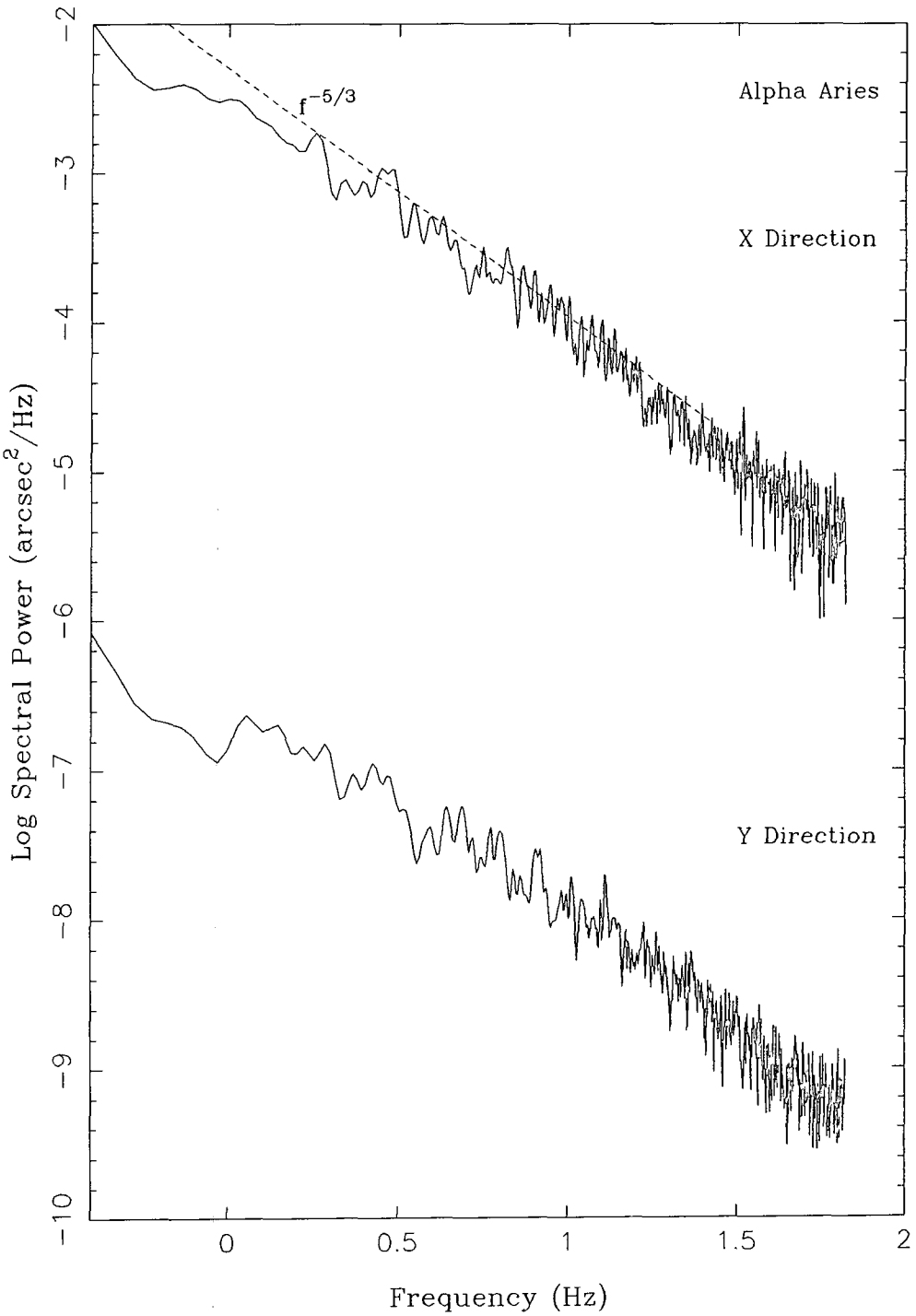

Figure 5.9: The X and Y power spectra of image motion for Beta Pegasi observed on the night of the 23/9/88 through a 60 cm aperture. The Y direction power spectrum is plotted shifted down by a factor of 10^{-4}.

not evident in these figures, several of the power spectra obtained over the three nights also showed a peak in power at a frequency of 2–3 Hz. The origin of this peak has been established as due to the mechanical vibrations of the telescope, intermittently excited by observer movements on the Nasmyth platform.

5.3 The June 1989 Run

5.3.1 Introduction

This observing run took place on the nights of the 5,6,7,8 and 9 June. Full real-time correction of images was performed as well as the collection of timetag data sets for post-exposure sharpening. An optical arrangement similar to that given in figure 4.1 of chapter 4 was used, the only difference being that the beam splitter used to divert light to the IPD was positioned a few centimetres in front of the re-imaged Nasmyth focus. The real-time corrected output of the system was recorded by either a cryogenically cooled CCD camera placed directly at the re-imaged Nasmyth focal plane or by a video camera, the light being switched between the two by the insertion of a plane mirror just behind the beam splitter.

The cooled CCD camera used was a Wright Instruments design, equipped with an uncoated P8603 GEC chip giving a 576×399 pixel readout; the physical size of each pixel being $16 \times 16\,\mu$m. In the arrangement used, with the CCD placed directly at the re-imaged Nasmyth focus, the magnification was such that a single pixel corresponded to 0.075 square arcseconds of sky. The total field achievable was therefore 43×30 arcseconds. All the observations with the CCD camera were made through a Kitt Peak R band filter and, as in the September run, the objects chosen to be observed were a selection of single and multiple stars.

The procedure adopted when setting up for a real-time correction run, was as follows. Using an artificial star, the images formed on the EEV video camera by each of the six apertures in a mask were focused by adjusting the position of the video camera until the diffraction limited images were obtained. When this had been achieved, the voltages on the piezo-actuator driven tilt mirrors were adjusted so that the six images were coincident. The plane switching mirror was then inserted and the artificial star images were focused on the cooled CCD camera by adjusting the camera's position such that the images formed by the sub-apertures were again coincident. Finally the IPD was focused by adjusting the split-lens assembly. When the artificial star focusing procedure was complete the centroid positions of the images formed on IPD were recorded and these positions were then used as the origins in each aperture to which the images of a real guide star

would be corrected too.

The focusing of a real star image was then done visually using the high magnification video camera. In fact accurate focusing would seem to be critical since, using the full aperture of the telescope, an error of only 0.1 mm in the positioning of the secondary mirror produces a 2 mm error at the f/11 Nasmyth focus corresponding to a 0.8 arcsecond blurring of an image. In the MARTINI system with its sub-aperture masks, the major effect of such a focusing error would be to produce a separation of the images formed by sub-apertures at the re-imaged Nasmyth focus. However, the operational procedure of MARTINI makes this less of a problem since during real-time correction the images on the IPD are always corrected back to the origins established by the artificial star and this forces the 6 individual images at re-imaged Nasmyth focus to be coincident. Thus the focusing is essentially similar to that of a single aperture with its higher f-number and correspondingly greater depth of field. This is not to imply, however, that focusing is not important and indeed more accurate focusing methods have been developed in subsequent runs.

The correct matched aperture size for the particular seeing conditions prevalent at the time of an observation was found to be best established visually using the high magnification video camera monitor. A range of apertures was quickly run through and the best one chosen as the aperture size at which the image began to depart from a simple diffraction limited image and show a tendency to break up into speckles.

5.3.2 Post-Exposure Sharpening

In order to investigate the prediction of seeing theory that an aperture size exists at which the improvement to be gained in image sharpening is maximised, a range of aperture sizes were selected in quick succession whilst observing a single star. A set of ten 'timetag' observations were made with each aperture and these data sets were then post-exposure sharpened using the same techniques as described in §5.2.3, except that this time the telescope was not repositioned between individual timetag observations and so the long exposure images could be constructed from the direct superimposition of the data sets without recentering the images in each

one.

The FWHMs obtained after the post-exposure sharpening, along with the corresponding unsharpened FWHM values, are given in table 5.2 and these values are also shown plotted versus the aperture diameter of the observation in figure 5.10. It can be seen from this figure that, as seeing theory predicts, there is an optimum aperture size at which a minimum sharpened short exposure FWHM is obtained. This minimum occurred at an aperture size of approximately 60 cm, which according to seeing theory should correspond to $4r_o$, thus indicating a coherence parameter of 15 cm. Using this value of r_o the theoretically predicted long and short exposure FWHM versus aperture diameter curves for various values of the outer scale of turbulence were determined and these are also shown in the figure. As can be seen the theoretical short exposure curve agrees well with the experimental points. However, the long exposure result would only seem to be in agreement with theory if the outer scale of turbulence is assumed to be of the order of a few metres in size.

5.3.3 Real-Time Image Sharpening

The corrected output of the MARTINI system was recorded by a CCD camera and in order to establish the amount of sharpening that was achieved though real-time correction, observations of the stars chosen as targets were recorded in pairs, one CCD exposure being taken with the adaptive mirrors flattened but switched off, and immediately following that an exposure during which real-time adaptive correction was performed. The performance of the real-time correction could also be monitor visually on a real-time display of the six images formed on the IPD used as the wavefront tilt sensor.

The FWHM obtained for the uncorrected and real-time corrected images of a series of binaries are shown in table 5.3. The best sharpening that was achieved was for the binary star HD187613, the image of which was sharpened to 0.35 arcseconds, and figure 5.11 shows the profiles through the uncorrected and real-time corrected images of this binary. It is clear from this figure that the companion star 9.6 arcseconds away from the star used for the wavefront tilt sensing is considerably sharpened too, showing that the diameter of the isoplanatic patch for

Aperture (cm)	FWHM Unsharpened (arcsec)	FWHM Sharpened (arcsec)	σ_m (arcsec 10^{-1})
27.49	0.58	0.40	2.07 ±0.18
41.96	0.44	0.31	1.43 ±0.20
47.82	0.55	0.28	1.50 ±0.33
58.37	0.45	0.25	1.35 ±0.23
74.92	0.58	0.26	1.32 ±0.18
89.55	0.45	0.33	1.34 ±0.23
110.57	0.53	0.39	1.50 ±0.41

Table 5.2: Unsharpened and post-exposure sharpened full width half maxima obtained for a variety of aperture sizes selected in quick succession.

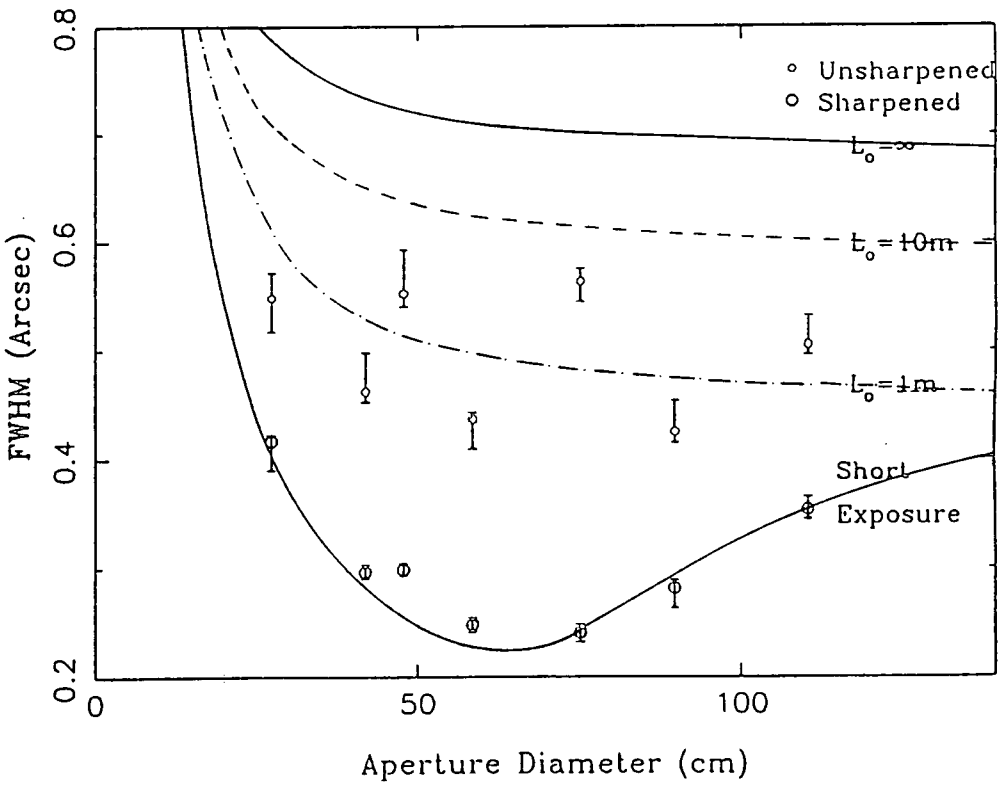

Figure 5.10: FWHM Versus Aperture Diameter for the unsharpened and post-exposure sharpened data. Also shown are the theoretical expected results for an r_o of 15 cm and L_o values of infinity, 10 m, and 1 m.

tilt correction was at least $\simeq 20$ arcseconds.

As can be seen from the table the improvement in the FWHM was not as great as that seen in the results of post-exposure sharpening. A possible reason for this comes from the visual observation that when real-time correction of an image was being performed that though the gross motions of the image were removed, there seemed to be a broadening of the instantaneous point spread function due to injected high frequency noise. From simulations of the performance of the CUSPS algorithm (see §4.12.3 of chapter 4) such a high frequency noise injection is in fact expected.

To investigate this effect, the power spectrum of image motion was determined for series of ten timetag data sets recorded before and during real-time correction with MARTINI. The timetag data sets being recordings of the photon events in the six images formed by the split lens on the IPD. The power spectrum of image motion for each data set was then determined using the following procedure. The centroid motion of the six images in a data set was determined using a binning technique as in §5.2.3. As the photon rates recorded were only between 1000–2000 counts a second per aperture, when binning the data frames times of 25 milliseconds were necessary in order to establish the image centroids accurately. The autocovariance function was then calculated from the centroid motion for each of the six images and the resulting functions were co-added to produce an average autocovariance function. The power spectrum of image motion was then calculated from this average autocovariance. This procedure was repeated for each of the ten timetag data sets which constituted a single observation and the resulting power spectra averaged. Due to the frame binning times the upper frequency limit to the power spectrum that could be investigated was 20Hz. Figure 5.12 shows the power spectrum of image motion obtained before and during MARTINI real-time tilt correction. As can be seen the system successfully reduces the power of the motions with frequencies of up to $\sim 15\,\mathrm{Hz}$ (this upper frequency limit is set by the photon count rate and the effective number of photons used in the CUSPS algorithm to determine the image centroid). Above this frequency there seems, as expected from the simulations of §4.12.3 of chapter 4, to be some injection of high frequency motion the exact extent of which could not be investigated with the photon count rates used.

Object	Aperture (cm)	Separation (arcsec)	FWHM Uncorrected (arcsec)	FWHM Corrected (arcsec)
100 Her				
a)	47.82	14.3	0.63	0.43
b)			0.67	0.50
100 Her				
a)	74.92	14.3	0.63	0.41
b)			0.65	0.58
95 Her				
a)	47.82	6.3	0.58	0.45
b)			0.54	0.49
95 Her				
a)	74.92	6.3	0.50	0.41
b)			0.52	0.43
HD187613*				
a)	47.82	9.6	0.60	0.40
b)			0.68	0.50
HD187613*				
a)	74.92	9.6	0.54	0.36
b)			0.65	0.47
* - (b) component is a 0.3 arcsecond binary.				

Table 5.3: Real-time image correction results of a series of binary stars. The stars in the binary are given as (a) and (b) with the (a) star being the component used for guiding. The CUSPS constants f,v used for the observations were 0.02 and 20 respectively.

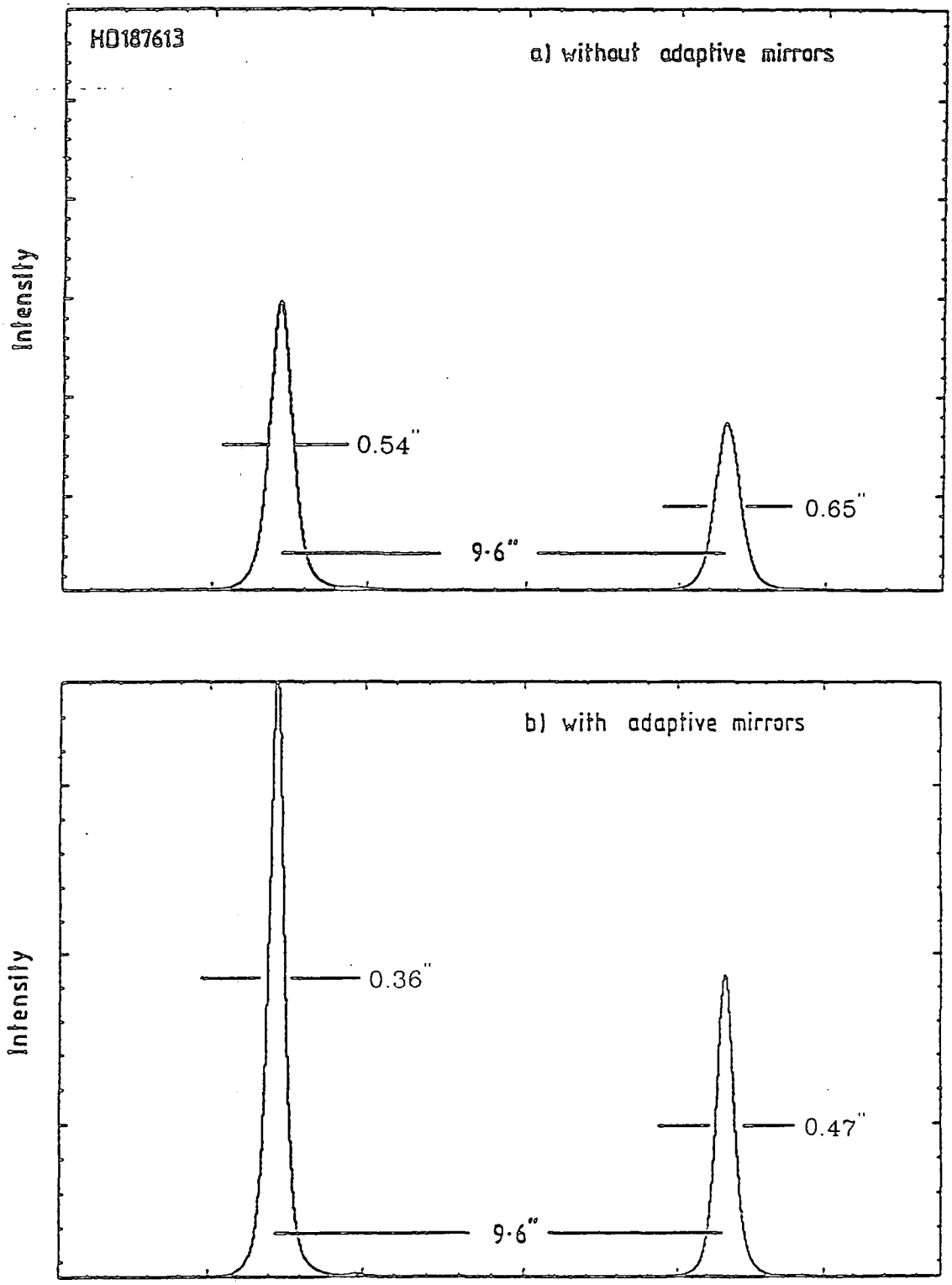

Figure 5.11: Profiles of the binary star HD187613 for both unsharpened and real-time corrected CCD images. The star on the left was the one used as the reference object for the wavefront tilt detection. The star on the right is an unresolved 0.3 arcsecond separation binary.

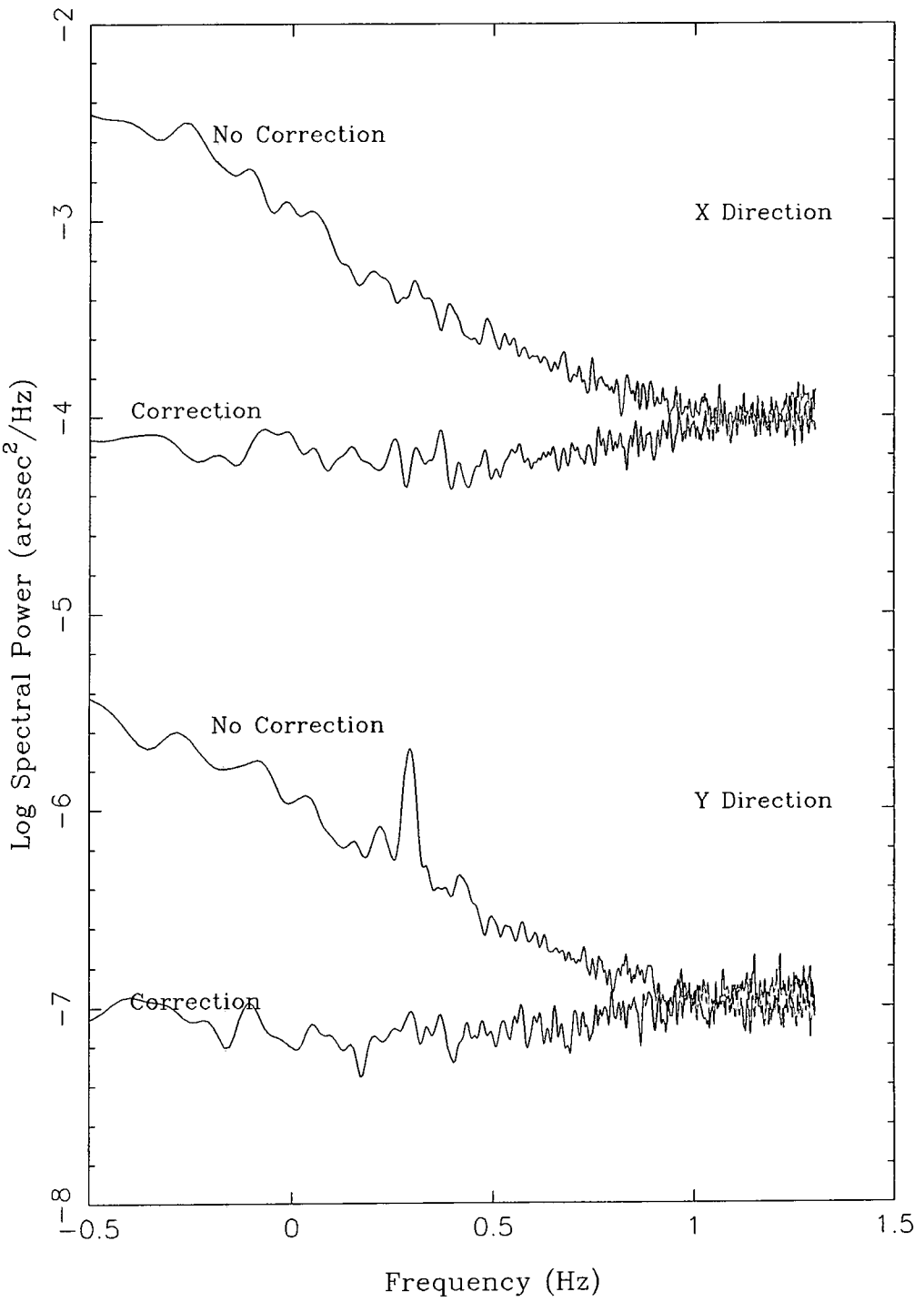

Figure 5.12: Power spectra of image motion with and without real-time adaptive image correction.

5.4 The February 1990 run

This run took place on the nights of the 27–28 February, and the 1–2 March 1990. The main goal of the run was to record high resolution real-time corrected CCD images of galaxies in the Virgo cluster. The astronomical motive for obtaining such images is that if these galaxies can be resolved into their individual stars, then the brightest stars in the galaxies can be used as distance indicators (see SAND GE AND CARSON [71]).

The optical set up used for the observations was different to that of the previous observing runs with MARTINI. The IPD detector was positioned to receive the transmitted light from the beam-splitter positioned at the secondary Nasmyth focus whilst the reflected light was imaged on to the cryogenically cooled CCD camera, this CCD camera being the same as used in the June run. The magnification of the CCD imaging optics was arranged such that a single CCD pixel corresponded to a sky area of 0.1×0.1 arcseconds thus giving a full field of view of 40×57 arcseconds. The CCD video camera previously used for star acquisition was replaced with an intensified CCD camera to facilitate the location of the faint stars used as the MARTINI system reference objects. The IPD used in this run was equipped with a refurbished photocathode with a peak RQE of $\sim 20\%$. The overall DQE of the whole device was $\sim 4\%$. This increase in efficiency allowed guide stars of 13^{th} magnitude to be used.

A new 'Hartmann' technique of focusing the CCD and IPD images was implemented utilising the effect that, with a multi-aperture system such as MARTINI, the images formed by each of the apertures at a fixed plane separate as the focus is moved in either direction away from this plane. If this image separation is measured for several different focal positions on either side of the optimum, an interpolation can be made to determine the exact position where the images all coincide (care has to be taken in this technique in avoiding backlash problems in the focusing mechanics by always driving the focus in the same direction when making measurements). Using this Hartmann method of focusing it was estimated that the focusing of the real star image could be established with an accuracy in the secondary mirror positioning of ± 0.02mm.

Figure 5.13: CCD image of the Virgo galaxy IC3583 (from Tanvir [72]). The picture represents an area of sky of 40×57 arcseconds and the guide star used for the observations is the object just to the right of the picture centre (the central portion of the star is whited out due to saturation effects). The object at the bottom of the picture is a ghost image of the guide star caused by the beamsplitters in the optical train.

Unfortunately the weather during the observing run was poor and only on one of the nights were good seeing conditions encountered. On this night real-time corrected CCD images of the Virgo galaxy IC3583 were obtained, and such an image is shown in figure 5.13. The corrected seeing that was achieved, as measured from the FWHM of the guide star, was 0.65 arcseconds.

5.5 Summary Of Results

The results of the non-adaptive investigation of the atmospheric parameters at the site have established that:-

1. The value of the coherence parameter r_o was typically between 15–20 cm for both the September and June observing runs.

2. There is an optimum aperture size at which the sharpening achieved by short exposure superposition is maximised. This confirms the predictions of the seeing theory due to Fried given in §2.3 of chapter 2. However, the amount of sharpening that is achieved is less than the factor of three that theory suggests might be gained. This reduction in the achievable sharpening might be due to the effect of the outer scale of turbulence L_o, which the experimental results would seem to suggest is of the order of a few metres in size.

3. The power spectra of image motion determined are consistent with those predicted by the theory outlined in §2.8 of chapter 2. If the seeing is due to a single layer, theory predicts that the power spectrum should show a $f^{-\frac{2}{3}}$ dependency at low frequencies with a turn off to a $f^{-\frac{8}{3}}$ dependency at high frequencies. This behaviour has been seen in the experimentally observed power spectra, but most of the curves experimentally determined showed an extended region where the power spectrum followed a $f^{-\frac{5}{3}}$ dependency. Such a result is expected if, as is likely to be the case, seeing is due to multiple layers of turbulence.

The results of adaptive real-time image correction with the MARTINI system have established the following:-

1. The adaptive mirrors do null the gross image motions as observed on the real-time IPD display. Sharpening of the images recorded on the output detector is achieved, with the best corrected image FWHM so far obtained being 0.35 arcseconds in size .

2. When real-time correction is examined through the power spectrum of image motion, it is seen that frequencies of motion up to 15 Hz are successfully removed. At the lowest frequencies studied the action of the real-time correction is to produce a reduction in the power spectrum by a factor of 50–100.

3. The degree of sharpening is not as great as that indicated as being possible from the results of post-exposure sharpening. Part of the problem is the injection of noise above the effective sampling frequency of the system due the action of the servo tracking algorithm.

4. The real-time correction of binary stars has shown that the isoplanatic patch for wavefront tilt correction is at least some tens of arcseconds in size.

Chapter 6

Developments Of The MARTINI System

6.1 MARTINI II

At the present time a MARTINI II system is being built, incorporating various modifications to improve the system performance and to produce a more 'user friendly' device that is easier to set up and operate. The major changes in the system are as follows:-

1. Computing Control: This is the area in which the major changes are being implemented. The IBM-ATs, which are at present used for interfacing to the 68020 microprocessor unit and for monitoring the IPD detector, are being replaced with a single 33 Megahertz i386 microprocessor Elonex personal computer running a Unix based X-windows environment. This system is designed to be operated remotely, via an Ethernet connection, from the WHT control room, instead of as at present the Nasmyth GHRIL control room. This will provide a more comfortable user environment, and remove any problems associated with exciting mechanical oscillations of the GHRIL platform.

2. Automated Control: Control of the various beam splitters and filters in the system is being mechanised so that they can be operated remotely. A motorised micropositioning cradle for the CCD detector is being constructed. This will enable automatic methods to be developed of telescope and artificial

star focusing along with automatic selections of sub-aperture size and filters appropriate to the seeing conditions and guide star magnitude.

3. Imaging Photon Detector: The original IPD has now been replaced with one of increased quantum efficiency, the new detector having a peak DQE of 4 percent as compared to the old value of 1 percent. This will enable stars of 13^{th} magnitude to be used as guide stars.

4. Optics: A few minor modifications to the optics of the present system are planned with the construction of a new split-lens system to enable a higher image magnification to be achieved on the IPD. The aim of this is to reduce problems associated with the local saturation of the IPD and to lessen the effect of the IPD's resolution.

5. Electronics: The electronics will be more compact with the existing six amplifier units used to drive the piezo-actuators replaced with a single in house built unit. The design of the digital to analogue convertor boards is also being changed to incorporate programmable analogue filters on the outputs. The purpose of these filters being to remove any motion that is injected by the present system above the cut off frequency of the digital tracking filter.

6. Algorithms: Work has been done on replacing the CUSPS algorithm. Problems were encountered with the present algorithm in quickly determining the correct algorithm parameters for the particular seeing conditions prevalent. Conditions being encountered where the seeing conditions, and hence the optimum CUSPS parameters, changed on time scales of a few minutes. It is therefore planned to implement heuristic algorithms that will constantly adjust to the changing conditions.

Work on these improvements is well on schedule and the full MARTINI II system will be tested at the WHT in October 1990.

MARTINI II is intended as a semi-common user instrument that will be available for High Resolution Imaging projects. Collaborations have already been formed to study the following resolution-limited astrophysical problems:

1. Planetary Nebulae: filamentary structure in giant halos and detailed structure of 'born-again' type planetary nebulae.

2. Active Galactic Nuclei: imaging the nuclear regions of NGC4151, Cygnus A and of a selection of Markarian Galaxies.

3. Planar shocks in Cygnus loop Supernova remnants and lowly ionized knots in Wolf-Rayet stars.

6.2 Future Research

In the visible, full wavefront correction on r_o scales involves large numbers of sub-apertures and actuators, highly detailed wavefront sensing and copious quantities of reference light. Further development of MARTINI will therefore involve the investigation of the use of large ($D \simeq 4r_o$) tilt-corrected sub-apertures which would then be co-phased using one of several possible techniques. This system would not attempt to correct small spatial scale turbulence but would concentrate on the longer baselines. Figure 6.1 shows the theoretical image that is obtained using six tilt corrected, but unphased, apertures whilst figure 6.2 shows the expected image if co-phasing of the apertures is achieved. It can be seen that phasing produces an extremely sharp central image (FWHM $\simeq 0.026$ arcseconds *in the visible*) corresponding to the longest baselines, surrounded by a number of subsidiary peaks. Such phasing of the apertures might be achieved by using a neural network technique such as that suggested by ANGEL [73].

If such a system is successful research will be directed towards a full 4-metre aperture adaptive system based on $4r_0$ diameter sub-aperture co-phasing in the visible. The system would be automated, like MARTINI II, to provide some astronomical observational capability during the research period. All techniques employed will be scalable for application to the planned United Kingdom Large Telescope (UKLT).

Research is also being carried out in Durham into the possibility of using liquid crystals as the means of phase correction of a distorted wavefront. The refractive index of a liquid crystal can be altered by the application of a voltage across the

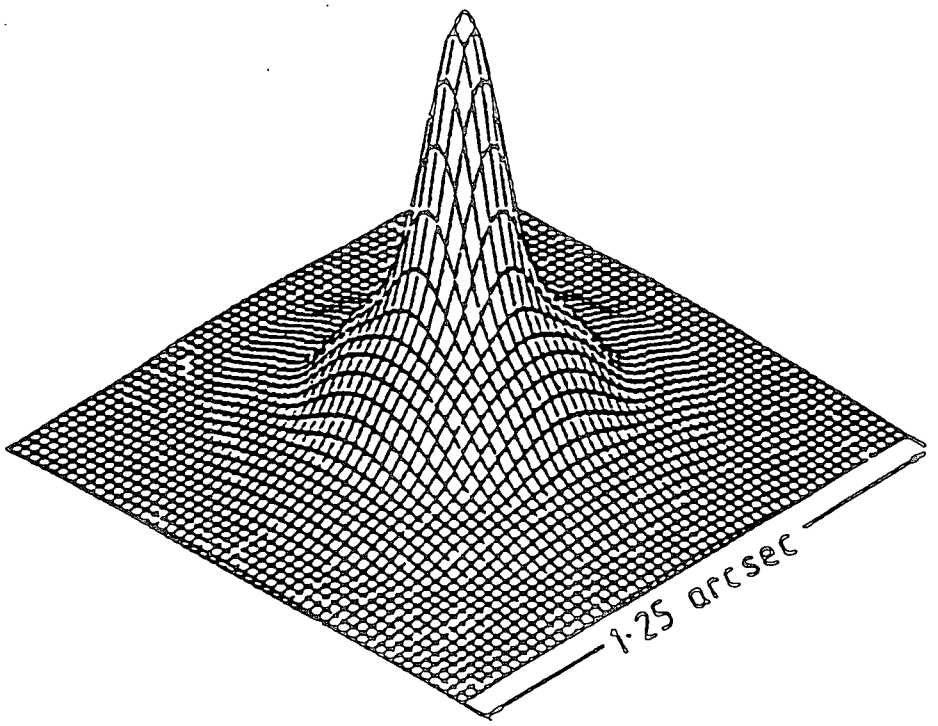

Figure 6.1: Theoretical point spread function obtained by six tilt corrected unphased apertures for an r_0 of 0.15 m and a sub-aperture diameter of 0.60 m.

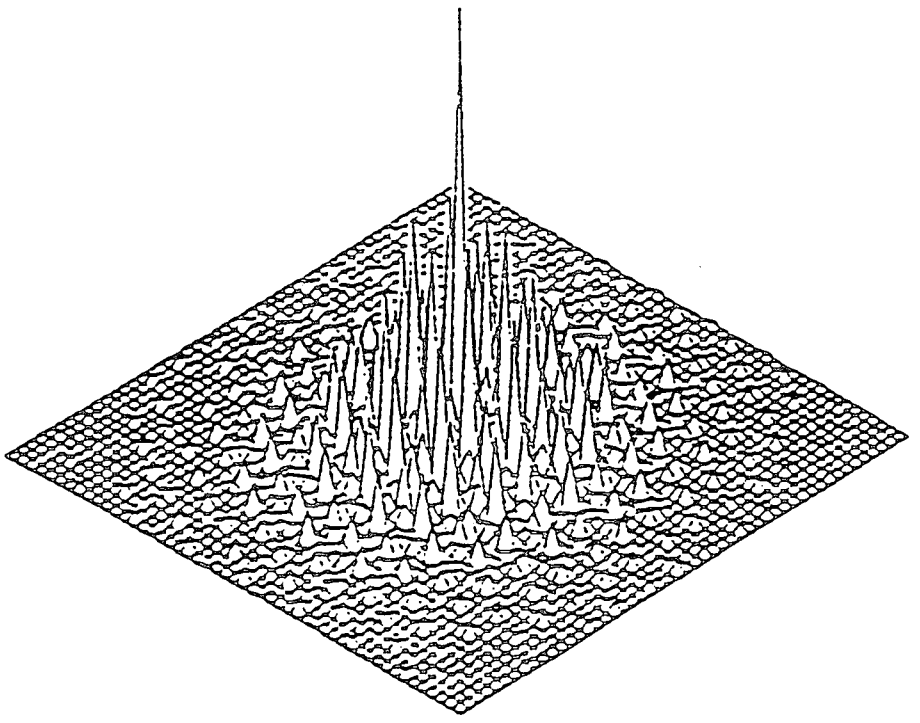

Figure 6.2: Theoretical point spread function obtained by six tilt corrected phased apertures for an r_0 of 0.15 m and a sub-aperture diameter of 0.60 m.

crystal and if an array of such liquid crystal cells were constructed, the tilt of an incident wavefront could be removed by the application of a suitable voltage gradient across the array. In fact a more complicated system can be imagined where the voltage gradient applied is not uniform, but varies in such a way as to remove all the distortion of the wavefront not just the tilt. Since liquid crystals only effect one direction of polarisation, at least two orthogonal arrays would have to be used to ensure the full correction of the incident wavefront. The advantages of such a system are that there would be no moving parts and the possibility of producing a compact system. However, work in this field is still in its early stages.

Appendix A

Isoplanatic Patch Size For Conjugate Focus Position

The mean squared optical path difference σ_p^2 between two points in the atmosphere separated by a distance ξ is given by

$$\sigma_p^2 = \left(\frac{\lambda}{2\pi}\right)^2 D_\phi(\xi) = 6.88\left(\frac{\lambda}{2\pi}\right)^2\left(\frac{\xi}{r_o}\right)^{\frac{5}{3}} \tag{A.1}$$

where $D_\phi(\xi)$ is the phase structure function.

Considering now the optical arrangement shown in figure 2.18 of chapter 2, where the wavefronts from two different sky directions, separated by an angle θ, are compared at a plane positioned downstream of the main telescope focus and conjugate to a height in the atmosphere of h_c. If the seeing is assumed to be due to a single layer of turbulence at a height h and of a thickness δh, points on the wavefronts that are coincident at the conjugate plane will be separated by a distance $\theta|h - h_c|$ at the turbulent layer. The mean squared optical path difference between the points can be calculated from equation A.1 as

$$\sigma_p^2 = 6.88\left(\frac{\lambda}{2\pi}\right)^2\left(\frac{\theta|h - h_c|}{r_o}\right)^{\frac{5}{3}} \tag{A.2}$$

Substituting in the value of r_o as

$$r_o = \left[0.423\left(\frac{2\pi}{\lambda}\right)^2 C_N^2(h)\delta h\right]^{-\frac{5}{3}}, \tag{A.3}$$

equation A.2 can be rewritten as

$$\sigma_p^2 = 2.91\,\theta^{\frac{5}{3}}|h - h_c|^{\frac{5}{3}} C_N^2(h)\delta h. \tag{A.4}$$

This can now be extended to a continuous distribution of turbulent layers where the above equation becomes

$$\sigma_p^2 = 2.91\,\theta^{\frac{5}{3}} \int_0^\infty |h - h_c|^{\frac{5}{3}} C_N^2(h)dh, \tag{A.5}$$

this can be rewritten using equation A.3 as

$$\sigma_p^2 = 6.88\left(\frac{\lambda}{2\pi}\right)^2 r_o{}^{-\frac{5}{3}}\theta^{\frac{5}{3}} \left[\frac{\int_0^\infty |h - h_c|^{\frac{5}{3}} C_N^2(h)dh}{\int_0^\infty C_N^2(h)dh}\right]. \tag{A.6}$$

If we now adopt Fried's criterion for isoplanatism that the maximum allowable root mean square optical path difference σ_p between two wavefronts at the conjugate plane is $\frac{\lambda}{2\pi}$ (corresponding to a phase difference of one radian), and substitute this value into the equation A.6. Then re-arranging, the angular extent of the isoplanatic patch Ω can be written as

$$\Omega = 0.62 r_o \left[\frac{\int_0^\infty |h - h_c|^{\frac{5}{3}} C_N^2(h)dh}{\int_0^\infty C_N^2(h)dh}\right]^{-\frac{3}{5}} \tag{A.7}$$

The integral part of the above equation can now be substituted for by an average turbulent layer height $\overline{h}_c$ defined as

$$\overline{h}_c = \left[\frac{\int_0^\infty |h - h_c|^{\frac{5}{3}} C_N^2(h)dh}{\int_0^\infty C_N^2(h)dh}\right]^{\frac{3}{5}}, \tag{A.8}$$

and so equation A.7 can be written as

$$\Omega = 0.62\frac{r_o}{\overline{h}_c}. \tag{A.9}$$

Appendix B

Detectors In Adaptive Optics

The requisite of a detector for use in wavefront distortion sensing in an adaptive optics image sharpening system, is that the image centroid of the reference star can be read out in a fast enough cycle time so that the effects of seeing motion are effectively frozen ($\approx$10–50 ms). The current photon counting detectors capable of fulfilling these requirements all tend to be based on image intensifier designs. A summary of the basic detectors currently used for adaptive optics systems is is given as follows:-.

The Intensified Charged Coupled Device (ICCD): The typical construction of this device is shown in figure B.1. A photon incident on the photocathode of the image intensifier stage liberates an electron which is accelerated by a high voltage field onto the first of several microchannel plates. These microchannel plates now amplify the original signal by a factor of $\sim 10^7$ and the electron cloud that emerges from the final plate is then incident on a phosphor producing a light burst of photons. The position of this photon burst is then recorded by a CCD detector which is coupled to the phosphor's output face via a tapered fibre optic link. The overall efficiency of this device is determined by the efficiency of the intensifier stage. This typically for an S20 photocathode means that the peak detected quantum efficiency (DQE) of the device is approximately 8 percent. The readout time of the device is determined by the time required to clock out and read the CCD chip pixels, this limits the time resolution to typically $\sim$15 ms.

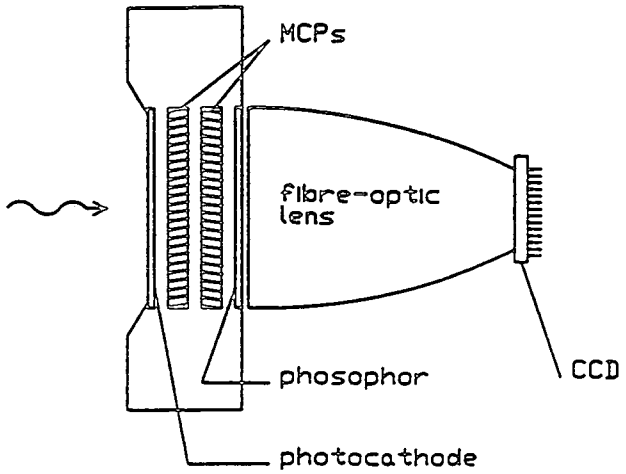

Figure B.1: Schematic diagram of the ICCD detector (from Hickson [74]).

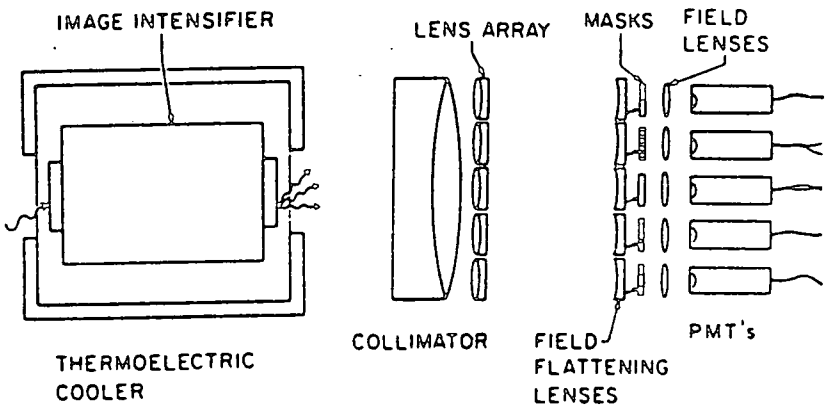

Figure B.2: Schematic diagram of the PAPA detector (from Papaliolios et al. [75]).

The Precision Analogue Photon Address System (PAPA): The design of this detector is shown schematically in figure B.2. The output face of an an image intensifier is imaged by an array of lenslets onto a number of photomultiplier tubes each of which is covered with a Gray coded mask (Gray coding being used in preference to binary coding to avoid errors associated with photon events occurring on mask boundaries). A photon detection by the image intensifier produces a bright spot on the output phosphor. The light from this spot will, however, only be detected by certain photomultipliers due to the coded mask arrangement, and according to which tubes provide a signal the position of the photon event can be established; each photomultiplier giving information on one bit of the photon X or Y position. The efficiency of the device is again limited by the intensifier stage with a peak DQE of ~ 8 percent. A fuller description of the PAPA detector is given in PAPALIOLIOS ET AL. [75]

The Image Photon detector (IPD): This is another device based on a photocathode-microchannel plate intensifier, the output of which is incident on an arc-terminated resistive anode. The IPD was the detector chosen for the MARTINI system and a fuller description of the device is given in chapter 4.

The disadvantage with all the above systems is their relatively low efficiency (peak DQE ~5–10%). This limits the magnitude of the reference star that can be used for adaptive optics image sharpening purposes and so limits the sky coverage of this technique. A possible solution to this problem is the development of the Avalanche Photo-diode Detector (APD) which is based on a semi-conductor photo-diode device, the construction of which is shown schematically in figure B.3. These devices are usually operated in the 'Geiger mode' where the device is biased with a few more volts than the reverse breakdown voltage. This bias voltage produces a depletion layer in the π layer and a high voltage field in the *pn* junction. Photons that enter the detector though the p^+ electrode produce electron-hole pairs in the π layer and these electrons then drift across to the depletion layer where they are accelerated by the high voltage field and produce more electron-hole pairs through impact ionisation. These secondary electrons are themselves accelerated causing more ionisation and hence an avalanche effect is produced that causes a charge pulse to appear at the electrodes. Once this charge pulse has been detected by

subsidiary electonics the electron avalanche is actively quenched in order that the APD is rapidly returned to a state where it is ready to detect another photon arrival.

As mentioned above the main advantage of the APD is its enhanced efficiency compared to photocathode based devices; a typical efficiency versus wavelength curve for an APD is shown in figure B.4 along with the efficiency curve for an S20 photocathode. As can seen from this figure the efficiency of the APD is approximately 40-80 percent over a wavelength range of 400–800 nm.

However, there are at present drawbacks with using APDs, for example multi-pixel APD arrays suffer problems with cross-talk since the electron avalanche produced on the detection of a photon can itself produce photons which can trigger adjacent APD pixels. APD also exhibit 'afterpulsing', which is the generation of spurious electron avalanches after a true photon induced electron avalanche has occurred, and 'junction heating' which is the heating of the device at high count rates, due to the photon induced current flow, which causes the efficiency of the device to be unstable.

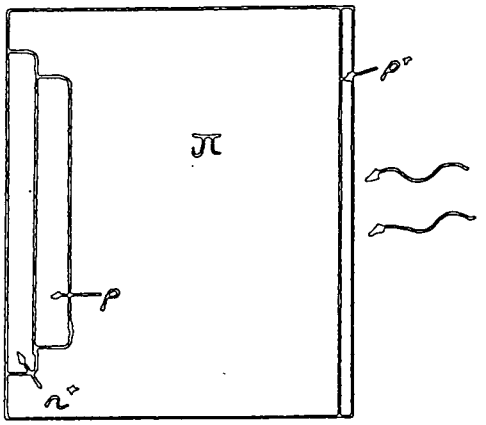

Figure B.3: Schematic diagram of the APD detector (from Nightingale [76]).

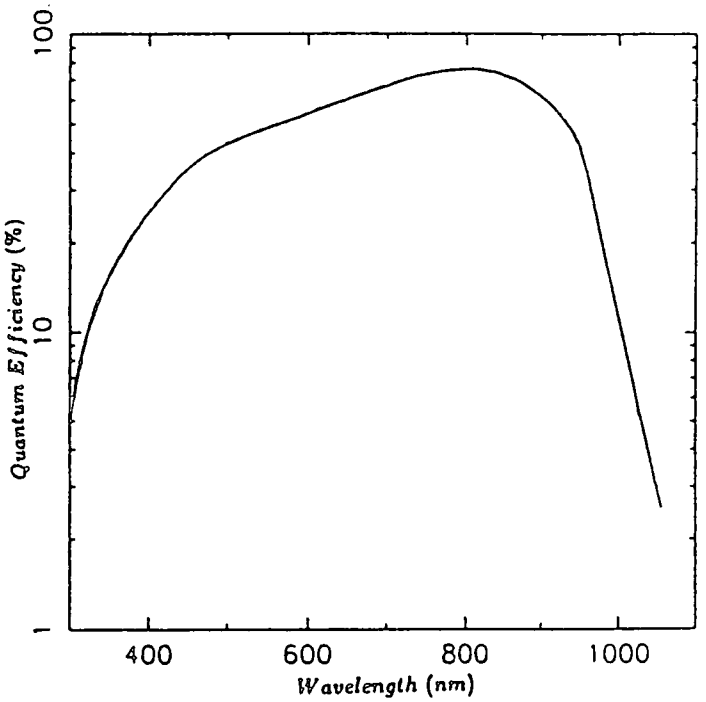

Figure B.4: Detected Quantum Efficiency versus wavelength for an APD detector (from Nightingale [76]).

Appendix C

Limiting Magnitude of Reference Star

According to Planck's theory of blackbody radiation, the energy flux E_λ emitted between wavelength λ and $\lambda+d\lambda$ from unit area of a blackbody at temperature T Kelvin, is given by the expression

$$E_\lambda = \frac{2\pi hc^2}{\lambda^5} \frac{1}{\left[\exp(-\frac{hc}{\lambda kT}) - 1\right]} d\lambda, \tag{C.1}$$

where h is Planck's constant, c is the velocity of light and k is Boltzmann's constant. The total energy flux E_{BB} emmitted by a black body per unit area is given by

$$E_{BB} = \sigma T^4, \tag{C.2}$$

where σ is Stefan's constant. Using equations C.1 and C.2 the fraction F_λ of energy that is emmitted between wavelengths λ and $\lambda + d\lambda$ per unit blackbody area is

$$F_\lambda = \frac{E_\lambda}{E_{BB}}. \tag{C.3}$$

To calculate the number of photons produced by a star, the star can be considered a blackbody source at an effective temperature of T_{eff}. The effective temperature of a star can be found from tables using its colour index B–V. The bolometric correction term BC can also be determined from such tables and the bolometric magnitude of the star calculated from the V band magnitude m_V using the relation

$$m_{bol} = m_V + \mathrm{BC}. \tag{C.4}$$

Now it is known that a star of apparent bolometric magnitude $m_{bol} = 0.0$ gives a total energy flux E_{ta} of 2.45×10^{-12} J sec^{-1} cm^{-2} at the top of the Earth's atmosphere (ALLEN [77]), the energy flux at any other bolometric magnitude m_{bol} is then given by the relationship

$$E_{ta} = 2.45 \times 10^{-12} \times 2.51^{m_{bol}} \text{J sec}^{-1} \text{cm}^{-2}. \tag{C.5}$$

Assuming that the energy arriving at the top of the atmosphere has a blackbody distribution, the flux of photons N_λ in wavelength range λ to $\lambda + d\lambda$ per square centimetre per second at the top of the Earth's atmosphere can now be determined using equations C.3 and C.5 with

$$N_\lambda = \left(\frac{\lambda}{hc}\right) F_\lambda E_{ta} \text{ counts sec}^{-1} \text{cm}^{-2}. \tag{C.6}$$

Using the above equations the expected photon count rate per unit wavelength per centimetre squared at the top of the Earth's atmosphere can be calculated for any star of given V-band magnitude and colour index.

To determine the photon count rate expected to be detected by an IPD detector mounted on an astronomical telescope, the quantum efficiency C_λ of the IPD, the size of the telescope aperture D, and the atmospheric transmission A_λ must be taken into account. The total count rate N_{ipd} expected to be detected by the IPD is then

$$N_{ipd} = \frac{\pi D^2}{4} \int_0^\infty N_\lambda C_\lambda A_\lambda \, d\lambda \text{ counts sec}^{-1}. \tag{C.7}$$

Figure C.3 shows the expected count rate N_{ipd} versus V-band magnitude for a variety of aperture sizes, calculated using the IPD efficiency and atmospheric transmission versus wavelength curves shown in figures C.1 and C.2. The V-band magnitude given in the figure is for main sequence star of spectral calls G0 with a bolometric correction term of -0.06.

To determine the limiting star magnitude that can be used as the guide star in adaptive optics wavefront tilt correction, the number of photons required to establish an image centroid accurately, and the length of the integration time that can be used such that the seeing motion is effectively 'frozen' within this time, must be known.

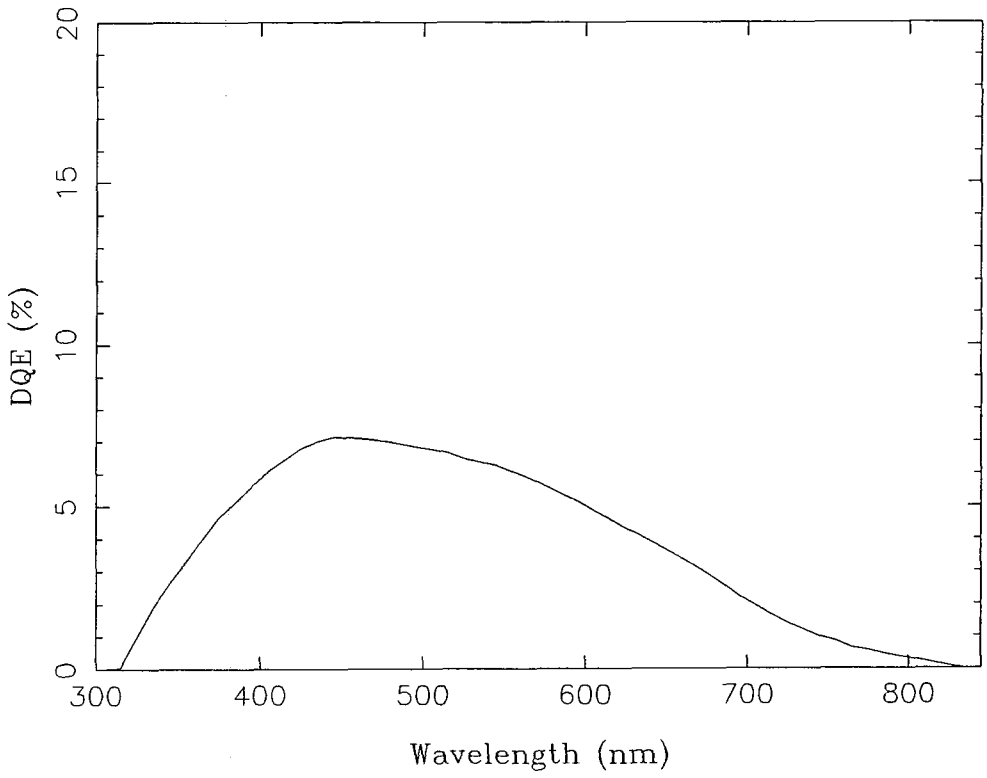

Figure C.1: IPD detected quantum efficiency versus wavelength for an S20 photocathode (peak RQE~ 20 %), assuming a 30 % multichannel plate throughput efficiency.

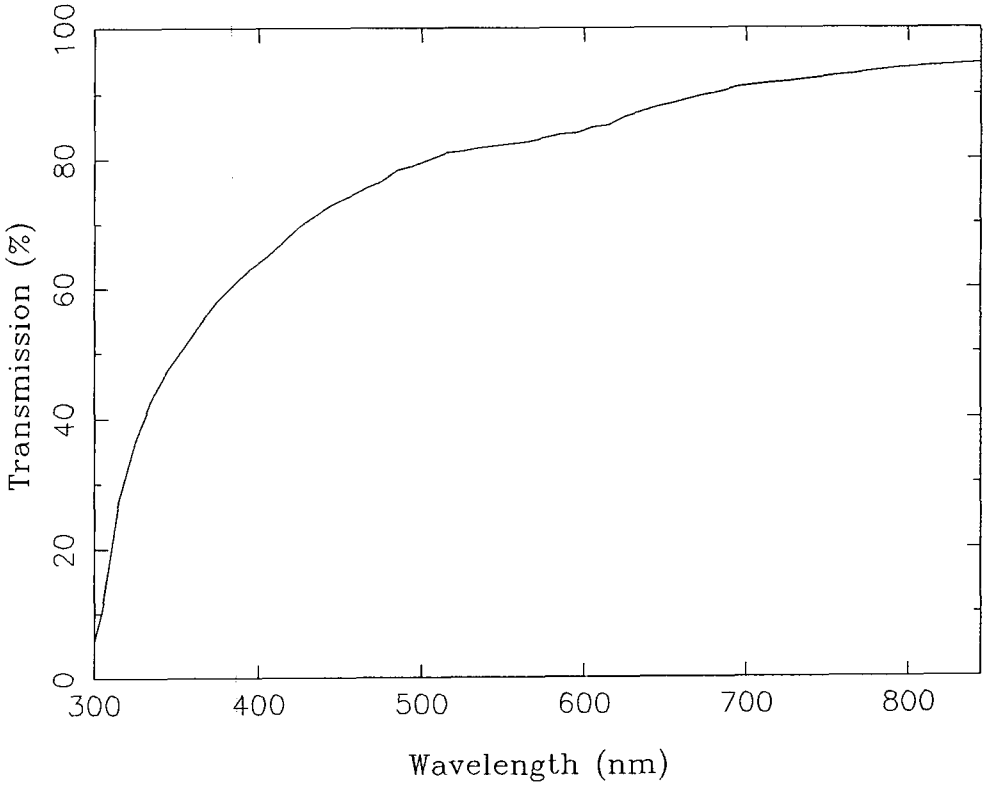

Figure C.2: Atmospheric transmission versus wavelength (from Allen [77]).

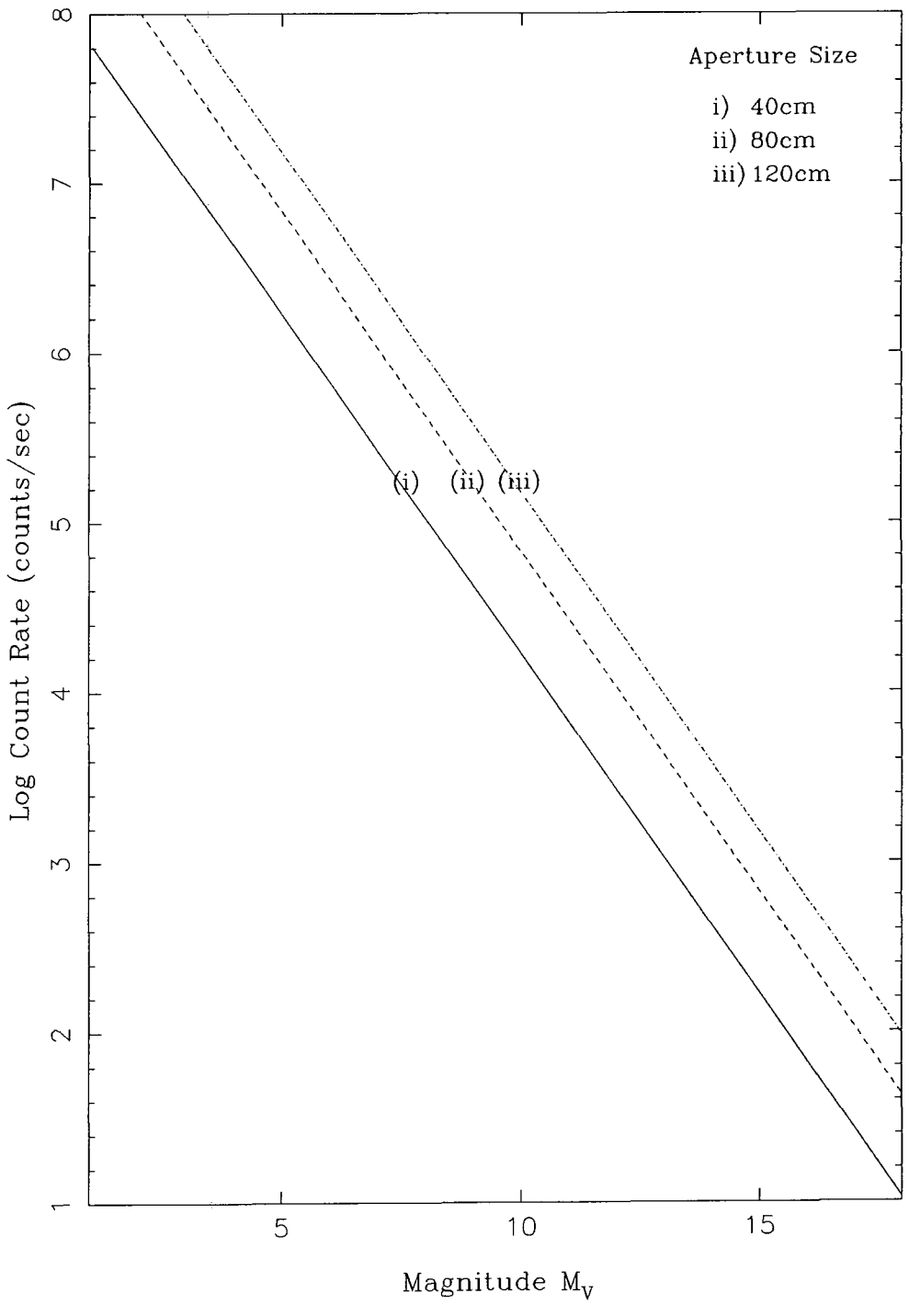

Figure C.3: Count rate detected by an IPD detector versus star V–band magnitude (calculated for a G0 star with bolometric correction term -0.06).

The number of photons required to determine the image centroid was found by simulating random photon arrivals in a short exposure image based on the point spread functions obtained from the theory outlined in §2.2.2 of chapter 2. These events were then binned into sequential segments containing fixed numbers of photons and the positions of the photons in each segment used to calculate an image centroid. The average positional error of these centroids from the true centroid position was then calculated. This procedure was preformed for segments of increasing photon number from 2–100 in steps of 2. This was then repeated for events simulated with short exposure image point spread functions corresponding to coherence parameter r_o values of 10 cm, 20 cm, and 30 cm. The results of these simulations are shown in figure C.4 and it can be seen that, to establish an image centroid to an accuracy of a tenth of an arcsecond approximately 20 photons are required.

The integration time that can be used in determining a image centroid is very dependent on the seeing conditions prevalent at the time of the observation. Assuming a typical seeing matched aperture of 40 cm ($r_o = 0.1$ m) and a crosswind velocity of 10 ms^{-1} in the dominant turbulent layer, the correlation time of seeing is given by equation 2.41 of chapter 2 as about 40 ms, thus to obtain sufficient photons within this time period to accurately determine a star image centroid (~ 20 photons) the required photon count rate is ~ 500 counts per second which from figure C.3 can be seen to correspond to a star of V-band magnitude of $\sim 13.5^{th}$.

It must be mentioned that no account is taken in these calculations of any loss of light due to the telescope optics or any optical elements before the IPD detector. Any such losses will effect the magnitude of the guide star that can be used; for example if there is a 50 % loss of light this would mean that an approximately 0.75 magnitudes brighter guide star is required to achieve the necessary count rate.

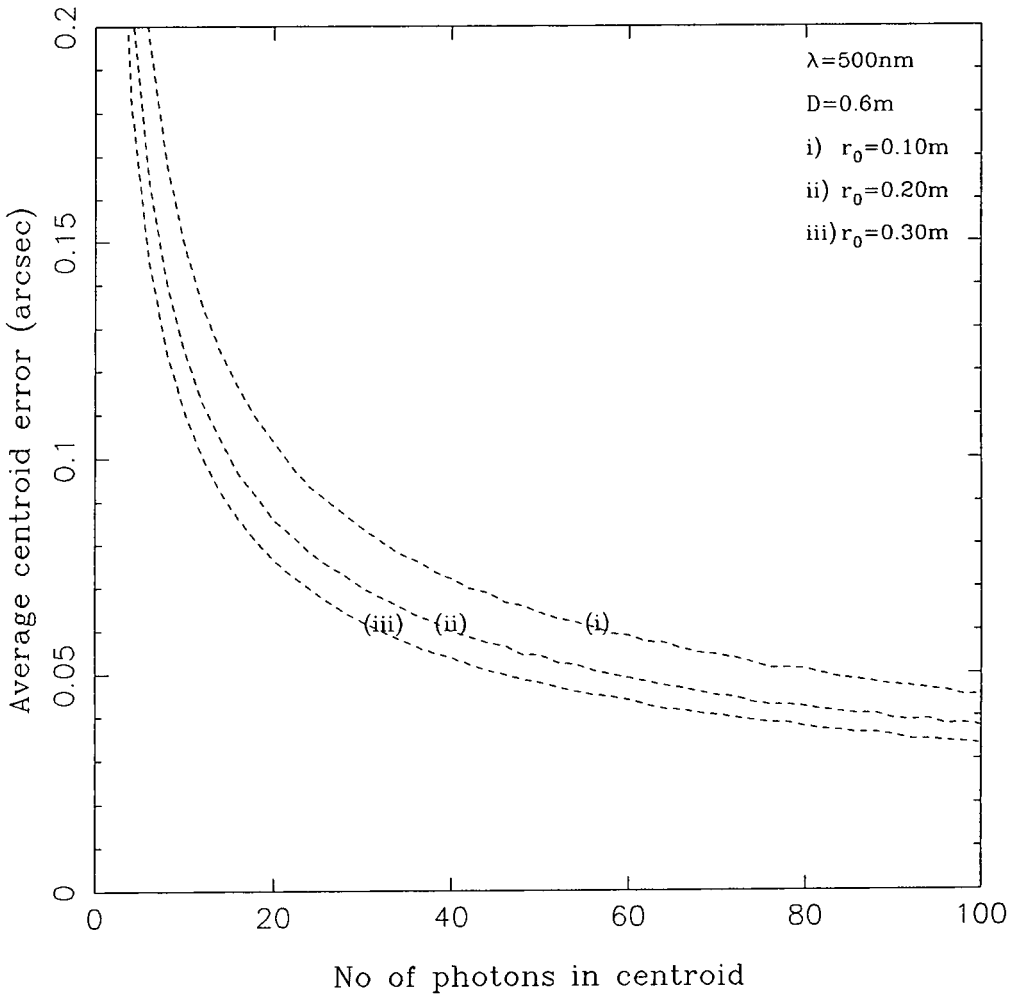

Figure C.4: Average centroid error versus number of photons in the centroid for short exposure point spread functions modelled with r_o values of 0.10 m, 0.20 m, and 0.30 m.

Appendix D

Detection Limits For Astronomical Objects

The signal to noise ratio SNR for an astronomical object observed with a Charged Coupled Device camera is given by

$$\mathrm{SNR} = \frac{\mathrm{N}_r \tau}{(\mathrm{N}_r \tau + \mathrm{S}_r \tau + p Q_e)^{-\frac{1}{2}}}, \tag{D.1}$$

where N_r is the expected number of counts per second from the astronomical object within a specified radius r of the image at the focal plane, S_r is the number of counts due to the sky background, Q_e is the RMS pixel noise value p is the number of CCD pixels within the image radius r chosen, and τ is the exposure time.

To calculate the SNR for a star observed with the MARTINI system, the number of counts per second expected at the top of the atmosphere per square centimetre per second N_λ from a certain magnitude astronomical object was determined using the method outlined in appendix C. This number was then corrected for atmospheric transmittance A_λ, CCD efficiency K_λ, Kitt Peak V–band filter transmittance V_λ, and the sub-aperture size D, such that the total number of counts from the astronomical object expected to be detected by the CCD camera $\mathrm{N}_{\mathrm{ccd}}$ is given by

$$\mathrm{N}_{\mathrm{ccd}} = \frac{6\pi D^2}{4} \int_0^\infty \mathrm{N}_\lambda \mathrm{K}_\lambda \mathrm{A}_\lambda \, d\lambda \ \text{counts}\,\text{sec}^{-1}, \tag{D.2}$$

with D given in centimetres. The factor of six in above equation is present to take account of the six sub-apertures of the MARTINI system. The value for the atmospheric transmission versus wavelength used in the calculations was the

same as that shown in figure C.2 of the previous section. The values used for the CCD efficiency and V–band filter transmittance versus wavelength are shown in figures D.1 and D.2.

To find the number of counts per second N_r expected in a specific image radius at the focal plane, the astronomical object was assumed to be a point like source, and the fraction of the total counts that would be expected inside a given image radius calculated using the enclosed energy curves for a theoretical short exposure image obtained for the particular value of the coherence parameter r_o and sub-aperture diameter D chosen (see figure D.3).

The expected count rate from the sky background within a given image radius at the focal plane of a telescope S_r was calculated in the following way. The magnitude of the dark sky was assumed to be $m_v = 21.8$ per arcsecond squared, thus the counts per second per centimetre squared per unit wavelength range was determined for a $m_v = 21.8$ magnitude star using the method outlined in appendix C (assuming magnitude given is for a G0 star with bolometric correction term -0.06). This figure was then corrected for atmospheric transmittance, CCD efficiency, V–band filter transmittance, and sub-aperture diameter, to give the total number of counts expected to be detected by the CCD from the sky background S_{ccd} over an area at the focal plane corresponding to a one arcsecond squared area of sky. The sky background rate S_r within a specified radius r (in arcseconds) was then determined from S_{ccd} with

$$S_r = \pi r^2 S_{ccd} \text{ counts sec}^{-1}. \tag{D.3}$$

The values obtained for N_r and S_r were then substituted into equation D.1 and the signal-to-noise calculated, with the RMS pixel noise Q_e assumed to be 8 electrons and the value of p based on an image scale such that one CCD pixel represented 0.1 arcseconds squared. This calculation was performed for various values of r such that the SNR for the particular magnitude and seeing conditions chosen was optimised. Using this technique the star magnitude was found at which, assuming full correction was achieved by the MARTINI system, the SNR dropped below a value of ten for exposure times of 1000 and 3000 seconds. This was repeated for a seeing conditions corresponding to r_o values of 10 cm, 15 cm, and 20 cm, assuming in each case that seeing matched apertures ($D = 4r_o$) were

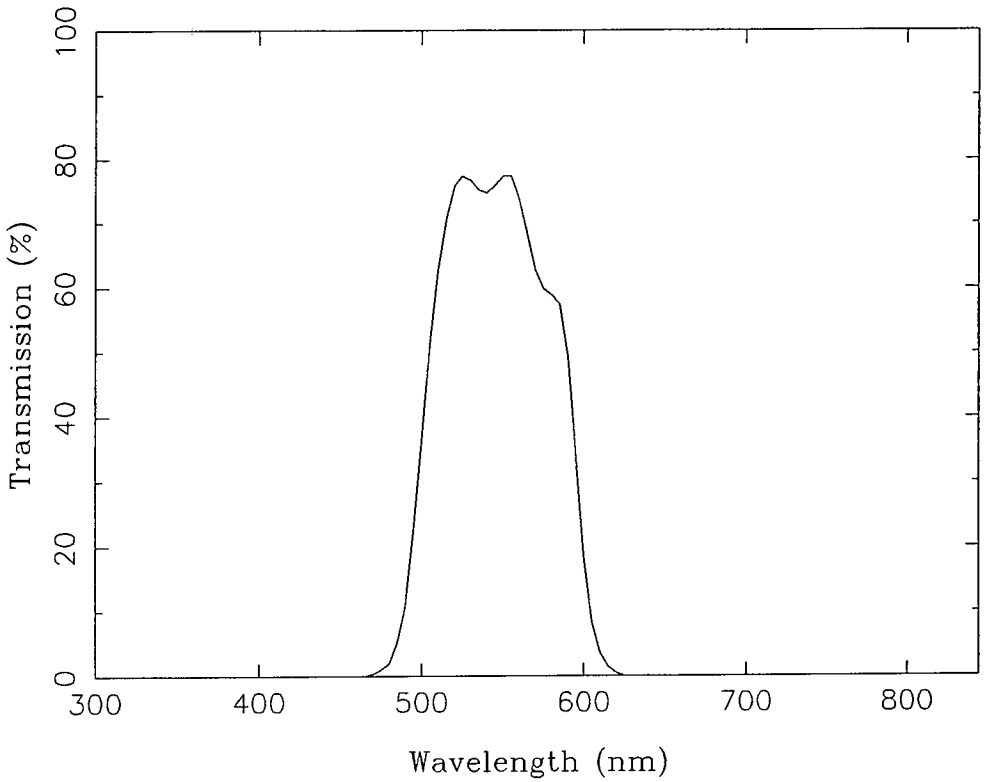

Figure D.1: Kitt Peak V–band filter efficiency versus wavelength (from Ungen et al. [78]).

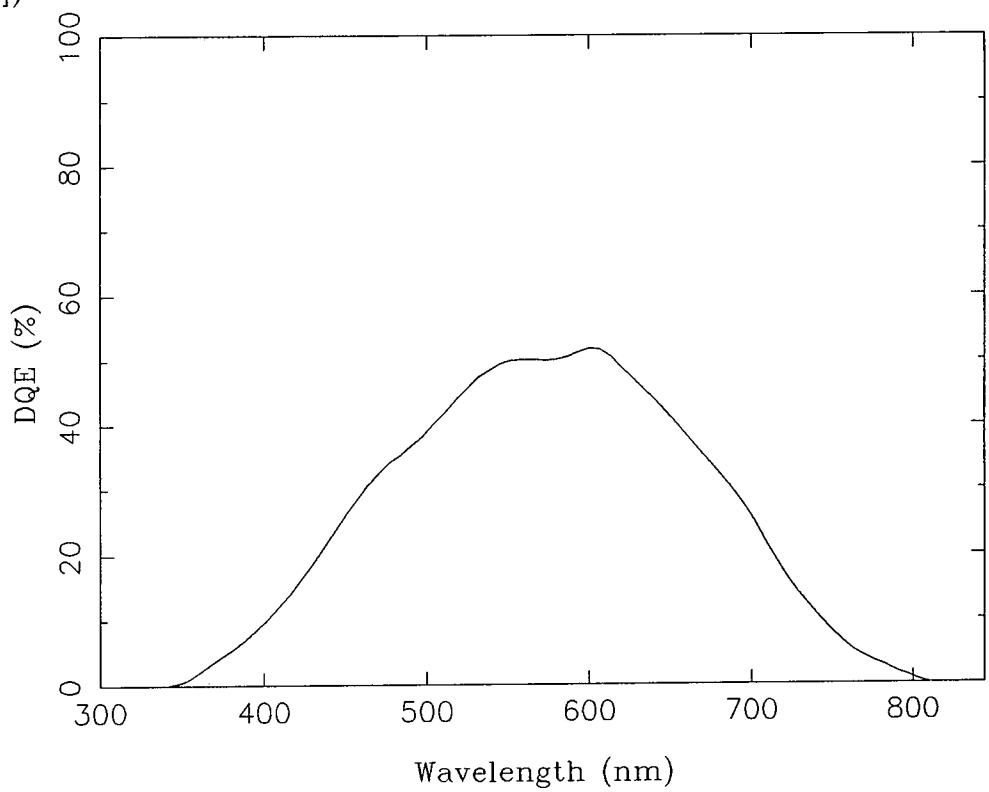

Figure D.2: CCD efficiency versus wavelength (from Ungen et al. [78]).

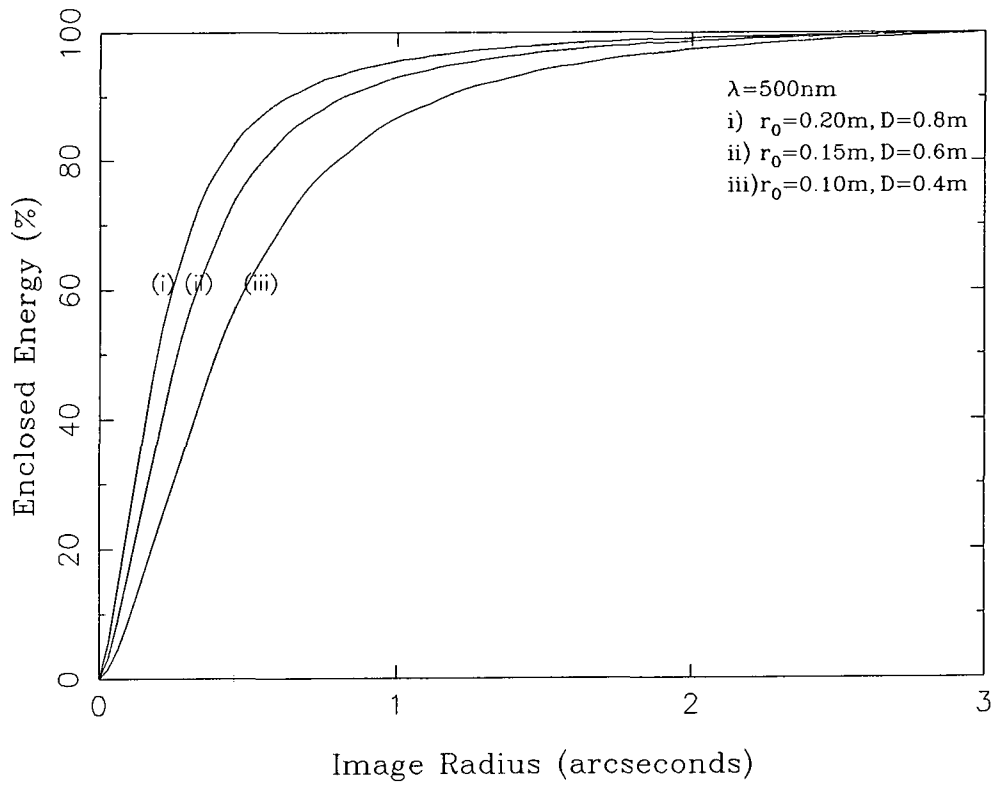

Figure D.3: Theoretical short exposure enclosed energy versus image radius for r_o values of 0.10 m, 0.15 m, and 0.20 m, with seeing matched apertures ($D = 4r_o$).

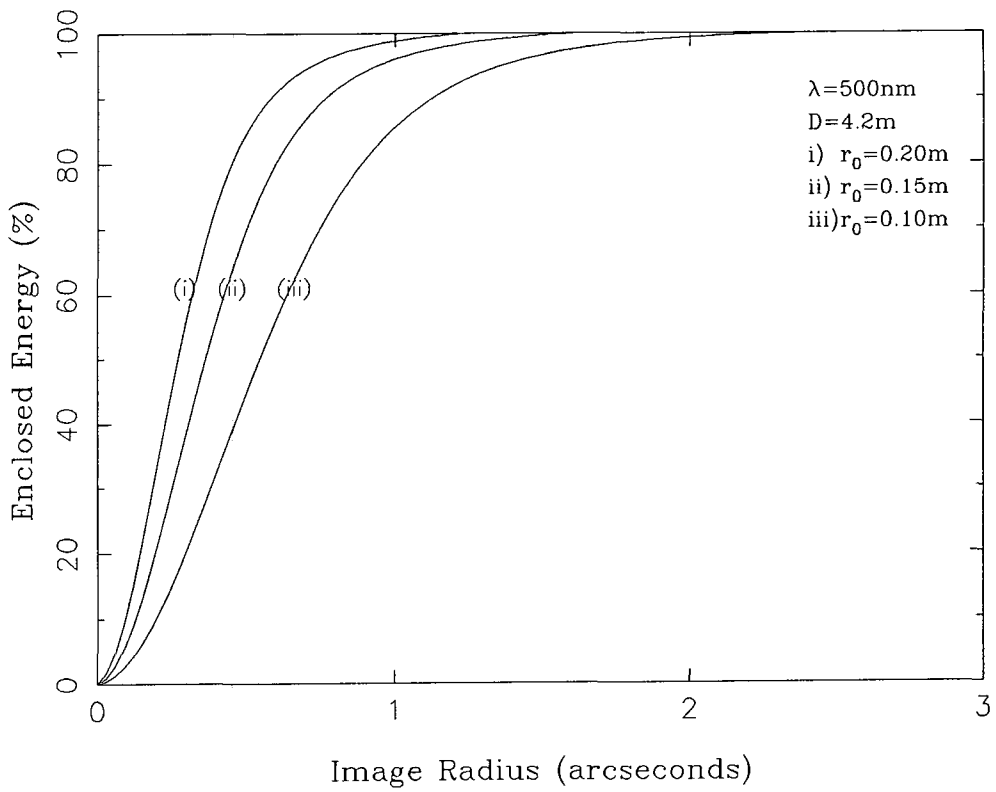

Figure D.4: Theroetical long exposure enclosed energy versus image radius for r_o values of 0.10 m, 0.15 m, and 0.20 m, for a telescope aperture of 4.2 m.

used for the observations.

The limiting magnitudes of the WHT with its full aperture for the same values of r_o as above was also calculated using the enclosed energy versus image radius curves shown in figure D.4. These curves were calculated from the theoretical long exposure point spread functions as described in §2.2.1 of chapter 2, for a telescope aperture of 4.2 m.

The results of these calculations are shown in table 4.2 of chapter 4.

Appendix E

Actuator Movement Algorithm

In operation the only information the MARTINI system has on the current position of the PZL actuator extension is obtained from the voltage applied to it. The voltage change required to be applied to an piezo-actuator in order to produce the required mirror deflection after each new photon event was found by using an actuator movement algorithm designed to minimise the effects of hysteresis.

In developing this movement algorithm, measurement of the actuator extension was achieved by using an actuator to drive one mirror of a Michelson interferometer. Movement of the actuator caused the circular interference fringes formed to expand or contract and by counting the number of fringes that crossed a fixed point the extension of the actuator could be measured (each movement of one fringe representing a distance of $\lambda/2$).

It was experimentally found that a ('S-shaped') voltage-extension curve could be established, the points on which marked the piezo-extension that would finally result for a given voltage if the actuator was oscillated around this voltage with decreasing amplitude. For regularly spaced points along this S-shaped curve, the voltage versus extension curves were experimentally established for increasing and decreasing voltage from the point. These experimental curves were then fitted with a polynomial of the form,

$$\mathrm{y_{extn}} = a_0 + a_1\mathrm{x} + a_2\mathrm{x}^2 + a_3\mathrm{x}^3, \tag{E.1}$$

where $\mathrm{y_{extn}}$ is the actuator extension, x the voltage applied and a_0, a_1, a_2, and a_3 are a set of fitting constants. The way the polynomial constants varied with

voltage starting point on the S-shaped curve was in turn fitted with polynomials so that semi-empirical upward and downward extension curves could be produced for any arbitrary starting point on the S-shaped curve. Using these curves the voltage change, required to move an actuator, with a given starting voltage, a given distance could be found. Thus a matrix $\mathrm{Hys_{j,k}}$ was produced containing the voltage change (actually stored in the form of DAC digitisation levels) required in order to produce movements of an integral number of a fixed distance steps, for any particular value of the current actuator voltage (the distance step size in the matrix was chosen to be 0.0625 microns, which corresponds to an 0.025 arcsecond deflection of the tilt mirrors). Therefore to find the voltage (DAC level) to be applied to an actuator to move the tilt mirror a required, the new voltage ma_N is found from $\mathrm{Hys_{j,k}}$, using the present piezo-actuator voltage ma_{N-1} and the number of 0.0625 μm steps *nstep* (as calculated by the CUSPS algorithm), as the indices.

$$m_N = \mathrm{Hys}_{ma_{N-1},nstep}. \tag{E.2}$$

This method of determining the voltage changes required to move the actuator a given distance was adopted since, even if the actual extension of the actuator does not lie on the S-shaped curve (and in practice it won't as it can be anywhere within the hysteresis envelope), the voltage changes determined with this technique are more accurate than if just a simple linear model of actuator movement were assumed.

Bibliography

[1] C.E. Coulman, J. Vernin, Y. Coqueugniot, and J.L. Caccia. *App. Opt.*, 1988, 27(1), 155.

[2] A. Kolmogorov. *Turbulence - Classic Papers in Statisical Theory.* Interscience Publishers Inc., New York, 1961.

[3] J. W. Goodman. *Statistical Optics.* Wiley and sons, 1985.

[4] V.I. Tartarski. *Wave Propagation in a Turbulent Medium.* McGraw-Hill Book Co. Inc., New York, 1961.

[5] A.M. Obukhov. *Ser Geograf. Geofiz*, 1949, 13, 58.

[6] A.M. Yaglom. *Dan. S.S.S.R.*, 1987, 69(6), 743.

[7] R. Barletti, G. Ceppatelli, L. Paterno, A. Righini, and N. Speroni. *J. Opt. Am.*, 1976, 66, 1380.

[8] R.E. Hufnagel. In *Digest of Technical Papers, Topical Meeting on Optical Propagation through Turbulence*, 1974.

[9] F. Roddier. The effects of atmospheric turbulence in optical astronomy. In E. Wolf, editor, *Progress in Optics XIX*, North-Holland, 1981.

[10] F. Roddier and C.Roddier. *Proc. Soc. Photo-Opt. Instr. Eng.*, 1986, 628, 298.

[11] D.L. Fried. *J. Opt. Soc. Am.*, 1966, 56(10), 1380.

[12] D.L. Fried. *J. Opt. Soc. Am.*, 1965, 55(11), 1427.

[13] J.R. King. *Pub. Astr. Soc. Pac.*, 1971, 83, 199.

[14] D.S. Brown and R.J. Scadden. *Observatory*, 1979, 99, 125.

[15] D.L. Fried. *J. Opt. Soc. Am.*, 1966, 56(10), 1327.

[16] D.L. Fried. *J. Opt. Soc. Am.*, 1978, 68(12), 1651.

[17] G.C. Valley. *App. Opt..*, 1979, 18(7), 984.

[18] M. Sarazin and F. Roddier. *Astron. Astro.*, 1990, 227(1), 294.

[19] B. McInnes and M. F. Walker. *Pub. Astron. Soc. Pac.*, 1974, 86, 529.

[20] B. McInnes. *Q. Jl R. astr. Soc.*, 1981, 22, 266.

[21] C. Dunlop, Y.A. Hamam, and J.V. Major. *Mon. Not. R. astr. Soc.*, 1989, 236, 875.

[22] D.L. Fried. *Optica Acta*, 1979, 26, 597.

[23] H.M. Martin. *Pub. Astron. Soc. Pac.*, 1987, 99, 1360.

[24] C. Christian and R. Racine. *Pub. Astr. Soc. Pac.*, 1985, 97, 1215.

[25] A.A. Michelson and F.G Pease. *Astrophys. J.*, 1921, 53, 249.

[26] M. Shao, M.M. Colavita, B.E. Hines, D.H. Staelin, D.J. Hutter, K.J. Johnston, D. Mozurkewich, R.S. Simon, J.L. Hershey, J.A. Hughes, and G.H. Kaplan. *Astron. Astophys.*, 1988, 193, 357.

[27] D.H. Rogstad. *Appl. Opt.*, 1966, 7, 585.

[28] W.T. Rhodes and J.W. Goodman. *J. Opt. Soc. Am.*, 1973, 63(6), 647.

[29] J.E. Baldwin, C.A. Haniff, C.D. Mackay, and P.J. Warner. *Nature*, 1986, 320, 595.

[30] C.A. Haniff, C.D. Mackay, D.J. Titterington, D. Sivia, J.E. Baldwin, and D.J. Warner. *Nature*, 1987, 328, 694.

[31] J.C. Dainty and R.J. Scadden. *Mon. Not. R. Astr. Soc.*, 1974, 167, 69.

[32] J.B. Breckinridge. *J. Opt. Soc. Am.*, 1975, 65(7), 755.

[33] F. Roddier and C.Roddier. *Astro. J.*, 1985, 295, L21.

[34] A. Labeyrie. *Astron. Astrophys.*, 1970, 6, 85.

[35] D.Y. Gezrai, A. Labeyrie, and R.V. Stachnik. *Astrophys. J. Letters*, 1972, 173, L1.

[36] R.H.T. Bates and P.T. Gough. *Astron. Astophys.*, 1973, 22, 319.

[37] K.T. Knox and Thompson B.J. *Astrophys. J.*, 1974, 193, L45.

[38] A.W. Lohmann, G. Weigelt, and B. Wimitzer. *App. Opt.*, 1983, 22(24), 4028.

[39] G. J. M. Aitken. *Pub. Astr. Soc. Pac.*, 1989, 101, 639.

[40] A. Hecquet and G. Coupinot. *J. Optics (Paris)*, 1985, 16(1), 21.

[41] J.J. Fuensalida, F.Rosa, and F.J. Fuentes. *Astron. Astrophys.*, 1988, 191, L13.

[42] M. Redfern, M.N. Devaney, P. O'Kane, E. Ballesteros Ramirez, R. Gomez Renasco, and F. Rosa. *Mon. Not. R. Astr. Soc.*, 1989, 238(2), 791.

[43] G. Lelièvre, J.L. Nieto, D. Salmon, A. Llebaria, E. Thouvenot, J. Boulesteix, E. Le Coarer, and J. Arnaud. *Astron. Astrophys.*, 1988, 200, 301.

[44] R.A. Hudgin. *J. Opt Soc. Am.*, 1977, 67(3), 393.

[45] G.C. Valley and S.M. Wandzura. *J. Opt. Soc. Am.*, 1979, 69(5), 712.

[46] G.C. Valley. *App. Opt.*, 1980, 19(4) 574.

[47] L.L. Cowie and A. Songalia. *Opt. Soc. Am.*, 1988, 5(7), 1015.

[48] R. Foy and A. Labeyrie. *Astron Astrophys.*, 1985, 152, L29.

[49] L.A. Thompson and C.S.Gardner. *Nature*, 1987, 328(6127), 229.

[50] R. Foy. Private communication.

[51] J.M. Beckers, F.J. Roddier, P.R. Eisenhardt, L.E. Goad, and Ker-li Shu. *Proc. Soc. Photo-Opt. Instr. Eng.*, 1986, 628, 290.

[52] H.W.Babcock. *Pub. Astr. Soc. Pac.*, 1963, 75, 1.

[53] A. Buffington, F.S. Crawford, R.A. Muller, A.J. Schwemin, and R.G. Smits. *J. Opt. Soc. Am.*, 1977, 67(3), 304.

[54] L.A. Thompson and H. Ryerson. *Proc. Soc. Photo-Opt. Instr. Eng.*, 1984, 445, 560.

[55] L.A. Thompson and F.Valdes. *Astrophys J.*, 1987, 315, L35.

[56] R.D. McClure, W.A. Grundmann, W.N. Rambold, J. Murray Fletcher, E. Harvey Richardson, J.R. Stilburn, R. Racine, C.A. Christian, and P. Waddell. *Pub. Astron. Soc. Pac.*, 1989, 101, 1156.

[57] R. Racine and R.D. McClure. *Pub. Astron. Soc. Pac.*, 1989, 101, 731.

[58] F. Maaswinkel, S. D'Odorico, and G. Huster. *ESO Messenger*, 1987, No.48, 51.

[59] F. Maaswinkel, F. Bortoletto, B. Buzzoni R. Buonanno, S. D'Odorico, B. Gilli, G. Huster, and W. Nees. In *ESO Conference on Very Large Telescopes and their Instrumentation*, 1988.

[60] P. Kern, P. Léna, G.Rousset, J.C. Fontanella, F. Merkle, and J.P. Gaffard. In *ESO Conference on Very Large Telescopes and their Instrumentation*, page 657, 1988.

[61] F. Merkle, P. Kern, P. Léna, F. Rigaut, J.C. Fontanella, G.Rousset, C. Boyer, J.P. Gaffard, and P.Jagourel. *ESO Messenger*, 1989, No.58.

[62] F. Merkle. *ESO Messenger*, 1990, No.60.

[63] L. Goad, F. Roddier, J. Beckers, and P. Eisenhardt. *Proc. Soc. Photo-Opt. Instr. Eng.*, 1986, 628, 305.

[64] F. Roddier and C. Roddier. In *ESO conference on Very Large Telescopes*, page 667, 1988.

[65] R.B. Dunn. In *LEST Technical report No28*, 1987.

[66] O. von der Lühe, A.L. Widener, G. Spence Th. Rimmele, R.B. Dunn, and P. Wilborg. *Astron. Astrophys.*, 1989, 224, 351.

[67] D. Rees, I. McWhirter, P.A. Rounce, F.E. Barlow, and S.J. Kellock. *J. Phys E: Sci. Instrum.*, 1980, 13, 763.

[68] M. Lampton and C.W. Carlson. *Rev. Sci. Instrum.*, 1979, 50(9), 1093.

[69] I. McWhirter. Ghril ipd technical manual.

[70] M. Blackman and J.L.Michiels. *Proc Phys. Soc.*, 1948, 6, 36.

[71] A. Sandage and G.Carlson. *Astro. J.*, 1988, 96(5), 1599.

[72] N. Tanvier. Ph.d thesis.

[73] R. Angel. Preprint. Submitted July 1990.

[74] P. Hickson. *Pub. Astr. Soc. Pac.*, 1986, 98, 622.

[75] C. Papaliolios, P. Nisenson, and S. Ebstein. *App. Opt.*, 1985, 24(2), 287.

[76] N. Nightingale. Private communication.

[77] C. W. Allen. *Astrophysical Quantities.* The Athlone Press, London, 1973.

[78] S.W. Unger, E.Brinks, R.A. Laing, K.P. Tritton, and P.M. Gray. Isaac newton group, la palma, observers guide. 1988.

Acknowledgements

I would like to express my thanks to Dr John Major, Dr Mike Thompson, Dr Richard Myers, Dr Colin Dunlop, and Gordon Love for the help they have given me in preparing this thesis and for the support shown to me during my time at Durham. I would also like to thank the physics department technical staff for their invaluable contribution to the MARTINI project.